ABSTRACT

Title of Thesis:	HEALTH IMPACTS OF THERMAL RUNAWAY EVENTS IN OUTDOOR LITHIUM-ION BATTERY ENERGY STORAGE SYSTEM INSTALLATIONS
	Zelda Qijing Zhao, Master of Science, 2024
Thesis Directed By:	Dr. Jamie McAllister, Department of Fire Protection Engineering

This study aimed to develop a methodology for characterizing health impacts of large-scale, outdoor, lithium-ion battery energy storage systems (BESS) thermal runaway events. A literature review was conducted to identify toxic gas yields produced during flaming and non-flaming thermal runaway, as well as mass loss rates, gas temperature, typical BESS unit capacity and dimensions, and event durations. Lithium-iron-phosphate and nickel-manganese-cobalt cell chemistries were assessed. The BESS unit thermal runaway events were modeled in Fire Dynamics Simulator with a bounding analysis for wind and ambient temperature. Concentrations were evaluated using Immediately Dangerous to Life or Health values for occupational exposure and the Protective Action Criteria for Chemicals hierarchy values (Acute Exposure Guideline Levels-

Level 1, Emergency Response Planning Guidelines- Level 1, Temporary Emergency Exposure Limits- Level 1) for community exposure. Through application of the methodology, a relationship between exposure limit distance and wind speed, ambient temperature, event duration, cell chemistry, and toxic gas species can be assessed. Under the conditions modeled in this project, exposure limits were exceeded at longer distances in the non-flaming scenarios when compared to the flaming scenarios. Wind speed, ambient temperature, event duration, cell chemistry, and toxic gas species were the controlling factors for non-flaming exposure limit distances. Wind speed was the primary controlling factor for flaming exposure limit distances; however, event duration had some influence.

HEALTH IMPACTS OF THERMAL RUNAWAY EVENTS IN OUTDOOR LITHIUM-ION BATTERY ENERGY STORAGE SYSTEM INSTALLATIONS

by

Zelda Qijing Zhao

Thesis submitted to the Faculty of the Graduate School of the
University of Maryland, College Park, in partial fulfillment
of the requirements for the degree of
Master of Science
2024

Advisory Committee:
Dr. Jamie McAllister, Chair
Dr. Fernando Raffan-Montoya, Assistant Professor
Dr. Arnaud Trouvé, Professor

Dedication

To my mom.

Acknowledgements

I would like to thank Dr. McAllister for mentoring and guiding me through the research process. Thank you for believing in me and my potential as a researcher and for always pushing me to be a better engineer. I am always thankful that you picked me up when I was a junior in undergrad and let me be a part of FireTox. I have learned a lot under your guidance and hope to continue gaining experience in new projects with you.

I would like to thank Brendan McCarrick for helping me figure out the approach and setting time aside from your other tasks to work on this project. Your guidance was incredibly helpful, and I am incredibly grateful for your support in the literature review and modeling input calculations, as well as all the grunt work you helped me complete.

I would like to thank Dr. Trouvé, Stephen Olenick, and Jonathan Hodges for their assistance in Pyrosim and FDS. I am grateful to them for helping me develop my modeling approach and troubleshoot the FDS simulation. Thank you to Jonathan for also taking the time to walk me through pyFDStools so I could process the FDS data. Without their help, the FDS analysis would not have been possible.

I would like to thank Daniel for making sure I had a work-life balance while I was working on this thesis. Thank you for keeping me company during the long workdays and making sure I ate and slept well.

This work was partially supported by the SFPE Foundation.

Table of Contents

List of Tables

List of Figures

List of Abbreviations

A: ampere

ACGIH: American Conference of Governmental Industrial Hygienist

ABS: acrylonitrile butadiene styrene

AEGL: Acute Exposure Guideline Levels

Ah: ampere-hour

AIHA: American Industrial Hygiene Association

ANSI: American National Standard Institute

ARC: accelerating rate calorimeter

AQI: Air Quality Index

BESS: battery energy storage system

BEV: battery electric vehicle

BMS: battery management system

CATL: Contemporary Amperex Technology Co., Limited

CFD: computational fluid dynamics

DEC: diethyl carbonate

DMC: dimethyl carbonate

DME: dimethoxyethane

DOE: Department of Energy

EC: ethylene carbonate

EEPS: engine exhaust particle sizers

EMC: ethyl methyl carbonate

EPA: Environmental Protection Agency

ERPG: Emergency Response Planning Guidelines

ESS: energy storage system

EV: electric vehicles

FM: Factory Mutual

FDS: Fire Dynamics Simulator

FEC: fractional effective concentration

FED: fractional effective dose

FID: flame ionization detection

FPRF: fire Protection Research Foundation

FTIR: Fourier Transform infrared spectroscopy

GC: gas chromatography

GC-MS: gas chromatography mass spectroscopy

GC-TCD: gas chromatography thermal conductivity detector

HDPE: high-density polyethylene

HPIC: high-pressure ion chromatography

HRR: heat release rate

HRRPUA: heat release rate per unit area

ICC: International Code Council

ICEV: internal combustion engine vehicle

ICP-OES: inductively coupled plasma-optical emission spectrometry

ICP-MS: inductively coupled plasma mass spectrometry

IDLH: Immediately Dangerous to Life and Health

IFC: International Fire Code

IMC: International Mechanical Code

INERIS: National Institute for the Industrial Environment and Risks

IT: information technology

kW: kilowatt

kWh: kilowatt-hour

LCO: lithium-cobalt

LEL: Lower Explosive Limit

LFL: Lower Flammability Limit

LFP: lithium-iron-phosphate

Li-ion: lithium-ion

LMO: lithium-manganese-oxide

LOD: limit of detection

LTO: lithium-titanium-oxide

MJ: megajoule

MLR: mass loss rate

MP2: MegaPack 2

MS: mass spectroscopy

MSS: micro-soot sensor

NCA: nickel-cobalt-aluminum

NDIR: non-dispersive infrared sensor

NFPA: National Fire Protection Association

NIOSH: National Institute for Occupational Safety and Health

NIST: National Institute of Standards and Technology

NMC: nickel-manganese-cobalt

NOAEL: No Observed Adverse Effect Level

NOEL: No Observed Effect Level

OC/EC: organic carbon/elemental carbon

OCV: open circuit voltage

OSHA: Occupational Safety and Health Administration

OSB: oriented strand board

OSHA: Occupational Safety & Health Administration

PACs: Protective Action Criteria for Chemicals

PAH: polycyclic aromatic hydrocarbons

PBDD/F: polybrominated dibenzo-p-dioxins and furans

PC: propylene carbonate

PCB: polychlorinated biphenyls

PCDD: polychlorinated dibenzo-p-dioxins

PCDD/F: polychlorinated dibenzo-p-dioxins and furans

PE: polyethylene

PEL: Permissible Exposure Limit

PET: polyethylene terephthalate

PFAS: per- and polyfluoroalkyl substances

PM: particulate matter

PMMA: polymethyl methacrylate

PN: particle number

PTFE: polytetrafluoroethylene

ppm: parts per million

PU: polyurethane

PVC: polyvinyl chloride

PVdF: polyvinylidene fluoride

RISE: Research Institutes of Sweden

SBI: Single burning item

SCC: Standards Council of Canada

SOC: state of charge

SPSS: solid particle sampling system

STP: standard pressure and temperature

SVOC: semi-volatile organic compound

TEEL: Temporary Emergency Exposure Limits

THR: total heat released

TR: thermal runaway

UFL: upper flammability limit

UL: Underwriters Laboratories

V: volt

VOC: volatile organic compound

Wh: watt-hour

1. Introduction

1.1. Rationale

Over the past decade, there have been numerous thermal runaway events in outdoor, large-scale, lithium-ion (Li-ion) battery energy storage system (BESS) installations; however, quantification of the human health impact of these events has not been heavily investigated. Li-ion technology development and implementation has advanced ahead of comprehensive industry knowledge of hazards like thermal runaway events. Moreover, within the firefighter and first responder community, there are no standard methods for handling Li-ion battery fires. Characterizing health impact allows firefighters and first responders to better respond to thermal runaway events, whether it be operating distances from the incident or issuing shelter-in-place and evacuation orders.

The primary objective of this research was to develop a methodology for characterization of the health impact of outdoor, large-scale, Li-ion BESS thermal runaway events. This was accomplished through fire and plume dispersion modeling based on data obtained from industry research and historical events. For the purposes of this research, a large-scale Li-ion BESS was defined as a utility or commercial or industrial scale Li-ion energy storage installation system with a unit capacity of 500 kWh or more. The primary research objective was accomplished through a literature review, plume dispersion modeling, and a risk analysis. The literature review served to identify and summarize the existing industry data on emissions and yields from Li-ion batteries during flaming and non-flaming thermal runaway. Plume dispersion modeling of Li-ion BESS thermal runaway events was performed, adjusted to various weather conditions. The findings from

the literature review and modeling were used to conduct a risk assessment and gauge the impact of Li-ion BESS fires on human health. The findings from this research demonstrate a methodology that can be used in site-specific risk assessment and hazard mitigation analyses.

1.2. Approach

1.2.1. Literature Review of Lithium-ion BESS Fire Incidents

A literature review of peer-reviewed studies was conducted to identify a) the health impacts of large-scale Li-ion BESS thermal runaway incidents, b) factors controlling the degree of impact of large-scale Li-ion BESS thermal runaway incidents, and c) current modeling practices for modeling plume dispersion. Data was collected and analyzed to address the following questions:

- What gas yields are typical for large-scale Li-ion BESS thermal runaway events, and what factors influence them, e.g., cell chemistry?
- How are yields normalized, e.g., grams of gas per grams of fuel consumed, liters of gas per Wh?
- How do plume constituents and yields differ for flaming and non-flaming thermal runaway events?
- What are representative heat release rates (HRR) and mass loss rates (MLR) for large scale Li-ion BESS units, and what is the typical duration of an event?
- What factors influence propagation of thermal runaway or flaming conditions to other cells, e.g., cell chemistry?

Findings from historical incidents that have occurred globally are also included. The 2021 Victoria Big Battery fire in Australia, the 2022 Moss Landing fire in the California, and the 2023

Queensland battery fire in Australia, amongst others, were reviewed. Data from Underwriters Laboratories, UL 9540A, Battery Energy Storage System (ESS) Test Method was also evaluated. Historical incidents and UL 9540A testing data was used to address the following questions:

- What are the specifications of the BESS systems involved in the incident, i.e. energy and power capacity, dimensions, fire suppression systems?
- What products of combustion were identified as a concern, if any, and how were they measured, e.g., air sampling of HF?
- How was the health impact quantified, e.g., measured concentrations compared to Occupational Safety and Health Administration (OSHA) permissible exposure limits (PEL)?
- What was the scale of the health impact of each fire, e.g., distance between source and impacted areas?
- What were the dominant controlling factors in incident outcomes and/or the severity of the health impacts, e.g., wind direction, wind speed, other weather conditions, plume dynamics, material burning?

The review of current modeling practices for modeling plume dispersion sought to address the following questions:

- What software and practices are typically used in plume modeling, and have they been validated?
- What are the required inputs, and what are the outputs?
- What are the limitations of each program?

The findings from the modeling review informed the model selection for the plume dispersion modeling.

1.2.2. Modeling BESS Plume Dispersion during Thermal Runaway

Modeling of plume dispersion, as the result of a thermal runaway event in a large-scale, outdoor Li-ion BESS installation, was performed to determine the impact of the plume on public health. The purpose of this task was to demonstrate how the methodology can be used by consulting engineers to conduct a site-specific hazard assessment. Further, the modeling was performed to identify factors the consulting engineer should consider when modeling a BESS fire. The modeled hazard scenarios involved a non-flaming and a flaming thermal runaway event contained to a single BESS unit. The models included a bounding analysis for wind and temperature using minimum, average, and maximum conditions expected in areas of the country where BESS installations are most prevalent. Lithium-iron-phosphate (LFP) and nickel-manganese-cobalt (NMC) cell chemistries were evaluated and associated HRR, MLR, and gas yields were determined using UL 9540A data and industry research data gathered in Task 1. Model outputs were analyzed to address the following questions:

- What are the concentrations of gases and particulates at various distances and heights, and for what duration?
- How do wind speed and ambient temperature conditions impact plume height and gas dispersion?
- How do flaming combustion and heat release rate impact plume behavior?

1.2.3. Risk Analysis of Health Impact

The risk analysis involved reviewing the results of the plume dispersion models to determine the health and environmental impact of the modeled scenarios. The model results were analyzed to address the following questions:

- At what distances, under various weather conditions, do gas/heavy metal concentrations exceed OSHA, the U.S. Environmental Protection Agency (EPA) and/or industry established environmental and health thresholds?
- What are the safe operating distances for fire service personnel e.g., where should hot, warm, and cold zones be established on the fireground?
- What are safe distances for the public during an event e.g., when should emergency personnel consider shelter-in-place or evacuation?
- If a thermal runaway event occurred, how far would a large-scale lithium-ion BESS system need to be setback to have no significant impact on a community?

2. Background

The basic components of a Li-ion battery consist of an anode, cathode, separator, electrolyte, binder, and packaging or housing materials. A typical breakdown of the material composition of a Li-ion battery is shown in Table 1.

Table 1. Materials containing hydrocarbons in a typical Li-ion battery cell (Hill, 2020)

Battery Component (containing hydrocarbons)	Percent of Total Battery Mass [%]
Binders	2-5
Electrolyte	8-18
Separator	2-5
Packaging and containment (i.e. PE, PET)	3-25

PE: polyethylene
PET: polyethylene terephthalate

The electrolyte typically consists of an organic solvent, a lithium salt, and a variety of additives (Andersson et al., 2016). Common organic solvents include ethylene carbonate (EC), diethyl carbonate (DEC), or dimethyl carbonate (DMC), and a common lithium salt is hexafluorophosphate ($LiPF_6$) (Andersson et al., 2016). An example of a typical binder material is Polyvinylidene fluoride (PVdF) (Andersson et al., 2016).

One of the main differences in Li-ion battery cells is the chemistry used for the cathode. Typical cathodes are composed of NMC, LFP, lithium-cobalt (LCO), nickel-cobalt-aluminum (NCA), and lithium manganese oxide (LMO) (Hill, 2020). Other cathodes include lithium titanium oxide (LTO). Li-ion battery cells are composed of the housing, separator, electrolyte, cathode and anode foils, and the cathode and anode active materials.

There are three typical types of Li-ion battery cells: pouch, cylindrical, and prismatic. Pouch cells are of flexible construction utilizing a metalized polymer film, cylindrical cells are

constructed with a sealed aluminum “can” exterior, and prismatic cells are constructed with an aluminum casing in a rectangular shape (Hill, 2020).

Hill (2020) summarized thermal runaway of a Li-ion cell in open air into the following three stages:

1. Due to voltage or temperature instability, the cell's internal temperature rises which causes gases to be emitted from the thermal decomposition of the electrolytes in the cell.
2. The voltage of the cell drops to zero and a direct internal short occurs with the anode and cathode, which initiates thermal runaway. Flames may or may not be present.
3. If sufficient oxygen is present, a secondary fire can occur because of the thermal runaway condition, resulting in the ignition of the surrounding battery materials such as electrolyte, polymers, and plastics.

Hill (2020) also described the gases released before, during, and after a thermal runaway event. Prior to thermal runaway, ethanol, and ethane, as well as other hydrocarbons are produced. During the thermal decomposition of the electrolyte, typically the effluent is a mixture of ethylene carbonate compounds and $LiPF_6$. Gases produced during the "secondary fire" are like those of a fire involving typical plastics and include: H_2, CO, HCl, HCN, and HF, as well as other hydrocarbons. Hill (2020) states that, generally, the composition of gases released during a thermal runaway event are similar across Li-ion cell chemistries, forms, and manufacturers, and the yield of gases can validly be assumed to be proportional to the electrolyte mass in the cell.

Most Li-ion battery cells utilize an electrolyte salt containing fluorine with the most common salt being lithium hexafluorophosphate ($LiPF_6$). When heated under dry conditions $LiPF_6$ will decompose into LiF and PF_5.

$$LiPF_6 \rightarrow LiF + PF_5$$

However, in the presence of water, or humidity, the decomposition reactions include hydrogen fluoride and are as follows:

$$LiPF_6 + H_2O \rightarrow LiF + POF_3 + 2HF$$

$$PF_5 + H_2O \rightarrow POF_3 + 2HF$$

In comparing the quantities of HF produced by LFP cells and other cathode chemistries, the total HF produced has been found to be similar, despite the observation that other cathode chemistries, such as NMC/LMO, produce overall a much higher volume of gas, not limited to HF (Sturk, 2019). This can be contributed to the greater production of hydrocarbon gases, such as CO and CO_2, which are influenced by the oxygen release of the decomposition of the NMC/LMO cathodes.

2.1. Industry Installation Standards

There are several standards for BESS design and installation, including NFPA 855 and Chapter 12 of the International Fire Code (IFC). NFPA 855 was first introduced in 2020 by the National Fire Protection Association (NFPA) and addresses the installation requirements for energy storage systems at certain capacities. Chapter 9 focuses on electrochemical energy storage systems (ESS), including systems utilizing Li-ion cells. The current version of NFPA 855 is the 2023 edition. The IFC is developed and maintained by the International Code Council (ICC). Chapter 12 was added to the IFC in 2018 to address the installation, operation, maintenance, and decommissioning of energy systems. Section 1207 focuses on Li-ion BESS specifically. The current version of the IFC is the 2024 edition. The IFC defines Li-ion BESS as an ESS with capacity exceeding 20 kWh.

Chapter 9 of NFPA 855 requires that outdoor ESS installations must be listed to UL 9540, including Li-ion BESS systems. A fire code official approved hazard mitigation analysis must be completed for existing Li-ion BESS installation not listed with UL 9540. If the outdoor installation is located less than or at 100 feet from exposures, the total capacity of a Li-ion BESS installation cannot exceed 600 kWh. Locations that are "remote" (over 100 feet from exposures) may exceed 600 kWh in total capacity. NFPA 855 (2023)- Table 9.5.2 provides the relevant guidelines for the various components of an outdoor ESS, as shown in Table 2. There are specific requirements for rooftop, garage, and mobile outdoor ESS installations, as well.

Table 2. NFPA 855 (2023) Outdoor stationary ESS installation requirements

Compliance Required	Remote Locations	Locations Near Exposures	Reference
Administrative	Yes	Yes	Chapters 1-3
General	Yes	Yes	Sections 4.1-4.7
Maximum Size	Yes	Yes	9.5.2.4
Clearance to Exposures	N/A	Yes	9.5.2.6.1
Means of Egress Separation	N/A	Yes	9.5.2.6.1.7
Walk-in Units	Yes	Yes	9.5.2.3
Vegetation Control	Yes	Yes	9.5.2.2
Enclosures	Yes	Yes	4.6.12
Size and Separation	No	Yes	9.4.2
Maximum Stored Energy	No	Yes	9.4.1
Smoke and Fire Detection	Yes	Yes	9.6.1
Fire Control and Suppression	Yes	Yes	9.6.2
Water Supply	Yes	Yes	9.6.3
Signage	Yes	Yes	4.7.4
Occupied Work Centers	Not Allowed	Not Allowed	9.5.1.2.1
Technology-Specific Protection	Yes	Yes	9.6.5

Fire suppression within outdoor walk-in units must be provided in accordance with Section 4.9, unless the installation is in a remote location and the ESS owner and fire code official agree that it is not required. Li-ion ESS, specifically, are required to have thermal runaway protection and explosion control in accordance with Sections 9.6.5.5 and 9.6.5.6. Thermal runaway protection must be evaluated as part of the UL 1973 or UL 9540 listing. The explosion control for Li-ion

BESS walk-in units must include explosion prevention compliant with NFPA 69 or deflagration venting compliant with NFPA 68. However, explosion control is not required if approved by the fire code official based on a review of fire and explosion testing of the ESS, such as UL 9540A, and a deflagration hazard study has demonstrated that the flammable gas concentrations cannot exceed 25% Lower Flammability Limit (LFL). Fire and explosion testing, such as UL 9540A, must include evaluation of the deflagration mitigation measures integrated into the BESS.

IFC (2024) Section 1207 requires that all Li-ion BESS be UL 9540 listed. Enclosures must be made from noncombustible materials, and combustible materials cannot be stored inside ESS areas or units. Maximum enclosure size and separation requirements are provided in Section 1207. The maximum allowable capacity of a Li-ion BESS is 600 kWh; however, that quantity can be exceeded provided that a fire code official -approved hazard mitigation analysis and large-scale fire testing in accordance with UL 9540A are performed. The hazard mitigation analysis requires the following:

- "Fires will be contained within unoccupied ESS rooms or areas for the minimum duration of the fire resistance-rated separations identified in Section 1207.7.4."
- "Fires involving ESS will allow occupants or the general public to evacuate to a safe location. (Material based on NFPA 855 2023 Ed.)" (ICC, 2024)

If the outdoor installation is remote (over 100 feet from exposures), the maximum capacities for the whole system and individual units do not apply. The IFC provides Table 1207.8, which is similar to NFPA's Table 9.5.2. There are no significant differences between the applicable sections in NFPA 855 and Section 1207 of the IFC for outdoor installations. A hazardous exhaust system in accordance with Section 502.8 of the International Mechanical Code (IMC) must be provided

if the ESS has the potential to release toxic gases during normal use conditions. This does not include release of toxic gases during abnormal or failure conditions, such as thermal runaway. Walk-in units must be protected by an automatic fire suppression system. Li-ion ESS, specifically, are required to have thermal runaway protection and explosion control complying with Section 911, unless explosion control is not required by the fire code official, based on UL 9540A testing.

Unlike NFPA 855, the IFC does not include a provision for existing Li-ion BESS with a fire code official-approved hazard mitigation analysis. Both the IFC and NFPA 855 include provisions for remediation and emergency response. Both codes require that ESS units can have a maximum capacity of 50 kWh and must be spaced a minimum of three feet apart unless the outdoor installation is remote. Smoke detection or radiant heat flux sensors in the area in accordance with NFPA 72 is required by both codes.

2.2. Common Thermal Runaway Quantification Methods

2.2.1. Heat Release

Heat release of Li-ion batteries can be quantified in several different ways. If the heat of combustion is known, mass loss can be measured and multiplied by the heat of combustion to calculate HRR. In cases of complete combustion, mass loss can calculate HRR with an error of less than 10%. For incomplete combustion, this method will overestimate HRR as CO production releases less energy than CO_2 production (Biteau et al., 2008). However, it can be difficult to use this method due to the unknown material composition.

Instead of calculating the heat of combustion for the Li-ion batteries, heat release is often quantified through oxygen consumption calorimetry. Oxygen consumption calorimetry calculates

the heat release rate under the assumption that the heat of combustion per unit mass of consumed oxygen is approximately 13.1 kJ/g of O_2 (Biteau et al. 2008). Although the oxygen consumption method is widely used, it cannot capture the HRR during non-flaming thermal runaway and is more suited to combustion (Mayonado et al. 2024). The cone calorimeter, single burning item apparatus, and the Tewarson calorimeter typically utilize oxygen consumption calorimetry to measure heat release rate (Mayonado et al., 2024).

HRR can also be calculated through the ratio of CO and CO_2 mass produced. This method is called carbon dioxide generation calorimetry and relies on balancing the chemical reaction for incomplete combustion. The heat of combustion per unit mass of produced CO_2 is relatively constant at 13.3 kJ/g. The heat of combustion per unit mass of produced CO is also relatively constant at 11.1 kJ/g. The HRR can be calculated using the CO_2 or CO production rate (Biteau et al. 2008). This method has been favored over the oxygen consumption method for quantifying thermal runaway HRR because oxygen consumption does not account for the gases produced during thermal runaway. Additionally, oxygen consumption does not account for the variability of the Li-ion battery composition and its influence on stages of fire development (Ditch & Zeng, 2020). The cone calorimeter and Tewarson apparatus can use carbon dioxide generation calorimetry (Biteau et al. 2008).

Several common fire testing apparatuses include the cone calorimeter, single burning item (SBI) apparatus, Tewarson apparatus, and the accelerating rate calorimeter (ARC). The cone calorimeter is a bench-scale fire test designed to measure combustion characteristics of small samples. The sample is mounted on top of a load cell and heated by a cone-shaped radiator. The sample is open to the ambient atmosphere and gas is collected by an exhaust hood located above

the sample and cone radiator (NIST, 2024). The SBI is a medium-scale apparatus that was designed to characterize combustion characteristics of building products when exposed to a single burning item. The specimen is mounted on a trolley and positioned in an enclosure beneath an exhaust hood connected to the gas sampling system. The burning item is modeled by a 30-kW propane flame (van Mierlo, 2005). The fire propagation apparatus, otherwise known as the Tewarson apparatus, is a bench-scale fire test where the sample is mounted on a load cell and enclosed in a quartz tube that restricts the combustion area. The quartz tube is surrounded by four infrared heaters and attached to a hood connected to the gas sampling system (Biteau et al., 2009). The ARC is a bench-scale fire test designed to simulate a worst-case scenario where there is no heat exchange with the surroundings. The specimen is placed in a spherical vessel that is heated through a tube. The vessel is placed inside of an insulated containment vessel (Netzsch, 2019). Mayonado et al. (2024) note that the fire testing method can cause variations in peak HRR data when testing the same specimen.

2.2.2. Toxic Gas Quantification

This section describes several common methods to quantify toxic gases. Fourier Transform infrared spectroscopy (FTIR) is a technique used to identify organic, polymeric materials, and some inorganic materials through the measurement of infrared spectrum absorption and emissions. The spectrometer collects data over a wide spectral length and converts it to an infrared spectrum using the Fourier Transform. The different wavelengths in the spectrum correspond with different gases. This method is preferred over classic dispersive spectroscopy, as it can analyze multiple gases at once and the signal produced is stronger (Andersson et al. 2013).

Non-dispersive infrared (NDIR) sensors are gas sensors consisting of a light source, detector and a filter allowing only infrared light to pass into the detector. The light is either absorbed or not absorbed by the gases. The Beer-Lambert law can then be used to calculate the wavelength of the detected infrared radiation. NDIR sensors are often used for measurements requiring high selectivity, sensitivity, and low power consumption. The absorption spectra of most volatile organic and inorganic gases of interest fall within the infrared spectrum, including CO, CO_2, NO, and NO_2. NDIR sensors are more inexpensive and simpler to operate compared to FTIR; however, NDIR sensors cannot analyze as many species at once compared to FTIR (Jha, 2022).

Colorimetric gas detector tubes use a reagent to induce a color change in the tube when it interacts with the sample gas. Reagents vary depending on the specific gas that is being analyzed. A pump draws the sample gas into the tube, which is marked with concentration values. Colorimetric tubes are simple to operate, inexpensive, and portable. However, they are subject to error as two gases may cause a similar color change if they have similar properties (Kawamura et al., 2021). Additionally, the concentration readings rely on visual indicators, which are more subjective.

Ion chromatography is a form of liquid chromatography that measures ions based on their interaction with resin. The sample is passed through the top of a pressurized column. Eluent, an ion extraction liquid, is flowed top-down in the column to separate the sample into ions. Different ions will separate at different rates down the column. Retention time of each species is used to quantify concentration (Bruckner, 2006).

Gas chromatography is an analytical method in which the sample is dissolved in a solvent and vaporized to separate each species. A dry, inert, oxygen-free gas then carries the species through

a heated column for quantification, usually through the effect of thermal conductivity on mass flow in a separation column. Gas chromatography can be paired with other gas quantification methods, such as gas chromatography mass spectroscopy (GC-MS), gas chromatography thermal conductivity detection (GC-TCD), and flame ionization detection (LibreTexts Chemistry).

Mass spectroscopy (MS) quantifies gases based on mass to charge ratio. The sample is bombarded by electrons which ionize and fragment the sample. Ions are passed through a mass analyzer and sorted by mass to charge ratio. The relative peaks determine concentration. A common mass analyzer utilized in GC-MS is a quadruple-ion trap analyzer. The quadruple MS holds ions for long periods of time for analysis (LibreTexts Chemistry). Inductively coupled plasma mass spectroscopy (ICP-MS) is a form of mass spectroscopy that separates the ions via plasma. A liquid sample is nebulized and transferred into argon plasma, which decomposes and ionizes the species (Wilschefski & Baxter, 2019). Mass spectrometers are able to continuously scan and quantify gases; however, samples may thermally degrade before they reach the mass analyzer (LibreTexts Chemistry).

The operating principle of thermal conductivity detection (TCD) is measuring the change in the thermal conductivity of the carrier gas. The sensor contains an inlet, outlet, and a heating wire. The carrier gas and sample change the temperature of the heated wire upon entering. Thermal conductivity can be calculated from the temperature and resistance of the heated wire. Typically, the carrier gas will also be monitored by itself for calibration. TCDs are capable of analyzing both organic and inorganic species; however, it has lower sensitivity compared to other detection methods and a dependency on flow rate and concentration (LibreTexts Chemistry).

Flame ionization detection (FID) is a form of gas chromatography used to detect hydrocarbons. The detector provides little to no response for inorganics, CO, CO_2, and water. The FID burns a pure hydrogen flame. Below the flame, sample gas is introduced, mixed with H_2, and passed through the flame. This process removes the hydrogen from the sample gas via decomposition and then ionizes the remaining carbon. The carbon is counted using an electrometer (Hinshaw, 2005).

Inductively coupled plasma optical emission spectroscopy (ICP-OES) quantifies gas ions by measuring the energy emitted by energized ions. Gases are ionized via argon plasma in the same process performed in ICP-MS. Energized ions emit photons until they return to their de-energized state. The photons have wavelengths that correspond to the species (ThermoFisher Scientific).

3. Literature Review

The findings of the literature review are summarized below. Studies that were not publicly available or did not have an English translation were excluded.

3.1. Peer Reviewed Publications

The first goal of the literature review was to identify thermal runaway characteristics of Li-ion batteries, including thermal runaway behavior, gas emission composition and yields, HRR/MLR, total heat released, total gas produced, and thermal runaway and cell gas venting temperature, as well as how these characteristics varied between cell chemistry, state of charge (SOC), cell geometry, number of cells and their arrangement, cell capacity, and flaming or non-flaming conditions. Google Scholar was utilized to identify literature that included the keywords "lithium-ion battery," "thermal runaway," "flaming," "non-flaming," "health impact," "toxic gases," "emissions yields," and "BESS testing." Publications that did not quantify these characteristics or identify the methods of quantification were excluded. The literature review primarily focused on determining characteristics for LFP and NMC cells. While some studies evaluated cell chemistries outside of LFP and NMC cells, that data was not considered for the modeling inputs.

3.1.1. Amano et al., 2022

Amano et al. (2022) performed 19 tests of NMC Li-ion battery cells in order to quantify the combustible and toxic gases produced during thermal runaway. The tests utilized NMC pouch cells with a 10 Ah/37 Wh capacity and a mass of 178 g and NMC pouch cells with a 32 Ah/118 Wh capacity and a mass of 590 g. Tests were of single cells or cell arrays consisting of two cells. Two series of tests were conducted. In Test Series 1, thermal runaway was initiated via a glow plug,

and in Test Series 2, thermal runaway was initiated via a heating plate. All tests were conducted in a 100 L sealed chamber, with ambient air. The SOC of the cell(s) varied between tests. Temperature and pressure measurements inside the chamber were used to determine the total amount of gas released from the cells. Gas samples were obtained from the chamber after the test was complete and were analyzed via FTIR. A thermal runaway onset temperature was defined as the temperature at which an obvious exothermic effect could be measured. A reaction temperature was defined as the maximum temperature achieved at the cell surfaces during the test. Using the time difference between these two temperature parameters, an effective period of thermal runaway was determined.

The authors did not determine if flaming combustion was achieved for each test. Table 3 presents the average concentrations of the measured toxic vent gases; where multiple tests are grouped together, the average value across the tests is indicated.

Table 3. Vent gas emissions from NMC pouch cells (Amano et al., 2022)

Test ID	Cell Capac. [Wh]	No. Cells	SOC [%]	TR Onset Temp. [K]	TR Duration [s]	Mass Loss [%]	Gas Release Rate [mol/s]	Total Gas Production [L/Ah]	Concentration [ppm]		
									HF	CO	HCN
Series 1											
1-3	37	1	80-89	344	9	23	0.64	1.6	7	45500	50
4	37	4	90-100	345	51	28	0.12	1.8	10	238240	48
Series 2											
1-3	37	1	30-50	472	605	21	<0.01	1.5	0	7970	130
4-6	37	1	80-89	452	545	27	0.07	1.75	0	12650	166
7-9	37	1	90-100	450	14	45.5	0.87	2.9	0	33970	147
10-12	37	2	90-100	393	28	42	0.56	2.8	0	101290	137
13-15	118	1	90-100	487	44	47	0.55	3.2	0	136120	287

Capac: Capacity
Temp: Temperature
TR: thermal runaway

The total gas production was observed to increase with increasing SOC. The authors noted that the tests involving one 10 Ah cell and two 10 Ah cells at 90-100% SOC had similar normalized gas production volumes despite the increase in cell capacity. They noted that this may have been due to the oxygen limited environment. HF was not detected in Test Series 2, however the authors noted that this may have been due to the increased dilution factor used in Test Series 2 (1:100) compared to that used in Test Series 1 (1:10). CO concentrations were observed to increase with increasing cell SOC and increased capacity. CO_2 measurements were not reported due to strong interference with other compounds.

3.1.2. Amano et al., 2023

Amano et al. (2023) performed 31 tests of NMC Li-ion battery cells in order to quantify the combustible and toxic gases produced during thermal runaway. Three series of tests were conducted. Test Series 1 utilized NMC pouch cells with a 2.5 Ah/9.25 Wh capacity and a mass of 58 g. Test Series 2 utilized NMC pouch cells with a 10 Ah/37 Wh capacity and a mass of 178 g, as well as NMC pouch cells with a 32 Ah/118 Wh capacity and a mass of 590 g. Tests were of single cells or arrays of two cells. All tests were conducted in a sealed chamber, with ambient air. The chamber for Test Series 1 had a volume of 10 L, the chamber for Test Series 2 had a volume of 100 L, and the chamber for Test Series 3 had a volume of 45 L. The SOC of the cell(s) varied between tests for Test Series 1, while all cells in Test Series 2 were charged to 100% SOC. Test Series 1 and 2 initiated thermal runaway via heating plates. Test Series 3 initiated thermal runaway via overcharging. Temperature and pressure measurements inside the chamber were used to determine the total amount of gas released from the cells. Gas samples were obtained from the chamber every 10 seconds and analyzed via FTIR.

For cells at a SOC of 50% or less, the authors determined that ignition of the vent gases did not occur. The publication did not indicate if ignition occurred during the 80 and 100% SOC tests in Test Series 1. Ignition of vent gases was determined for most Test Series 2 tests. Table 4 presents the average concentrations of the measured toxic vent gases; where multiple tests are grouped together, the average value across the tests is indicated. Gas concentrations for Test Series 3 were not reported.

Table 4. Vent gas emissions from NMC pouch cells (Amano et al., 2023)

Test ID	Cell Capacity [Wh]	No. Cells	SOC [%]	Flaming?[1]	Total Gas Production [L/Ah]	Concentration [ppm]			
						HF	CO_2	CO	HCN
Series 1									
1-3	9.25	1	0	No	≤0.4	11	0	8700	37
5-7	9.25	1	30	No	1.2	8	0	8489	38
9-11	9.25	1	50	No	1.2	15	10000	12300	84
13-15	9.25	1	80	Yes	2.4	17	286400	56400	170
17-19	9.25	1	100	Yes	2.6	18	480570	67700	165
Series 2									
21	37	1	100	Yes	1.65	<LOD	-	30980	110
22	37	1	100	Yes		<LOD	-	29220	100
23	37	1	100	Yes	4.2	<LOD	10000	41700	230
24	37	2	100	Yes	2.15	<LOD	-	67500	150
25	37	2	100	Yes		<LOD	-	68500	180
26	37	2	100	Yes	3.6	<LOD	-	168500	80
27	118	1	100	Yes	3.2	<LOD	-	136160	281
28	118	1	100	Yes		<LOD	-	124100	200
29	118	1	100	Yes		<LOD	-	148100	380

LOD: Limit of Detection

[1]Due to experiments being conducted in an enclosed vessel, flaming combustion could not be confirmed during the test. Flaming status indicated in this table reflects the beliefs of Amano et al. (2023), based on post-failure analysis of the cells and as communicated in the publication and private communication with the authors of this report.

A trend in HF production in relation to cell SOC could not be identified, but it was observed the highest average concentration (18 ppm) was produced during tests of cells at 100% SOC. HF was not detected in Test Series 2, however the authors noted that this may have been due to

increased dilution because of the increased size of the test reactor (100 L) compared to that used in Test Series 1 (10 L). HCN concentrations were observed to increase with increasing cell SOC.

3.1.3. Archibald 2021

In this dissertation from the University of Texas at Austin, Archibald conducted a series of experiments with single Li-ion cells, as well as cell arrays and modules to determine gas release and thermal runaway propagation behavior.

The first series of single-cell experiments were conducted using LCO pouch cells with a 5 Ah/18.5 Wh capacity at 100% SOC. The cells each had a mass of 90.2 g. Two tests were conducted in open air, and one was conducted with an inert pressure vessel. The cells were externally heated with block heaters on either side of the cell. The tests showed that the cells began to slowly vent approximately 1000 seconds before the rapid heating associated with the onset of thermal runaway. The author estimated that approximately 15% of the total vent gas was released during this incipient period. Thermal runaway was initiated when the heater-cell interface temperature reached 185 to 196°C. During the test, temperatures as high as 900°C were measured close to an emerging hot gas jet.

Cell array experiments were conducted with the same LCO pouch cells utilized in the single-cell experiments described above, as well as with 10 Ah LCO pouch cells. The 10 Ah cells had a mass of 208.9 g. Tests included either 5-cell arrays or 10-cell arrays, with the cells clamped together linearly with no insulation or spacing between them. A cartridge heater was utilized to initiate localized heating at the center of the initiating cell. The arrays were contained in a pressure vessel purged with nitrogen. For the 5 Ah arrays, the tests showed that the average time for cell venting was 11 seconds, and the average time for thermal runaway propagation between cells was

15 seconds. Upper gas temperatures in the chamber reached a maximum of approximately 150°C in the 10-cell, 5 Ah array test and approximately 130°C in the 10-cell, 5 Ah array test. For the 10 Ah arrays, the tests showed that the average time for cell venting was 14 seconds, and the average time for thermal runaway propagation between cells was 22 seconds. The author attributed the longer vent and propagation times to the increased thickness of the 10 Ah cells compared to the 5 Ah cells. Upper gas temperatures in the chamber reached a maximum of approximately 200°C in the 10-cell, 10 Ah array test. Archibald (2021) found that the final pressures and upper gas temperatures in the 10-cell, 5 Ah array and the 5-cell, 10 Ah array were nearly identical, and thus, concluded that the volume of vent gases and heat release can generally be normalized by watt hour capacity; additional testing was recommended to confirm the trend.

In comparing the single-cell tests to the cell array tests, it was found that single cells experience a longer pre-heat period, and the period of intense venting is faster than a cell that achieves thermal runaway via cell-to-cell propagation. The single cells also vented gas during the pre-heat period before thermal runaway. Conversely, the cells in the array did not have time to vent gases , because the preheat period lasted only a few seconds.

In the second series of single-cell experiments, tests were performed in a burn structure and in a pressure vessel purged with nitrogen. The cells used were NMC prismatic cells with a nominal capacity of 94 Ah/346 Wh and a nominal voltage of 3.68V. Cells were at 100% SOC and had a mass of 2100 g. Three single-cell, open air tests were conducted in the burn structure. In the first test, the cell was heated with a cartridge heater. This method caused the cell to rupture and project across the room, compromising the usefulness of the collected data. The next two tests utilized electric heaters on the large face of the cell with a gradual heating rate of 5°C/min. In these two

experiments, the cell vent opened and started to release gas 368 seconds and 292 seconds prior to thermal runaway and intense venting. The temperature of the gas measured immediately above the vent reached a maximum of 750°C during the intense venting period. The cell had a total mass of approximately 1350 g at the end of the test (750 g mass loss).

One single-cell, NMC test was conducted in the inert pressure vessel. The test utilized an electric heater on the large face of the cell, with a gradual heating rate of 5°C/min. Measured gas temperature and pressure were used to calculate the total volume of gas released from the cell and the gas release rate. The total volume of gas released was found to be 221.6 L at standard pressure and temperature (STP). The authors normalized this gas volume by cell energy capacity with a calculated value of 0.64 L/Wh. The total venting time was 7 seconds, and the peak gas release rate was calculated to be approximately 65 L/s. The composition of the vent gas was determined via a gas chromatography thermal conductivity detector (GC-TCD) calibrated to measure calibrated to measure H_2, N_2, CO, methane, acetylene, ethylene, ethane, propylene/propane, and water. Table 5 below presents the measured gas composition in the single, 94 Ah cell test in the pressure vessel.

Table 5. Vent gas composition of 94 Ah NMC cell in pressure vessel (Archibald, 2021)

Species	% Volume
H_2	30.6
CO_2	29.9
CO	21.3
Methane	7.2
Ethylene	5.6
Propane/Propylene	2.0
Ethane	1.8
Other	1.6

Archibald (2021) also conducted several module level experiments comprised of the same 94 Ah, NMC cells used in the single-cell tests described above. The module consisted of fourteen

cells, connected in series, within a polycarbonate casing. Thermal runaway was initiated via the same electric heater method used in the single-cell experiments. One module test was conducted in open air and two were conducted inside a steel rack enclosure to represent a BESS installation. The steel enclosure was closed on all sides, including the top side, with vent openings only at the top and bottom of the front side. Two noncombustible "dummy' models were installed above the test module within the enclosure.

In the open-air module experiment, a single cell was forced into thermal runaway and propagation subsequently occurred throughout the remaining cells. The authors observed that the failure of cells was generally similar to that observed in the single-cell tests. The initiating cell began to vent, and 77 seconds later, intense venting occurred, ejecting flammable gas and other materials from the cell over a period of several seconds. The flammable gases ignited during this intense venting period. Similar behavior was seen throughout the experiment for each cell as it failed via propagation. Propagation time for the first five cells was on the order of magnitude of minutes; however, as the event progressed, cell-to-cell propagation time decreased so that propagation through the last nine cells occurred over a total time of approximately 250 seconds, or approximately 27 seconds per cell. The total duration from thermal runaway of the initiating cell to completion of thermal runaway of the last cell was approximately 17 minutes. Mass loss measurements indicated that at each intense cell venting event, there was an approximate mass loss of 900 g. Using a time of 5 seconds before thermal runaway and 15 seconds after, the authors calculated an estimated average MLR of up to approximately 45 g/s during a single cell vent event and up to approximately 55 g/s over the period of time at which two cells vented in rapid succession. Between cell venting events, gradual mass losses occurred due to combustion of the module's polycarbonate housing. The total cell mass loss during the test was estimated to be

approximately 12,200 g and the total mass loss of the polycarbonate housing was estimated to be approximately 3,000 g. Gas temperatures within the module reached a maximum of approximately 1180°C.

In the rack module experiments, similar behavior was seen for thermal runaway propagation. The total duration from thermal runaway of the initiating cell to completion of thermal runaway of the last cell was approximately 16.5 minutes, compared to 17 minutes in the open-air test. For all three module experiments, the last 3 cells underwent thermal runaway in a period of 20 to 38 seconds. Gas temperatures within the module and within the rack enclosure reached a maximum of approximately 950°C.

Archibald (2021) also performed a series of tests to evaluate the explosion hazards of Li-ion cells. As part of this series, a test of an array of five, 18.5 Ah, LCO pouch cells in an inert pressure vessel was conducted. This test produced a total of 118.2 L of gas, or 0.35 L/Wh. Table 6 presents the measured gas composition in the 5-cell array test in the pressure vessel.

Table 6. Vent gas composition of 5-Cell LCO array in pressure vessel (Archibald, 2021)

Species	% Volume
Hydrogen	26.8
CO_2	31.9
CO	23.9
Methane	4.8
Ethylene	7.1
Propane/Propylene	2.4
Ethane	1.3
Other	1.8

In a review of 21 studies on gas compositions of Li-ion cell venting incidents at 100% SOC, Archibald found that gas released per nominal capacity was a minimum of 0.12 L/Wh, a maximum of 0.63 L/Wh, and an average of 0.40 L/Wh, across various cell chemistries.

Additional experiments were conducted on modules comprised of cylindrical, Type 26650, LFP cells. The module contained 48 cells arranged with six cells long, four cells wide, and two cells high. The two vertical rows of cells were separated by a thin plastic panel and thin foil current collectors. The module had a total nominal capacity of 568.3 Wh (11.8 Wh per cell) and a total mass of 5300 g. The first experiment was conducted with the module in open-air. Thermal runaway was initiated via a block heater placed under 12 of the bottom cells. These 12 cells were observed to enter thermal runaway within 918 seconds after the first cell vent. Propagation to other cells in the module did not occur for another 305 seconds. The next 14 cells went into thermal runaway over a period of 813 seconds. Analysis of mass loss rates showed that individual cell vent events had an average MLR of 1 g/s to 3 g/s. The cells that experienced higher MLR were determined to be those that partially ejected their contents (i.e., cathode, anode, current collectors). The total mass of the module at the end of the test was approximately 4965 g (335 g total mass loss). No flaming combustion was achieved during the test and post-test evaluation showed that only the 24 lower cells went into thermal runaway. As such, thermal runaway was noted to have propagated horizontally within the module, but not vertically.

The second experiment consisted of only the bottom 24 cells of the module, located within a pressure vessel purged with nitrogen. Thermal runaway propagated throughout the 24-cell array over a period of 909 seconds. The event produced a total of 33.5 L of gas at STP, or 0.12 L/Wh. The total starting mass of the array was 2,080 g and the total mass at the end of the test was 1,566 g (514 g total mass loss). Upper gas temperatures within the chamber reached a maximum of approximately 190°C. Table 7 presents the measured gas composition in the 24-cell array test in the pressure vessel.

Table 7. Vent gas composition of 24-Cell LFP array in pressure vessel (Archibald, 2021)

Species	% Volume
H_2	42
CO_2	24
CO	7.8
Methane	7.6
Ethylene	4.5
Propane/Propylene	3.7
Ethane	1.78
Other	8.62

Comparing the tests involving LMC and LCO cells and those involving LFP cells, Archibald (2021) observed that the LFP tests did not achieve flaming combustion due to the lack of ejected hot material. In the LCO and NMC tests, the cells consistently ejected glowing hot particles, which almost immediately ignited the surrounding gases.

3.1.4. Andersson et al., 2013

The SP Technical Research Institute of Sweden performed experimental testing on Li-ion battery electrolytes to assess the production of HF, PF_5, and POF_3 and the feasibility of using FTIR to measure the gases. In addition, the authors initiated flaming thermal runaway in pouch and cylindrical Li-ion cells, as well as two laptop battery packs, to quantify thermal combustion characteristics method under different heating and combustion conditions. The FTIR spectrometer was a Thermos Scientific Antaris IGS analyzer.

In the first phase of the study, two types of tests were run under a cone calorimeter. The first involved placing the electrolyte materials in an open container and heating them via external radiation. The second type was an extension to these tests where the vapor produced from the thermal decomposition of the electrolyte materials was ignited via an electric sparker. The FTIR sampling port in the exhaust duct was located approximately 20 inches upstream of the radiant

cone. Independent tests were run with different combinations of electrolyte materials and mixtures. $LiPF_6$ salt and two types of solvents, dimethoxyethane (DME) and propylene carbonate (PC), were used in this phase. It was found that evaporation of pure $LiPF_6$ salt and combustion of $LiPF_6$ salt dissolved in both types of solvents produced HF and POF_3 but did not produce PF_5.

The second phase of the study involved tests that injected solvent/salt solutions directly into a propane burner flame. The burner effluents were collected under the cone calorimeter hood, and it is assumed that the FTIR sampling port was in the same location as previous tests. Variations of the test were conducted with different propane/solvent ratios, salt/solvent concentrations, and introduction methods of the solution into the flame. In addition, some tests involved injecting water into the flame as well. The two types of solvents used in this phase were DME and DMC and the salt was $LiPF_6$. It was observed that HF and POF_3 were always present during the combustion of the electrolyte solutions. The HF concentration was 8 to 33 times higher than the POF_3 concentration in each of the tests involving DMC and 53 times higher in the one test involving DME. No reasoning for the difference in the HF/POF_3 ratio was established. Peak concentrations of HF reached as high as 1,500 ppm and peak concentrations of POF_3 reached as high as 158 ppm in the exhaust duct, i.e., close to the source. In addition, no conclusive findings were identified for the impact of water on HF or POF_3 production. PF_5 was not detected in any of the tests. Andersson et al. (2016) identified that the Swedish Work Environment Authority set a maximum allowable concentration of HF in a working environment at 2 ppm and the U.S. National Institute for Occupational Safety and Health (NIOSH) sets the Immediately Dangerous to Life or Health (IDLH) value of HF at 30 ppm but neither of these organizations have established exposure limits for POF_3.

The gas sampling system included a pump to draw in sample gas, filters, and a gas cell. The pouch cells tested were placed in five cell bundles and fastened together with steel wire. The cylindrical cells were placed in a bundle of nine cells and placed in a box made of steel net and silica board. The two laptop battery packs were placed inside a steel net. The experiment was conducted in an SBI apparatus, and a propane burner was utilized to initiate combustion. HRR was measured via oxygen consumption calorimetry. Water mist was applied to Test 3 only. Table 8 shows the test specifications and results for mass loss, heat release, and toxic gas production.

Table 8. Results from testing of Li-ion cells conducted by Andersson et al. (2013)

Test ID	Cell Type	Cell Geometry	No. Cells	Capac. [Wh]	SOC [%]	Total Mass [g]	Mass Loss [g]	Peak HRR [kW]	THR [kJ]	Total HF [g]	Peak HF Prod. Rate [mg/s]	HF Yield [mg/g]
1	LFP	Pouch	5	112	100	1228	346	48	6826	4.9	8.8	14
2	LFP	Pouch	5	112	100	1229	342	44	6645	6.3	7.7	18
3	LFP	Pouch	5	112	100	1229	341	42	7130	5.7	15.4	17
4	LFP	Pouch	5	112	0	1229	353	9.5	7356	11.3	10.2	32
5	LFP	Pouch	5	112	50	1228	354	14	7460	13.9	16.4	39
6	LFP	Cylindrical	9	92	100	735	145	26	2409	2.2	2.9	15
7	Unk	Pack	2x (3x2)	373	100	639	258	50	3036	1.9	1.1	7.3

At the higher SOCs, pouch cells underwent rapid venting of gases, whereas no rapid venting was observed in the lower SOC pouch cell tests. The rapid venting of gases was also observed in the cylindrical cell and laptop battery pack tests. Andersson et al. (2013) noted that the water mist applied in Test 3 did not impact the total amount of HF produced, although it had the potential to shift the chemical kinetics to favor HF production over POF_3.

3.1.5. Barowy et al., 2021

In 2020, UL conducted mock-up installation level BESS tests to assess the impact of water-based and clean agent fire suppression on installation level BESS fires. The tests involved an

initiating unit, two partial target units, and several dummy units all placed in a 20-foot storage container. One target unit was placed directly next to the initiating unit, while the other was placed across from the initiating unit with separation. In the storage container, some walls were made of steel only, while other walls were a combination of steel, oriented strand board (OSB), and gypsum, or a combination of steel, polyurethane (PU), two layers of plywood, and gypsum. The container was equipped with five deflagration vents set to activate at 0.5 psig.

The initiating unit consisted of a rack of nine modules with a total capacity of 28.9 kWh. Each module contained 270, NCA, 18650, Li-ion cells at 100% SOC with a capacity of 99 Ah. The cell level thermal runaway properties are shown in Table 9.

Table 9. Cell level thermal runaway properties (Barowy et al., 2021)

Property	Measurement
Cell vent temperature	130°C
Thermal runaway temperature	204°C
Gas volume	213 L
Gas composition	36.2 v% carbon monoxide; 22.1 v% carbon dioxide; 31.7 v% hydrogen; 10.0 v% hydrocarbons Hydrocarbon breakdown 7.4 v% methane; 0.92 v% ethylene; 0.61 v% ethane; 0.22 v% propylene; 0.04 v% propane; 0.07 v% C4-hydrocarbons; 0.24 v% benzene; 0.03 v% toluene; 0.38 v% dimethyl carbonate
Gas LFL	8.9 v%
Gas UFL	40 v%
Gas P_{max}	93 psig
Gas burning velocity	35 cm/s

UFL: upper flammability limit
P_{max}: maximum pressure

The cells and modules were not electrically connected, meaning no current was running through them. The partial target units held one-third of the initiating unit's capacity, while the

dummy units were empty. One cell in the initiating unit was heated to thermal runaway via film heaters. Tests were run without any suppression (Test 1), with Novec 1230 at 8.5 %vol (Test 2), and with water suppression (Test 3). Tests were terminated by discharging 41 kg of CO_2 into the container when thermal runaway activity subsided, or module temperatures began decreasing.

In Test 1, the initiating cell vented at 23 min 43 s and entered thermal runaway 2 min 22 s later. An off-gas plume was produced and ignited the initiating module 31 seconds after thermal runaway. There was a partial volume deflagration that opened the doors due to pressure, but the vents remained sealed. At this time, the combustible gas detector registered 50% of the lower explosive limit (LEL). The doors were manually closed and flaming subsided 1 min 25 s later. Thermal runaway propagated through all modules in the initiating unit and the left target within 2 hr 50 min of the initial thermal runaway. CO_2 was discharged 2 hr 55 min after thermal runaway initiation; no reignition occurred after CO_2 application.

The incident heat flux exceeded 12.5 kW/m^2, the critical heat flux for ignition of most combustible materials, at the rear wall after thermal runaway propagated to the modules and towards the end of the test and at the left target unit after the doors closed for the rest of the test. The rear and side walls had charring. There were penetrations to the bare steel beneath the plywood on the rear wall. The front target did not have as much exposure to heat flux, likely due to the separation distance.

Table 10 shows the times at which each module underwent thermal runaway. The authors defined thermal runaway as “an immediate temperature increase of more than 400°C, and a sustained temperature above 300°C.” Thermal runaway propagated upward at a rate of one module per 2 to 10 minutes. Downward propagation was slower at a rate of one module per hour.

Table 10. Time to thermal runaway for Test 1 modules (Barowy et al., 2021)

Time [hh:mm:ss]	Time Since Initial Thermal Runaway [hh:mm:ss]	Location
00:26:22	00:00:00	InitUnitMod3
00:40:26	00:14:04	InitUnitMod5
00:46:57	00:20:35	LeftUnitMod4
00:49:04	00:22:42	InitUnitMod4
00:55:47	00:29:25	LeftUnitMod5
00:57:26	00:31:04	LeftUnitMod3
00:58:41	00:32:19	LeftUnitMod6
01:00:55	00:34:33	InitUnitMod6
01:04:26	00:38:04	LeftUntMod7
01:13:37	00:47:15	InitUnitMod7
01:15:10	00:48:48	LeftUnitMod8
01:22:57	00:56:35	InitUnitMod8
01:25:48	00:59:26	InitUnitMod9
01:28:46	01:02:24	LeftUnitMod9
01:54:53	01:28:31	InitUnitMod2
02:08:06	01:41:44	LeftUnitMod2
03:13:48	02:47:26	LeftUnitMod1
03:14:04	02:47:42	InitUnitMod1

The gas concentrations were measured via portable gas detectors inside and outside the storage container for Test 1. Exterior sensors were located on Sides A and B of the container; both pumped, and diffusion sensors were used. The LEL peaked at 83% at 26 min into the initial thermal runaway event. At that point, thermal runaway started to propagate to the left target. The other gases peaked around 60 minutes into the test, except for the interior H_2, CO, and HCN which reached the measuring limit of the detectors shortly after thermal runaway. Volatile organic compound (VOC) concentrations also hit the measuring limit but dropped several times during the test. H_2S remained under 20 ppm both inside and outside the container, but exterior measurements had higher readings than interior measurements. Gas concentrations tended to be higher on Side A, except for LEL.

Thermal runaway was first detected at 28 min 9 s for Test 2. The Novec 1230 system triggered after two smoke detectors were alarmed 55 seconds after thermal runaway. Thermal runaway propagation continued in the initiating module for 7 minutes after suppression. An upper layer of

flammable gases formed and ignited 28 min 32 s after initial thermal runaway. The flames extinguished after 30 seconds, but the gas layer reformed and caused a deflagration 16 min later. The deflagration opened a side and ceiling vent. Thermal runaway propagation began again in Module 4 of the initiating unit. Thermal runaway reached the left target at 1 hr 1 min after the initial thermal runaway. Upward propagation continued at a rate of 1 to 12 minutes per module. At 2 hr 9 min, the door was opened, and a flashover occurred due to the introduction of fresh air. Water was applied manually to reduce the heat release rate, the doors were closed again, and the container was flooded with CO_2. Thermal runaway continued after CO_2 application. By the end of the test, all modules in the initiating unit and the left module had undergone thermal runaway.

The peak heat fluxes at the rear and side walls for Test 2 were comparable to Test 1 due to reignition after suppression. After the Novec 1230 was applied, the heat fluxes and temperatures inside the container decreased. There was a gradual increase after suppression that peaked at flashover. Temperature decreased after CO_2 was applied, but heat flux continued to slowly increase.

For Test 3, thermal runaway initially occurred at 29 min 53 s. After 8 min 49 s, thermal runaway had propagated throughout the initiating module. Ignition and sustained flaming occurred at the same time. The water suppression system turned on 10 min 13 s after the initial thermal runaway. Flaming was suppressed, but cooling the module was not as effective due to the initiating unit's enclosure protecting the modules from direct contact. As a result, partial thermal runaway occurred in three more modules in the initiating unit. Deflagration occurred when the third module went into thermal runaway. Waterflow was stopped 1 hr 36 min into the test. Two more modules in the initiating unit underwent thermal runaway. Eventually, thermal runaway propagated to the

left target. Waterflow was turned back on to see if cooling would prevent further propagation. At 2 hr 29 min, the storage container doors were opened while maintaining suppression. One module at the top of the initiating unit entered thermal runaway.

The temperatures at the rear and sidewall peaked at ignition and were lowered during suppression. After suppression was turned off, both temperature and heat flux increased and peaked once more. The temperatures inside the target units followed a similar pattern. In total, seven modules from the initiating unit and one module from the left target underwent thermal runaway.

The Novec 1230 at 8.5 %vol did not remove sufficient heat to stop thermal runaway concentration. Other studies demonstrated that propagation could be reduced using crossflow at the same concentration but did not completely stop it (Said and Stoliarov, 2021). Tests 1 and 2 had the same extent of thermal runaway propagation and similar rates of propagation. The Novec 1230 only delayed initial propagation from the initiating module. The water suppression in Test 3 lowered the temperatures enough to reduce thermal propagation but did not eliminate it. The modules in Test 1 and Test 2 reached the same magnitude of temperatures, although there was a delay in Test 2. The suppression in Test 3 consistently lowered temperatures when active, but the temperatures would increase after the waterflow was discontinued. Deflagrations occurred in all three tests and were associated with the thermal runaway of a module. It is possible that the gases were ignited due to hot surfaces or sparks caused by thermal runaway, or the electrically powered gas detectors inside the enclosure. However, the vents mitigated the severity of deflagrations. Test 3 saw lower gas concentrations compared to Tests 1 and 2 due to less thermal runaway propagation, but neither suppression system stopped flammable gas accumulation. All three tests

reached the upper flammability limit and greatly reduced oxygen (7 to 10 %vol). CO was measured at 2 to 3 times higher yields than under-ventilated compartment tests containing plastics or PU foam. CO_2 was measured at 2 to 4 times higher than IDLH.

Novec 1230 was insufficient for cooling, but water suppression may be useful for mitigating thermal runaway between units. However, the module-to-module propagation was not affected by suppression. Gas temperature increase can raise the thermal propagation rate exponentially. Separation between units could stop thermal propagation due to less exposure to high temperatures. Thermal runaway is more likely to propagate upwards than downwards, and an event where the bottom module initiates thermal runaway may be more hazardous.

3.1.6. Blum & Long, 2016

In cooperation with the Fire Protection Research Foundation (FPRF), Exponent, Inc. conducted a hazard assessment of Li-ion BESS. The analysis included full-scale fire testing of Tesla Powerpacks at the Tesla test facility in November of 2015. A PowerPack consists of approximately 14,400 cylindrical, 18650 cells, each with a nominal voltage of 3.6V and a capacity of 2.4 Ah. The total capacity of a PowerPack is 100 kWh. Cell chemistry was not indicated in the report, but it is understood that the PowerPack utilizes NMC cells.

The analysis included a literature review which identified that Li-ion battery cells, when subjected to abnormal heating, can vent vaporized electrolyte products and electrolyte decomposition products. The gases released depend on cell composition, SOC, and the cause of cell venting and can include VOCs (such as alkyl-carbonates, methane, ethylene, and ethane), H_2, CO_2, CO, soot, and particulates containing oxides of nickel, aluminum, lithium, copper, and cobalt. The literature review also found that during fires involving Li-ion batteries, NO_x, HCN, and HCl

can be produced, and concentrations of fluoride and chloride may be found in water samples collected after extinguishing Li-ion battery fires. These findings of the literature review were applicable to Li-ion batteries generally, not specifically Tesla equipment.

Full-scale testing of the Powerpack was conducted in two configurations, an internal ignition test and an external ignition test. The internal ignition test was performed by placing cartridge heaters in the center of a pod module, and the external ignition test utilized a propane burner to generate direct flame impingement on the exterior side of the unit. Both tests used 100 kWh Powerpack units at a 100% SOC. Products of combustion were measured via handheld gas sampling units with built-in pumps which drew air samples from the exhaust vent of the unit. The following gases were measured: CO, Cl_2, CH_4, and HF. Heat flux measurements were taken during the test, however the results were deemed to be inaccurate, and therefore, were not considered in the findings of the hazard assessment. A summary of the testing results is presented in Table 11.

Table 11. Testing results from Blum and Long (2016)

	Internal Ignition Test	External Ignition Test
Observations	No flaming, only white smoke. Thermal runaway did not propagate beyond the initiating energy pod.	Sustained flames from the unit from 45 minutes to 221 minutes. Thermal runaway propagated to all energy pods.
Duration	75 minutes (from first smoke to extinguishment)	3 hours (from first flames to extinguishment)
CO	Max > 2,000 ppm (max measurement capacity of instrument). Remained elevated for 51 minutes.	Max = 50 ppm (only when external burners were on, not detected while undergoing self-sustaining combustion)
Cl_2	None detected	None detected
CH_4	Max = 96.9% (volume fraction)	None detected
HF	Max = 26 ppm. Remained at max for 2 minutes and then steadily decreased.	Max > 100 ppm (max measurement capacity of instrument). Remained elevated from 30 minutes. until end of test.

The HF concentration in the Internal Ignition test was significantly less than concentrations detected during the External Ignition Test. This was determined to be due to the lesser number of battery cells that became involved in combustion during the Internal Ignition Test. However, HF concentrations in both the Internal and External Ignition Tests were identified to be more than the PEL of 3 ppm (which is averaged over an 8-hour work shift).

3.1.7. Bordes et al., 2022

In this study, a series of tests was conducted on NMC pouch cells in various configurations to compare heat generation and gas and particle emissions during thermal runaway with flaming combustion versus during thermal runaway with no flaming combustion. The cells utilized in all tests were NMC pouch cells at 100% SOC with a nominal capacity of 70 Wh and a total mass of 485.3 g. The percent mass composition of a prototype cell was found to be 31% positive electrode materials and additives, 18% current collectors, 23% electrolyte, 4% separator, and 7% packing materials and connectors. All tests were conducted within a chamber with gas sampling extracted from the exhaust duct, with gas analysis performed through NDIR for CO and CO_2, a chemiluminescence-based on-line analyzer is for NO_x, FID for total hydrocarbons, and FTIR for additional gases such as organic carbonates (EC, DMC, ethyl methyl carbonate (EMC)), aldehydes, and fluorinated species (HF and POF_3). Air flow rates in the test chamber were approximately 1,000 m^3/h for the cell level test and 2,000 m^3/h for the array and module level tests. A polytetrafluoroethylene (PTFE) filter was placed within the test chamber for particle sampling of aluminum, cobalt, copper, lithium, phosphorus, nickel, and manganese with analyses by ICP-OES. A cellulosic filter was placed within the test chamber for particle sampling of fluorinated species with analyses according to the NF X 43-304 French standard.

HRR and total effective heat of combustion were determined through CO and CO_2 generation calorimetry. The authors note that, in battery fires, this method does not account for heat loss due to electrical or chemical processes, which might contribute up to 1/3 of the total thermal energy released in such an incident.

The first test was a cell-level test with thermal runaway initiated by an internal heater. Two insulated plates were placed on either side of the cell. During the test, the cell was observed to emit gases, without ignition, for the majority of the incident duration. A brief ignition of the vented gases occurred but did not result in a sustained flaming condition. Venting of gases during thermal runaway occurred for approximately 4 seconds. The maximum vent gas temperature recorded was 410˚C. The total gas released was 38 L (0.5 L/Wh). Table 12 presents the quantity of gases measured for the test.

Table 12. Gas quantities from cell level test of NMC pouch cell (Bordes et al., 2022)

Species	Total Gas Production		
	[g]	[L]	[mL/Wh]
CO_2	25.1	12.8	183
CO	5.4	4.3	61
HF	0.07	0.1	1
POF_3	1.4	0.3	4
H_2	0.1	1.3	19
Formaldehyde	0.3	0.2	3
Methane	0.7	1	14
Ethylene	0.7	0.5	7
DMC	40.3	10	143
EMC	15.5	3.3	47
EC	14.8	3.8	54
NO_x	ND	ND	ND
Total	104	37.7	539

ND: Not Detected

The third test was considered a module scale test and consisted of three, 3-cell arrays arranged in series. Each 3-cell array was separated by a polymer compression pad and an aluminum plate.

The ends of the cells were partially encased with acrylonitrile butadiene styrene (ABS) plastic. The total nominal capacity of the array was 627 Wh. Thermal runaway was initiated via an internal heater on the central cell. The initiating cell was observed to release significant gas, then calm down for 60 sec. The module then exhibited violent behavior, with strong flames, as the two adjacent cells simultaneously entered thermal runaway. Flaming combustion, due to the plastic components of the module, was observed up to 25 min after the first cell entered thermal runaway. During the test, thermal runaway only propagated through the initiating cell array. The other two cell arrays, on either side of the initiating array, moderately increased in temperature, but did not enter thermal runway. The authors attributed this to the polymer/aluminum barriers between the arrays. The total gas released was 466 L (0.8 L/Wh). The authors note that the quantity of gases is only from three of the nine cells in the module. Therefore, they provide a corrected normalized gas emission on 2.2 L/Wh. Table 13 presents the quantity of gases measured for the test.

Table 13. Gas quantities from module level test of NMC pouch cell (Bordes et al., 2022)

Species	Total Gas Production		
	[g]	[L]	[mL/Wh][1]
CO_2	808.5	411	1950
CO	14.2	11.4	54
HF	3.4	3.8	18
POF_3	1.12	0.2	0.9
H_2	-	-	-
Formaldehyde	0.5	0.4	2
Methane	1.5	2.2	10
Ethylene	1.2	0.9	4
DMC	96.2	23.9	113
EMC	40.0	8.6	41
EC	13.5	3.4	16
NO_x	0.5	0.4	2
Total	980	466	2210

[1]Accounting for only cells that entered thermal runaway (3)

Bordes et al. (2024) noted that CO_2, HF, and NO_x increased with the occurrence of flaming combustion, while methane, ethylene, CO, POF_3, carbonates, formaldehyde, and H_2 decreased. The authors contributed the increase in HF production during flaming combustion to the increase in temperature, which encourages thermal decomposition of fluorinated compounds, and/or the production of water which promotes HF formation from POF_3. This was also used to explain the decreased presence of POF_3 during flaming combustion with an increase during lower temperature and lower HRR conditions. The decrease of hydrocarbons during the flaming stages was contributed to these gases becoming involved in the combustion. Production of NO_x was noted only in the array and module level tests, and this was determined to be due to the presence of the ABS plastic encasing, which was not included in the cell level test.

The total heat released for the cell, array, and module tests were approximately 0.5, 8.0, and 10.5 MJ, respectively. For the array and module level tests, the heat released from the cells was estimated to be the same, however, the additional 2.5 MJ in the module test was produced during the slow combustion of plastic components of the module after completion of thermal runaway.

Bordes et al. (2022) determined an effective heat of combustion of 6 to 12 kJ/Wh for non-flaming combustion and 50 kJ/Wh for flaming combustion. This was explained by flaming combustion being a more effective thermochemical process, the involvement of additional combustible items (i.e. plastics, separators) during flaming conditions, and the increase of available oxygen. The peak HRR during the array test was found to be 130 kW, when the third cell entered thermal runaway. The peak HRR during the module test was found to be 250 kW, when the second and third cells entered thermal runaway simultaneously. In both tests, the HRR

during thermal runaway of the initiating cells, with no flames present, was found to be 20 to 25 kW.

3.1.8. Chen et al., 2017

Chen et al. (2017) performed testing on Li-ion batteries to assess the toxicity of the gases released during flaming thermal runaway. The test was conducted in accordance with the Chinese test standards GB/T 8323.2 and TB/T 3237-2010. The batteries were exposed to a 25 kW/m^2 radiant heater and ignited with a pilot flame inside a chamber. Gases released were measured via infrared analyzing instrumentation (CO and CO_2) and colorimetric gas detector tubes (SO_2, HCl, HBr, HF, HCN, NO_x). The specifications of the batteries were not identified. The results of the analysis are presented in Table 14.

Table 14. Toxic gases produced from burning Li-ion batteries (Chen et al., 2017)

Species	Concentration [ppm]
CO	28,400
CO_2	650
HF	0
HBr	0
HCl	0
NO_x	16
SO_2	10
HCN	1

Chen et al. (2017) determined that the gases were within a safe concentration range and "qualified." However, it is unknown what criteria were used to reach this conclusion. The gas concentrations were assessed for toxicity using the Chinese National Standard GB/T 20285-2006. Mice were exposed to the smoke and toxic gases produced. If the mice died within 30 minutes of exposure or had continued weight loss, the gas was considered dangerous. If the mice recovered

to their initial weight within three days and were still alive, the gases would be considered safe enough to have the highest allowable smoke concentration limit. The gases were ranked ZA2 and were "qualified." However, the authors do not explain what these classifications indicate. Absent battery specifications, it was not possible to correlate the gases produced with cell chemistry.

3.1.9. DNV, 2019

To assess Li-ion battery explosion risk and effectiveness of fire suppression methods, DNV GL conducted a series of tests on NMC and LFP cells to quantify gas production during thermal runaway events. Cell level tests were conducted with NMC pouch cells with a capacity of 63 Ah, LFP cylindrical 18650 cells with a capacity of 1.5 Ah, and LFP cylindrical 26650 cells with a capacity of 2.5 Ah, at varying SOC.

The tests were conducted inside a 0.44 m^3 chamber equipped with an exhaust fan set to flow air at a rate of 11 L/s. Gas samples were obtained from the interior of the chamber and FTIR was used for analysis of gases including CO, CO_2, NO, NO_2, HCl, HF, HCN, methane, ethane, ethylene, benzene, toluene, ethanol, and methanol.

Computational fluid dynamics (CFD) modeling was used to estimate the total amount of gas produced in the chamber, based on the FTIR concentration measurements. The CFD model did not account for leakage from the chamber. In addition, due to limitations of the measuring equipment, the results do not include hydrogen. However, using an assumed hydrogen concentration value of 30 %vol, based on a literature review, the authors adjusted the estimated total amount of gas produced; the authors did not adjust the toxic gas concentration estimates. Table 15 presents the adjusted total amount of gas produced for each test as well as the unadjusted percent volume concentration of toxic and asphyxiant gases.

Table 15. Gas volume and toxic gas concentrations from NMC and LFP cells (DNV, 2019)

Test ID	Cell Type	Capacity [Ah]	SOC [%]	Flaming?	Total Gas Production[1] [L]	%Volume						
						CO_2	CO	NO_2	HCl	HF	HCN	Benzene
A1	LFP	2.5	50	No	10	44.3	7.6	4.9	1.1	1.6	0.1	0.0
A2	LFP	2.5	75	No	7	20.2	15.9	9.7	0.8	1.6	0.1	0.7
A3	LFP	2.5	100	Yes	30	63.4	15.1	5.9	0.2	0.4	0.0	0.0
A4	LFP	2.5	100	No	21	20.9	26.1	1.3	0.3	0.1	0.1	13.6
B1	LFP	1.5	50	No	5	22.5	12.0	4.8	2.1	1.9	0.4	0.6
B2	LFP	1.5	75	No	5	23	13.9	5.6	1.9	3.7	0.7	0.0
B5	LFP	1.5	100	Yes	6	35.1	11.3	4.9	1.0	3.6	0.6	0.3
JDP 1	NMC	63	100	Yes	193	40.3	11.4	-	1.9	0.3	0.0	1.1
JDP 2	NMC	63	50	No	458	19.6	29.2	-	9.7	0.7	0.0	4.1
JDP 3	NMC	63	100	Yes	199	38.8	34.4	-	0.2	0.1	0.0	4.3
JDP 5	NMC	63	75	Yes	193	25.7	38.1	-	0.8	0.3	0.0	5.2
JDP 7	NMC	63	100	No	223	65.9	19	-	0.2	0.1	0.0	1.9

[1]Volume normalized to 25 °C ambient temperature and adjusted for a 30% H_2 concentration.

The authors noted that generally, tests in which there was no visible combustion produced a greater quantity of gas, due to an increase in CO and CO_2.

It was observed that the NMC cells produced their own oxygen during combustion of the electrodes, which encouraged flaming combustion, and likely contributed to increased yields of CO and CO_2. NMC cell tests also experienced higher temperatures and faster temperature increases. The duration of the intense vent gas release period at thermal runaway was found to be between 40 to 50 seconds for the NMC cells when flaming combustion was present, but this duration increased to 150 and 1050 seconds in cases where there was no flaming combustion.

For NMC cells, the thermal runaway onset temperature was found to be between 173 and 250°C for overheat failure scenarios and the maximum cell temperature was 481°C. For the overcharge and short circuit failure scenarios for NMC cells, the thermal runaway onset temperature was found to be 80 and 30°C, respectively, and the maximum cell temperature was

602°C. For the 1.5 Ah LFP cells, the thermal runaway onset temperature was found to be between 210 and 225°C for overheat failure scenarios and the maximum cell temperature was 384°C. The maximum cell temperature for the 2.5 Ah LFP cells was 243°C; the thermal runaway onset temperature could not be identified for these tests. For NMC cells, the temperature increase rate across all tests was between 13.6°C/s and 229°C/s, while for the LFP cells, the temperature increase rate across all tests was between 0.14°C/s and 5.06°C/s.

DNV GL also conducted a series of tests on NMC and LFP modules. Gas volume and gas concentrations were not reported for these tests. However, the authors observed that non-flaming scenarios produced more gas than flaming scenarios, consistent with what was observed in the cell level tests.

3.1.10. Ditch & Zeng, 2020

In a study conducted by Factory Mutual (FM), small, intermediate, and large-scale fire tests of Li-ion battery modules and module racks were performed. The tests were performed with two types of battery cell chemistries, LFP and LNO/LMO. The modules and racks for each battery type were set up in similar configurations. Modules were rectangular and made up of prismatic cells, arranged in a single row with thin metal cooling plates separating each cell. All modules were tested at a SOC of at least 95%. Racks were constructed with 8 levels of two modules side by side, for a total of 16 modules per rack, with the sides and backs of the rack enclosed with sheet steel. A thin removable separator, plastic for LFP tests and aluminum for LNO/LMO tests, was installed between the two columns of modules within the rack. The front of the rack was left open. The battery management system (BMS) for the rack was in place at the top of the rack but was not active during the tests; as such, protective mechanisms that would normally detect and shut down

the unit during thermal runaway were not operational. Some of the specifications for the battery cells, modules, and racks are indicated in Table 16.

Table 16. Li-ion battery equipment specifications for tests performed by Ditch and Zeng (2020)

	Number of Cells	Energy [kWh]	Mass [kg]	Combustible Load [kg]
LFP Cell	1	0.07	-	-
LFP Module	78	5.2	49	7.5
LFP Rack	1,248	83.6	-	120
LNO/LMO Cell	1	0.12	-	-
LNO/LMO Module	64	7.8	75	13.6
LNO/LMO Rack	1,024	125	-	218

The total combustible load of the modules and racks were estimated based on total weights and estimated mass percentages of the combustible components, classified into either electrolyte or unexpanded plastics. Electrolyte mass was estimated to be 7% of the individual battery mass, based on the author's experience in studies of batteries with similar capacity, and approximately 15 to 20% of the total module mass was classified as combustible. The material and mass of the separators within the battery cells were unknown and therefore not included in the calculations for combustible loads. The remainder of the module components were mostly metal and considered negligible. For the electrolyte heat of combustion, a value of 28 MJ/kg, based on DEC, was used and for the plastic components a value of 38 MJ/kg was used. A ±10% uncertainty was added for the calculated energies. The calculated total combustible load was approximately 279 MJ for the LFP module and 4,464 MJ for the rack. The calculated total combustible load was approximately 509 MJ for the LNO/LMO module and 8,142 MJ for the rack.

Tests were performed under a hood to measure the HRR of the various fire tests through three different techniques. The convective HRR was calculated from the measured gas temperature and mass flow through the FPC. An uncertainty of ±10% was applied to these results. The chemical

HRR was calculated from the measurement of CO and CO_2 within the hood duct. An uncertainty of ±20% was applied to these results to account for typical sources of uncertainty for ordinary combustibles as well as carbonate species produced during thermal runaway. Ditch and Zeng (2020) identified that previous studies have suggested that HRR rate calculations based on oxygen consumption can be corrected to account for the thermal runaway gases produced by Li-ion batteries; however, they determined that these corrections could not be accurately applied in their tests due to variability based on battery chemistry, quantities of batteries, quantity of other combustibles, and stages of fire development. Chemical HRR based on oxygen consumption calorimetry was also calculated for the tests but was found to be unreliable due to drifting of the O_2 analyzer; as such, these results were not reported.

In the small-scale tests, a single battery module was forced into thermal runaway via heating elements attached to the underside of the module. The heating source remained active until sustained burning was achieved within the module. In the LFP tests, it was observed that while significant vent gases were released during heating, ignition of these gases did not always occur, and had to be initiated via an external pilot flame in some cases. When self-ignition did occur, the time to ignition varied from 45 seconds to 7 minutes after venting. Meanwhile, in the LNO/LMO cell tests, sparks and flames were observed that consistently ignited the cell vent gases.

The LNO/LMO module was observed to produce a much higher peak chemical HRR (1,023 kW) and chemical total heat released (THR) (315 MJ) compared to the LFP module (413 kW and 143 MJ, respectively). The corresponding convective HRR and THR values were 450 kW and 204 MJ for the LNO/LMO module and 214 kW and 101 MJ for the LFP module. These values were approximately 50-60% of the estimated combustible load energies discussed previously.

In the intermediate-scale tests, three levels of two battery modules side by side were installed within a metal cabinet, for a total of 6 modules. Based upon the description, it is assumed that there was no metal dividers or separations between the stacks. The bottom left module was forced into thermal runaway via heating elements attached to the underside of the module. A pilot flame, intended to ensure ignition of cell vent gases, was placed at the bottom of the rack 76 mm from the face of the initiating module. A pilot flame was not used for the single module testing.

For the LFP modules, it was observed that from the initiating module, the fire spread vertically up the left stack. After the top left module ignited, fire spread horizontally to the top right module (approximately 40 minutes after first sustained flames observed at initiating module), and then spread downwards to the two remaining modules in the right stack. The fire reached the peak HRR approximately 84 minutes after the first sustained flames were observed at the initiating module. In total, the fire burned for over 150 minutes before it was manually extinguished prior to all fuel being fully consumed. For the LNO/LMO modules, from the initiating module the fire spread horizontally to the bottom right module. Then, the fire spread vertically and simultaneously up both modules. The LNO/LMO peak HRR was reached at approximately 32 minutes after sustained flames were observed at the initiating module. All LNO/LMO modules were observed to be burned out at 74 minutes after sustained flames were observed at the initiating module; however, an orange glow continued until the test was terminated 72 minutes later.

The LNO/LMO modules were observed to produce a much higher peak chemical HRR (1,890 kW) and chemical THR (2,034 MJ) compared to the LFP modules (500 kW and 1,152 MJ, respectively). The corresponding convective HRR and THR values were 1,020 kW and 1,435 MJ for the LNO/LMO module and 312 kW and 758 MJ for the LFP module. These values were

approximately 66% of the estimated combustible load energies discussed previously. It was estimated that an additional 5% of total heat released could be added to the LFP module test given that the fire was extinguished before full mass consumption.

The large-scale tests were run in the same manner as the intermediate-scale tests, except that a full BESS rack was used. The rack was provided by an unidentified manufacturer and populated with eight levels of two modules side by side for a total of 16 modules. Imitation rack extensions were installed on either side of the rack but were not populated with additional battery modules. For both the LFP and LNO/LMO racks, from the bottom left initiating module, the fire was observed to spread vertically up the center of the rack igniting modules on both sides. For the LFP rack, the peak HRR was reached at approximately 34 minutes after sustained flames were observed at the initiating module. The fire burned for approximately 98 minutes before self-extinguishing. For the LNO/LMO rack, the peak HRR was reached at approximately 29 minutes after the sustained flames were observed at the initiating module. The fire burned for over 160 minutes before it was manually extinguished, prior to all fuel being fully consumed.

The LNO/LMO rack produced a much higher peak chemical HRR (10,660 kW) and chemical THR (6,390 MJ) compared to the LFP rack (2,540 kW and 3,810 MJ, respectively). The corresponding convective HRR and THR values were 6,840 kW and 4,660 MJ for the LNO/LMO module and 1,680 kW and 2,770 MJ for the LFP module. These values were approximately 78 to 85% of the estimated combustible load energies discussed previously.

The results from all three levels of tests were analyzed to identify relationships between electrical capacity of the battery installation, combustible load, total energy released, and peak HRRs. It was found that total energy released had a linear relationship with both electrical capacity

and combustible load, and trends were consistent across the LFP and LNO/LMO batteries. However, it was found that the peak HRR had a non-linear relationship with both electrical capacity and combustible load, and trends were different across the LFP and LNO/LMO batteries. This non-linear trend was partially attributed to the occurrence of more extensive heating in the rack and multi-module systems which lead to more rapid involvement of subsequent modules. Ditch and Zeng (2020) noted that the trends identified in their testing should not be universally applied to other batteries, modules, or systems. The reason was because different battery modules, even those that are LFP or LNO/LMO, may have different ratios of electrical capacity to combustible load and/or different energy capacities per unit of volume.

3.1.11. Essl et al., 2020a

In this study, a series of tests on NMC/LMO cells was conducted to investigate hazards related to thermal behavior, vent gas production, and vent gas composition. The cells utilized were 41 Ah/156 Wh, NMC/LMO pouch cells at 100, 30, and 0% SOC. The cell mass was 865 g. The experiments were conducted inside a pressure chamber, purged with nitrogen. Thermal runaway was initiated by heater stripes attached to the metal sample holder plates on either side of the cell. Thermocouples were placed in four locations within the chamber to measure gas temperatures. Vent gas production was determined through pressure sensors in the chamber and the ideal gas law. Total gas production was determined for the total duration, between the initial vent and the initiation of thermal runaway, during thermal runaway, as well as the venting rate when 50% of the vent gas is released. The composition of the vent gases was determined via FTIR and gas chromatography. Gases analyzed were H_2, CO, CO_2, methane, ethane, ethylene, acetylene, DEC, DMC, EC, EMC, H_2O, hexane, HF, butane, and propane.

The thermal runaway onset temperature was determined to be 170°C for the 100% SOC cell. The experiments involving the 30% and 0% SOC cells did not achieve thermal runaway. Table 17 and Table 18 present the results of the vent gas measurements and analyses.

Table 17. Vent gas production from 41 Ah NMC/LMO cells (Essl et al., 2020a)

	100% SOC	30% SOC	0% SOC
TR Vent Duration [s]	4	N/A	N/A
Characteristic Vent Rate [L/s]	18.7	N/A	N/A
Total Vent Gas [L]	57	13	10
Normalized Total Vent Gas [L/Ah]	1.4	0.32	0.24
Mass Loss [%]	43	15	15
Uncondensed Gas Mass [g]	74	27	-
Particle Release [g]	300	N/A	N/A

N/A: Not applicable

Table 18. Vent gas composition from 41 Ah NMC/LMO cells (Essl et al., 2020a)

Species	% Volume	
	100% SOC	30% SOC
H_2	23	4
CO	17	5
CO_2	38	48
Methane (CH_4)	3	<1
Ethane (C_2H_6)	<1	<1
Ethylene (C_2H_4)	6	3
Acetylene (C_2H_2)	<1	<1
DEC	3	21
DMC	ND	ND
EC	ND	ND
EMC	ND	ND
H_2O	8	18
Hexane (C_6H_{14})	ND	ND
HF	ND	ND
Butane ($C4H_{10}$)	1	ND
Propane (C_3H_8)	ND	<1

Volume percent values were not reported for the 0% SOC test.

The authors observed that the vent gas composition reported in the 30% and 0% SOC tests was similar to that found prior to thermal runaway in the 100% SOC test. HF was not detected in any of the tests.

3.1.12. Essl et al., 2020b

Essl et al. (2020b) performed a series of tests on NMC cells to understand how different thermal runaway triggers influenced thermal behavior, vent gas production, and vent gas composition. Two types of cells were utilized, a 60 Ah/216 Wh, NMC prismatic cell at 100% SOC and a 60 Ah, NMC pouch cell at 100% SOC. The prismatic cells had a EC:DMC:EMC electrolyte and the pouch cells had a EC:EMC electrolyte.

The experiments were conducted inside a pressure chamber, purged with nitrogen. Thermal runaway was initiated by overtemperature, overcharge, and nail penetration. Thermocouples were placed in the pouch cell's foil welded sides and at the prismatic cell burst plates to measure the vent gas temperatures. Vent gas production was determined through the use of pressure sensors in the chamber and the ideal gas law. Quantities of gas were determined for the total duration, between the initial vent and the initiation of thermal runaway, during thermal runaway, as well as the venting rate when 50% of the vent gas is released. The composition of the vent gases, only after thermal runaway, was determined via FTIR and gas chromatography. Gases analyzed were H_2, CO, CO_2, methane, ethane, ethylene, acetylene, DEC, DMC, EC, EMC, H_2O, hexane, HF, butane, and propane.

The average maximum vent gas temperatures for the pouch cells were 584°C, 1044°C, and 482°C, for the overtemperature, overcharge, and nail penetration failure scenarios, respectively. The average maximum vent gas temperatures for the prismatic cells were 1169°C, 1021°C, and 850°C, for the overtemperature, overcharge, and nail penetration failure scenarios, respectively. The authors noted that the increase in the vent gas temperatures seen for the prismatic cells was due to a more concentrated point release from the cell, as opposed to the pouch cells where the gas

can release simultaneously from all sides. The authors also noted that the vent gas temperature might be influenced by the ejection of hot particles. Table 19 and Table 20 present the results of the vent gas measurements and analyses.

Table 19. Vent gas production from 60 Ah NMC cells across various thermal runaway triggers (Essl et al., 2020b)

	Overtemperature		Overcharge		Nail Penetration	
	Pouch	Prismatic	Pouch	Prismatic	Pouch	Prismatic
TR Vent Duration [s]	3.5	2	5.2	1.1	3.1	11.5
Characteristic Vent Rate [L/s]	34	67	47	250	182	140
Total Vent Gas [mol]	3.8	3.8	6.9	6.5	4.2	4.3
Normalized Total Vent Gas [L/Ah]	1.56	1.56	2.79	2.65	1.71	1.77
Mass Loss [%]	56	47	81	67	47	33

Table 20. Vent gas percent volume composition from 60 Ah NMC cells across various thermal runaway triggers (Essl et al., 2020b)

Species	Overtemperature		Overcharge		Nail Penetration	
	Pouch	Prismatic	Pouch	Prismatic	Pouch	Prismatic
H_2 [%]	15	15	26	27	23	20
CO [%]	26	30	33	30	22	23
CO_2 [%]	30	21	20	20	30	24
Methane (CH_4) [%]	5	5	5	7	3	5
Ethane (C_2H_6) [%]	<1	<1	1	<1	1	<1
Ethylene (C_2H_4) [%]	10	5	8	4	14	7
Acetylene (C_2H_2) [%]	<1	<1	ND	<1	ND	<1
DEC [%]	ND	ND	ND	ND	ND	ND
DMC [%]	ND	2	ND	<1	ND	2
EC [%]	ND	ND	ND	ND	ND	ND
EMC [%]	3	<1	ND	ND	ND	ND
H_2O [%]	4	4	3	3	3	3
Hexane (C_6H_{14}) [%]	ND	<1	ND	<1	ND	<1
HF [%]	ND	ND	ND	ND	ND	ND
Butane ($C4H_{10}$) [%]	<1	2	0	<1	<1	1
Propane (C_3H_8) [%]	ND	ND	ND	ND	ND	ND

The authors noted that while HF was not detected in any of these tests, they assume that it was produced in small amounts but due to the high reactivity of the compound, it did not transport into the FTIR spectrometer. It was also noted that the same experimental setup was used for older 18

Ah NMC/LTO cells and a concentration of 66 ppm of HF was detected after thermal runaway. The authors identified that the detection of EC was highly unlikely with the experimental setup. The overcharge experiments were observed to generate significantly more gas, have a higher mass loss, and have a higher concentration of H_2 and CO. The authors suggested this is due to the additional energy that is imparted into the cells by the overcharge.

3.1.13. Forestier et al., 2020

In an evaluation of the influence of Li-ion battery cell confinement, electrolyte composition, and separator composition on thermal and toxicological hazards, Forestier et al. (2020) performed a series of tests on 0.6 Ah NMC pouch cells. The total mass of the cell was approximately 13.5 g and consisted of approximately 31% negative electrode, 20% current collectors, 18% electrolyte, 4% separator, and 9% packaging materials and connectors.

Tests of single cells were conducted within a chamber filled with ambient air. Thermal runaway was initiated via heating wire with a continuous ramp. Gas sampling and analysis was performed via a heated sampling line from the top of the chamber connected to a FTIR spectrometer.

Thermal runaway onset temperatures were determined to be 180 to 200°C when the cells were not confined with pressure, and 245°C when pressure was applied. The authors explained that the increase in onset temperature in the confined case is due to the restriction of cell swelling which prevents electrolyte from coming into contact with the electrodes.

Table 21 and Table 22 present the results of the gas analysis for certain groups of tests. The publication did not report specific values for each test conducted.

Table 21. Average vent gas quantities from 0.6 Ah NMC cells (Forestier et al., 2020)

Species	Vent Gas Production [mg]			
	No VC [mg]	VC [mg]	VC and Ceramic Coating of Separator [mg]	VC, No Ceramic Coating of Separator [mg]
CO	200	240	-	-
CO_2	800	1000	-	-
DMC	900	950	-	-
EC	640	500	-	-
EMC	810	950	-	-
HF	15	16	11	20
POF_3	6	7	12	26
Formaldehyde	40	23	14	22

Table 22. Max vent gas concentrations from 0.6 Ah NMC cells (Forestier et al., 2020)

Species	Vent Gas Concentrations [ppm]	
	Unconfined	Confined
CO	5500	350
CO_2	16500	2400
HF	500	56
POF_3	1600	82
SO_2	275	-
HCN	50	-
Formaldehyde	675	90

The authors noted that the confined cell tests (pressure applied to sides of cell) produced less gas overall, including both hydrocarbons and toxics. This was also contributed to the cell not being allowed to swell, thus preventing additional electrolyte from coming into contact with the electrodes.

3.1.14. Franqueville et al., 2023

Franqueville et al. (2023) assessed the minimum safety distances related to firefighting and evacuation for Li-ion battery fires. A meta-analysis of the literature was conducted to establish the main toxic gas species emitted by Li-ion batteries. CFD modeling was performed using Fire Dynamic Simulator (FDS) to characterize toxic gas profiles associated with various ambient conditions, e.g., temperature, wind, etc., and battery characteristics. Estimated minimum safety

distances were determined through comparison of predicted toxic gas concentrations and IDLH values.

The production of toxic gases was modeled as a boundary condition with mass flow rate for the lumped toxic gas species. The mass flow rate was calculated by multiplying the sum of estimated yields for each species by an estimated total mass production rate. For lumped species, the fraction of each toxic gas was specified using mass fractions that were proportional to the yields. The yield of each toxic species was obtained by dividing its reported mass production per unit of battery energy by the estimated total mass produced per unit of battery energy. The mean mass of gas produced per unit of battery energy was 0.47 g/Wh. An estimated heat of combustion was derived using experiments where the total heat released, and mass loss was reported. The heat of combustion was found to be 17 MJ/kg. The mean mass loss per unit battery energy was 2.3 g/Wh. To calculate the distribution of HF yields, the HF data reported in terms of mass per unit of battery energy were divided by the approximate total mass released per unit of battery energy.

A model representing a home garage, or the container of a BESS unit, was run for both flaming and non-flaming thermal runaway. The room was 6 m by 5 m by 2.5 m with a 1 m by 2 m open door. A 4 m by 1 m by 1 m object representing a battery was placed inside the room. There were two vents on the battery, one for toxic gases and the other for flammable gases. The domain size was 36 m by 104 m by 8 m and the sides and top were set to open. The grid inside the room was 25 cm, and was increased to 50 cm, 1 m, and 2 m outside the room.

Refining the mesh did not significantly change the plume characteristics. The concentration field of each toxic gas was extracted at 2 m to represent head height. The maximum battery system size was set to energy of 3 MWh at 100% SOC. The mean HF value used was 0.008 kg/kg for non-

flaming; HF was only gas coming out of the toxic vent. Mean volume percentages of all other species including CO, CO_2, and H_2, were assigned to the flammable gases vent. The gas release temperature was 300ºC.

For flaming, the gas released normalized by capacity in Wh was determined by applying a multiplier five to the non-flaming case. The FDS "simple" combustion model was used. The gases released from the toxic vent were HF, CO, HCl, NO, and SO_2. The release of these toxic gases was defined by a lumped toxic gas species and composition was specified using mass fractions. The MLR of the lumped toxic gas species was specified by multiplying the total mass flow rate by the sum of the yields of all toxic gases. The soot yield was set at 0.05 kg/kg. The MLR profiles are triangular and ranged from 1 kg/s (non-flaming) to 4 kg/s (flaming) at peak. The steady state equivalent MLR was approximately 1 kg/s for the flaming and non-flaming cases.

The flaming simulation used a summed toxic gas yield rather than an individual yield. Scenario-based simulations included 50 and 100% SOCs, wind speeds of 3, 8, 24, and 32 km/h, and six battery energies ranging from 5 kWh to 3 MWh. Zero mph wind cases were not considered because it showed that the plume went straight up, so safety distances were very small, e.g., the smaller the safety distance, the closer the firefighter can be to the source without a negative health impact. Failure duration was one hour.

A battery electric vehicle (BEV) was modeled using yields from the vehicle that produced the most toxic concentrations. The computational domain and room sizes remained the same as the BESS unit model.

For the non-flaming case, the worst-case timestep regarding toxicity was at the peak mass flow rate. However, the worst-case timestep in the flaming case did not align with the peak mass flow

rate. The authors determined this was due to a balance between two factors; as the HRR increased, plume buoyancy increased and reduced the safety distance while at the same time, the mass flow rate of the toxic gases increased, causing an increase in safety distance. The authors identified that when the mass flow rate is less than 1 kg/s, the effect of toxic gas mass flow dominates, and the safety distance increases with the mass flow rate. The study found that plumes in the 100% SOC scenarios had a greater buoyancy than in the 50% scenario, which would decrease safety distances. However, the increased toxic gas production outweighed this effect, resulting in an overall increase in safety distances for 100% SOC scenarios versus 50% SOC scenarios.

For all flaming simulations, HF was the gas setting the safety distance. HF was the gas that required the largest distance to drop below IDLH. The largest safety distances across all SOCs and battery sizes for the 2, 5, 15, and 20 mph wind speeds were 5, 13, 45, and 54 m, respectively. The authors contributed the correlation of increasing safety distance with increasing wind speeds to the plume being able to rise upwards at the low wind speeds.

For the non-flaming scenarios, most safety distances were also set by HF. The largest safety distances across all SOCs and battery sizes increased from 13 m to 51 m at 2 mph and 5 mph, respectively but then decreased to 34 m and 22 m at 15 and 20 mph, respectively. The authors contributed the decrease in safety distance at high wind speeds to increased dilution of the plume. In all cases, the non-flaming scenarios had higher or approximately equal mean safety distances compared to the flaming scenarios.

3.1.15. Golubkov et al., 2014

Golubkov et al. (2014) conducted thermal runaway experiments on three types of Li-ion cell chemistries to evaluate the influence of cell chemistry on the thermal and explosive hazards. The

cells utilized were LCO/NMC cells with a 2.6 Ah/9.9 Wh capacity and a mass of 44.3 g, NMC cells with a 1.5 Ah/5.7 Wh capacity and mass of 43.0 g, and LFP cells with a 1.1 Ah/3.5 Wh capacity and a mass of 38.8 g. All cells were cylindrical 18650 type cells at 100% SOC.

The experiments were conducted inside a sealed reactor, purged with argon. Thermal runaway of the cells was initiated by a heating sleeve with a consistent temperature ramp. Gas temperatures and pressure inside the reactor were measured and inputted into the ideal gas law to determine the quantities of gas produced. Gas samples from the chamber were started after thermal runaway or, if no thermal runaway occurred, after the cell temperature exceeded 250°C. Gas samples were analyzed for H_2, O_2, N_2, and hydrocarbons using gas chromatography. Table 23 presents the thermal runaway onset temperature, vent duration, quantity of vent gas produced, and the CO_2 and CO mole percentages of the vent gas for each for each cell chemistry.

Table 23. Test results from 2.6 Ah LCO/NMC, 1.5 Ah NMC, and 1.1 Ah LFP cells (Golubkov et al., 2014)

Cell Type	TR Onset Temp. [°C]	Total Gas Production [mmol]	Peak Venting Duration [s]	Concentration [%mol]	
				CO_2	CO
LCO/NMC	149	265	0.8	24.9	27.6
NMC	168	149	0.2	41.2	13.0
LFP	195	50	30	53.0	4.8

3.1.16. Golubkov et al., 2015

In this study, Golubkov et al. (2015) performed testing of LFP and NCA Li-ion cells to assess the impact of SOC and overcharge. The cells utilized in the testing were all 18650 cylindrical cells. The LFP cells had a mass of 38.87 g and a nominal capacity of 1.1 Ah. The NCA cells had a mass of 45.4 g and a nominal capacity of 3.35 Ah. The LFP cells were charged to 3.5V and the NCA were charged to 4.2V.

The experiments were conducted inside a sealed reactor, purged with inert gas (nitrogen or argon). Thermal runaway of the cells was initiated by a heating sleeve with a consistent temperature ramp. Gas temperatures and pressure inside the reactor were measured and inputted into the ideal gas law to determine the quantities of gas produced. Gas samples from the chamber were started after thermal runaway or, if no thermal runaway occurred, after the cell temperature exceeded 250°C. Gas samples were analyzed for H_2, O_2, N_2, and hydrocarbons using gas chromatography.

NCA and LFP Cells with a 0% SOC did not enter thermal runaway and displayed vent gas releases with a uniform rate; there were no sudden or violent reactions or gas releases. NCA cells with a SOC of 25% or greater did enter thermal runaway. LFP cells with a SOC of 25% did not achieve distinctive thermal runaway and behaved similar to the 0% SOC. LFP cells with a SOC of 50% or greater did enter thermal runaway. Thermal runaway onset temperatures for LFP and NCA cells with a SOC of 100% or less were between 136 and 160°C. Thermal runaway onset temperatures for NCA cells with a SOC of greater than 100% were between 65 and 80°C, while for overcharged LFP cells they were still approximately 140°C. Table 24 presents the mass loss, quantity of vent gas produced, and the CO_2 and CO mole percentages of the vent gas.

Table 24. Test results from 3.35 Ah NCA and 1.1 Ah LFP cells (Golubkov et al., 2015)

Test ID	Cell Type	SOC [%]	Mass Loss [g]	Total Gas Production [mmol]	Concentration [%mol]	
					CO_2	CO
1	NCA	0	-	65	94.6	1.6
2	NCA	0	4.4	52	94.7	1.9
3	NCA	0	4.5	55	96	1.5
4	NCA	0	4.5	39	96.2	1.1
5	NCA	0	4.5	59	96.6	1
6	NCA	25	5.9	67	62.7	5.5
7	NCA	50	8.5	157	33.8	39.9
8	NCA	75	-	217	20.8	43.7
9	NCA	100	-	273	19.7	48.9

10	NCA	100	20.5	314	17.5	44
11	NCA	100	20.9	244	22.7	41.5
12	NCA	112	19.2	252	18.8	48.1
13	NCA	120	-	281	20.8	48.7
14	NCA	127	-	317	16.2	46.6
15	NCA	132	17	262	18.9	49.2
16	NCA	143	20.1	303	22	43.4
17	LFP	0	6.1	55	93.5	1.8
18	LFP	25	6.1	31	85.3	3.1
19	LFP	50	6.1	32	66.2	4.8
20	LFP	75	6.3	41	62.6	6.4
21	LFP	100	7.2	32	48.3	9.1
22	LFP	115	6.2	61	52.2	6.4
23	LFP	130	-	58	55.8	7.7

The authors noted that for NCA cells, the quantity of gas increased with increasing SOC; however, for LFP cells, there was not a clear correlation. For NCA cells, as the SOC increased, the concentration of CO tended to increase while the concentration of CO_2 decreased. For LFP cells, as the SOC increased, the concentration of CO_2 decreased. CO concentrations were observed to be lower for LFP cells (maximum 9.1 %) versus NCA cells (maximum 49.2%).

3.1.17. Hill, 2020

On April 19, 2019, a thermal runaway event occurred in a McMicken BESS in Surprise, Arizona. The report by Hill (2020) discusses the findings of the incident investigation and subsequent analysis and provides background on typical Li-ion battery characteristics. The unit involved in the incident was a 2 MW/MWh battery composed of 10,584 NMC pouch battery cells manufactured by LG Chem. The pouch cells were Model JP3 and were 64 Ah/0.24 kWh cells with an operational voltage of 3.0 to 4.2V. The cells were arranged into 6.7 kWh modules with 28 cells per module. The modules were arranged into racks with 14 modules per rack. A total of 27 racks made up the BESS unit. The BESS was equipped with a clean agent fire suppression system. The incident was initiated when a single cell went into thermal runaway. The thermal runaway of the

cell caused adjacent cells to go into thermal runaway, and eventually, spread to adjacent modules within the rack. Thermal runaway event, however, did not propagate to adjacent racks in the enclosure. Three hours into the event, firefighters opened a door to the unit and an explosion ensued; the explosion resulted from a buildup of combustible gases inside the unit during the thermal runaway and the introduction of oxygen into the enclosure through the open door.

An analysis of the incident was conducted to assess on-site and off-site environmental and health impacts. This analysis included collecting soil samples, surface samples, and performing air dispersion modeling to identify exposures to contaminants of concern. Soil samples were collected from the ground surface around the incident BESS, and wipe samples were collected from the interior of the BESS. These samples were analyzed for a variety of organic and inorganic compounds suspected to be present based on the chemical safety data sheets and information provided by the vendor. It was found that generally, within all samples, the concentrations of contaminants of concern were undetectable or like control samples. There were no samples that had concentrations greater than thresholds set by applicable state and federal standards for site remediation or response actions (Hill, 2020). Air dispersion modeling was conducted to assess the transport of particulate matter (PM) and contaminants of concern. The analysis "relied upon conservative emission rates", however, further details, including these emission rates were not provided in the report (Hill, 2020). The air dispersion modeling analysis concluded that PM dispersion was minimal and limited to the immediate area around the BESS and that concentrations of contaminants off-site were at levels below state and federal standards. The air dispersion modeling program employed was not stated.

3.1.18. Huang et al., 2016

The authors initiated thermal runaway in modules composed of NMC/LTO cells with a 50 Ah capacity at 100% SOC to characterize the thermal behavior of battery modules undergoing thermal runaway. Cells were equipped with tabs and relief valves set to vent at 0.5 MPa. Two different formations were tested- a rhombus and a parallel line. Both module types laid horizontally on a platform 85 mm above a 5-kW heater. A hood collected the combustion products. The authors measured HRR through oxygen consumption calorimetry, temperature at the cell surface and tabs, ambient temperature, and mass loss percentage to determine if the arrangement of the cells affected thermal runaway in the module.

For the rhombus module, a jet flame emerged from Cell 2 between 0 to 1601 seconds. At 2210 seconds, thermal runaway was triggered at the same cell, which caused a stronger jet flame and ignited Cell 4. However, the ignition of Cell 4 had no significant impact on the HRR. Cell 4 extinguished at the same time Cell 3 ignited and entered thermal runaway (2655 seconds). Jets of white and black smoke appeared from Cell 3. Then, the module entered a stable combustion phase lasting 120 seconds. Afterwards, there was no visible flaming/smoke ejection (2760 to 4011 seconds), but decomposition in all cells continued to produce combustible gases. At 4011 seconds, Cell 4 exploded, destroying the experimental set up. Two minutes later, Cell 1 exploded.

The evolution of the event in the parallel line module test was similar to what was seen in the rhombus module. Cell 6 was the first to ignite and enter thermal runaway (0 to 1740 seconds). Afterwards, the module entered the stable combustion phase, which lasted for 540 seconds. Cell 7 ignited between 2400 to 2730 seconds, which then triggered thermal runaway and flaming in Cell 5. The flame from Cell 5 was blown off by the smoke flow. The flame from Cell 7 ignited the blown off smoke and caused a jet fire. At 2721 seconds, the jet fire caused a violent ejection of

black smoke from Cell 7. After 2730 seconds, flaming and smoking self-extinguished slowly. Table 25 shows the surface and tab ignition or explosion temperature, time to ignition, maximum temperature, thermal runaway propagation time, peak HRR, and total mass loss ratio of each cell.

Table 25. Comparison of parameters associated with thermal runaway and combustion characteristics (Huang et al., 2016)

Cell No.	1	2	3	4	5	6	7	Reference
T_{sur} [ºC]	See Note a.	135/-	185/-	78.5/192	124.1/-	128/-	139.1/-	146.6/-
T_{tab} [ºC]	See Note a.	116/-	178/-	73.7/149	181.1/-	135/-	147.6/-	121/-
Time to ignition [s]	-	1593	2626	2206	2299.9	1740	2326	1465
T_{max} [ºC]	173	466	425	192	384.4	-	443.1	494
Time to TR [s]	-	0	1033	613	548.9	0	586	-
Peak HRR [kW]	-	14/13/22.3	7.85	65	-	-	-	38
Mass loss ratio [%]	Exploded	20.9	30.79	Exploded	26.1	41.6	29	28.9

a. As no ignition occurred for LIB No. 1, T_{ign} for the surface and tabs were not detected. The explosion of LIB No. 4 destroyed all the thermocouples, so T_{exp} was not detected.
T_{sur}: ignition/explosion temperature at the surface
T_{tab}: ignition/explosion temperature at the negative tab
$T_{ign,tab}$: ignition temperature at the negative tab

The surface ignition temperatures ranged from 110 to 140ºC, but thermal runaway temperatures varied significantly. Huang et al. (2016) noted that it is possible that the heating effect from impinging fire accelerated thermal runaway onset. The largest mass loss percentages are correlated with peaks in HRR, ignition, and onset of thermal runaway.

3.1.19. Huang et al., 2020

Huang et al. (2020) explored the impact of electrical connection on thermal runaway propagation and characterized thermal runaway features of large format, Li-ion battery modules. The authors tested prismatic, 94 Ah, NMC single cells and 4-cell modules under a cone calorimeter. The single cells were tested by utilizing a 500 W heating plate placed on the sidewall of the cell to trigger thermal runaway. Cells were tested at 100% and 50% SOC. Gases were

quantified via FTIR. The modules were formed by placing four batteries in a steel holder and connecting them in series, parallel, or not at all. The heating plate placed on the sidewall of one battery. Once thermal runaway was confirmed, the heating plate was removed.

The 100% single cell underwent five stages during flaming thermal runaway. In the lateral heating stage, the battery starts self-heating as the chemical components decompose and react. In the next stage, the safety valve on the cell breaks and vents jet fire and black smoke violently. Then, the jet fire and smoke decrease in the third stage. The combustible gases and ejected electrolyte are ignited, burn, and combustion slows down as the fuel is consumed in stage four. The final stage is the end of the test.

The 50% SOC cell also had five stages of combustion. The first stage was also lateral heating; however, the other stages were different from the 100% SOC cell combustion. The cell underwent safety venting in stage two and vented jet white smoke in stage three. In stage four, the jet white smoke abated, and stage five was the end of the test. For the 50% single cell test, cell venting during thermal runaway occurred for approximately 82 seconds. Table 26 provides the combustion characteristics of the single cell tests.

Table 26. Gas volume and gas concentrations from a 94 Ah prismatic NMC cell (Huang et al., 2020)

SOC [%]	Flaming?	Mass Loss [%]	Peak HRR [kW]	Total Gas Production [g]				Peak Concentration [ppm]			
				CO_2	CO	NH_3	SO_2	CO_2	CO	NH_3	SO_2
100	Yes	31.8	15.0	115.5	45.1	0.31	5.15	6300	6000	63	123
50	No	22	-	50.57	6.45	0.56	10.43	760	258	36	108

The module level tests had three distinct stages during thermal runaway. First, the cells are heated, which causes an increase in gas production and internal pressure. This leads to cell safety venting. In the second stage, thermal runaway has propagated to all four cells in the module and

violent jet fire and black smoke are released. In stage three, the cells enter a weaker combustion stage and slowly abates as fuel is consumed. Testing revealed that thermal runaway propagates due to the heat transfer between adjacent modules. The authors noted that heat transfer through the connectors and radiation primarily drives heat transfer, while conduction through air contributes less.

3.1.20. Huang et al., 2021

The authors tested large format Li-ion modules with NMC and LFP cell chemistries at 100% SOC to compare their performance. Each module held four prismatic cells physically in parallel without electrical connection. The LFP cells each had a capacity of 336 Wh and weighed 2097 g. The NMC cells each had a capacity of 360 Wh and weighed 2027 g. One cell at the end of the module was heated to thermal runaway by a 0.5 kW heating plate.

Thermal runaway was defined as reaching 368°C at the front surface and 93°C at the back surface for NMC cells. For LFP cells, it was defined as reaching 335°C at the front surface and 121°C at the back surface. After reaching thermal runaway, the heating plate was turned off. Thermal runaway tests were conducted underneath a hood open to ambient air. The gases produced from the modules were analyzed for CO, CO_2, CH_4, C_2H_4, C_3H_6, H_2, HF, NH_3, and HCl using FTIR, a H_2 detector, and a HF detector. MLR and HRR were calculated using oxygen consumption, and pressure differential and smoke temperature, respectively.

The NMC modules underwent safety venting, jet fires, black smoke, and explosive into stable combustion when thermal runaway was triggered. Thermal runaway propagated through all cells in the NMC module in both NMC experiments. The NMC cells reached higher temperatures and had higher thermal runaway propagation speeds than the LFP cells. The period between safety

venting and thermal runaway was shorter for NMC cells (0 to 23 seconds) compared to LFP cells (98 to 597 seconds), indicating that the safety venting did not prevent thermal runaway in the NMC modules. On the other hand, the LFP modules released white smoke when entering thermal runaway but did not achieve flaming combustion. Complete thermal runaway occurred in only one of three LFP experiments. However, the duration of thermal runaway for LFP cells (208 to 247 seconds) was longer than the duration for NMC cells (19 to 31 seconds). The time from the first LFP cell venting to the completion of thermal runaway in the last cell was a total of 2330 seconds. The time from the first NMC cell venting to the completion of thermal runaway in the last cell was a total of 838 seconds.

The peak HRR for the NMC module was 16.98 kW; however, the oxygen analyzer malfunctioned due to the deflagration. Since the LFP module did not ignite and consume oxygen, the calculated HRR was 0 kW; however, this does not reflect the energy release potential of the module. The time for propagation of thermal runaway throughout the LFP module (1715 seconds) was found to be approximately twice as long as in the NMC module (816 seconds). H_2, CH_4, C_2H_4, C_3H_6, CO, and HF were released at significantly higher concentrations in NMC modules. CO and CO_2 were the primary gases produced by both cell chemistries. The gases produced from the NMC modules had a greater peak fractional effective dose (FED)[1] and fractional effective concentration[2] (FEC) values (0.13 and 0.168) compared to the values for LFP (0.017 and 0.01). The LFP module

[1] The FED model compares the concentration of asphyxiant gases, carbon monoxide and hydrogen cyanide, against doses known to cause the effect being evaluated, e.g., incapacitation. The model assumes the impact of CO and HCN are additive and considers the impact of carbon dioxide on respiratory rate. An FED less than 1 indicates that the effect was not reached.

[2] The FEC model compares the concentration of irritant gases, like HF, HCl, HBr, acrolein, etc. against doses known to cause the effect being evaluated, e.g., incapacitation. The model assumes the effects of irritants is additive. An FEC less than 1 indicates that the effect was not reached.

was found to produce a total of 8.54 g of CO, 18.2 g of CO_2, 5.4 g of HCl, and 5.24 g of NH_3. HF was not detected during the LFP experiment. The NMC module was found to produce a total of 68.4 g of CO, 1473 g of CO_2, 1.3 g of HCl, and 2.9 g of HF. NH_3 was not detected during the LFP experiment. NH_3 was not detected in NMC thermal runaway, whereas LFP produced NH_3. There was a larger amount of ejected combustible gases per failed NMC cell (21.09 g) compared to the total ejected combustible gases per failed LFP cell (4.17 g).

3.1.21. INERIS, 2022

In 2021, the French National Institute for the Industrial Environment and Risks (INERIS) performed analyzed emission factors for a variety of fuels including Li-ion batteries. FTIR was used to detect chemical compounds including CO, NO_x, acid gases, and formaldehyde. FID was used to measure VOCs. In addition, metals, polychlorinated dibenzo-p-dioxins and furans (PCDD/F), and polycyclic aromatic hydrocarbons (PAH) (23 substances) were sampled and analyzed. The test results showed that for Li-ion battery fires (50% SOC) the maximum CO/CO_2 ratio[3] was 0.04, and the ratio during steady-state burning was 0.03. The maximum CO/CO_2 ratio was less than all other fuels tested, but the ratio during steady state burning was like mixed plastics. The overall VOC emission factor for Li-ion batteries was 8,420 mg/kg which was nearly equivalent to that found for oil (8,880 mg/kg). This emission factor was more than natural wood (1,500 mg/kg) and high-density polyethylene (HDPE) (4,200 mg/kg) but significantly less than mixed plastics (21,800 mg/kg), polyvinyl chloride (PVC) (37,500 mg/kg), and shredded tires (54,050 mg/kg). A summary of emission factors is presented in Table 27.

[3] The CO/CO2 ratio is used to evaluate combustion efficiency. A larger CO/CO2 ratio indicates less efficient combustion and higher CO production along with higher production of other unburned hydrocarbons.

Table 27. VOC emission factors for various fuels (INERIS, 2022)

Fuel	VOC Emission Factor [mg/kg]
Natural Wood	1,500
Plywood	440
Chipboard (particle board)	590
OSB	785
HDPE	4,200
PVC	37,500
Oil	8,880
White spirit	4,680
Shredded tires	54,050
Li-ion Batteries (NMC) (50% SOC)	8,420
Plastic mix (PE+PMMA+PVC)	21,800
Crushed IT Equipment	35,000
Ethanol	760
Heptane	3,800

PMMA: polymethyl methacrylate
IT: information technology

The overall PAH emission factor for Li-ion batteries was found to be 45 mg/kg, similar to that found for crushed information technology (IT) equipment (60 mg/kg). This factor was more than those observed for natural wood (28.7 mg/kg), but significantly less than mixed plastics (1,311 mg/kg), PVC (526 mg/kg), and shredded tires (2,120 mg/kg). The results of the emission factors for all the fuels tested are presented in Table 28.

Table 28. PAH emission factors for various fuels (INERIS, 2022)

Fuel	PAH Emission Factor [mg/kg]
Natural Wood	28.7
Plywood	23.3
HDPE	320
PVC	526
Oil	0.55
White spirit	510
Shredded tires	2,120
Li-ion Batteries (NMC) (50% SOC)	45
Plastic mix (PE+PMMA+PVC)	1,311
Plastic mix w/ extinguishment	360
Crushed IT Equipment	60

A summary of the average emission factors for Li-ion Batteries determined through the series of tests performed by INERIS (2022), is presented in Table 29.

Table 29. Emission factors for Li-ion batteries (INERIS, 2022)

Species	Average Emission Factor
CO_2	980 g/kg
CO	14 g/kg
CO/CO_2	0.014
NO_x	0.9 g/kg
HCN	0
HF	7 g/kg
HBr	0
HCl	0
SO_2	0
Soot	2.1 g/g
Metals	17 g/kg
Total VOC	8.4 g/kg
Formaldehyde	0.5 g/kg
PAH	0.045 g/kg
PCDD/DF	Not Measured
PBDD/DF	Not Measured
PCB	Not Measured

PBDD/F: polybrominated dibenzo-p-dioxins and furans
PCB: polychlorinated biphenyls

Emission factors for a wide variety of other fuels were also identified by INERIS (2022). Based on these values, the Li-ion battery emission factor for HF (7 g/kg) is observed to be like the HF emission factors for electric cables (8.3 g/kg) and pesticides (9.0 g/kg) and significantly more than those for the other fuels, many of which had an emission factor of 0 g/kg. Additionally, the emission factor for metals from Li-ion batteries (17,000 mg/kg) and tires (60,000 mg/kg) were clear outliers from the other fuels, for which most had an emission factor of 0 mg/kg. The soot emission factor for Li-ion batteries (2.1 g/g) was also observed to be elevated compared to most other fuels.

Conversely, yields of HCN, HBr, HCl, and SO_2 were reported to be 0 g/kg for Li-ion batteries, but were produced from other common fuels such as PU (HCN = 1.8 g/kg), computer equipment

(HBr = 14 g/kg), PVC (HCl = 320 g/kg), and home appliance products (SO_2 = 7 g/kg). Yields of NO_x were reported to be significantly elevated for fuels such as PU (90 g/kg), and clothes (7.2 g/kg) compared to Li-ion batteries (.9 g/kg).

3.1.22. Larsson et al., 2016

In the study performed by Larsson et al. (2016), LFP and NCO modules were exposed to an external heat source to assess toxic gas emissions and heat release rate. HF production was measured via FTIR and gas-washing bottles. HF measurements using gas-washing bottles produced levels twice as high but within the same order of magnitude.

Table 30 presents the results of the tests and HF measurements obtained using FTIR.

Table 30. HRR and HF yields from Li-ion cells (Larsson et al., 2016)

Test ID	Cell Type	Cell Geom	No. Cells	Capacity [Ah]	SOC [%]	Mass Loss [g]	Peak HRR [kW]	THR [kJ]	Peak HF Conc. [ppm]	Total HF [g]	HF Yield [mg/g]	HF Yield [mg/Wh]
A	LFP	Cylind.	9	28.8	100	145	29	2766	9	2.2	15	24
B	LFP	Cylind.	9	28.8	50	155	19	2502	5	1.1	7	12
C	LFP	Cylind.	5	40	100	406	31	6605	16	7.6	19	58
D	LTO-NCO	Pouch	2	60	100	419	53	6893	100	6.4	15-27	46-81

Geom: geometry
Cylind: cylindrical
Conc: concentration

The study observed that cells with a 100% SOC produced higher peak HRRs and higher amounts of HF. It was also observed that the cell voltage breakdown appeared to occur simultaneously with HF gas emissions from the cell. Mass flow of HF was found to reach a peak value of approximately 3.0 mg/s, 1.8 mg/s, 8.0 mg/s, and 34.0 mg/s for Tests A, B, C, and D,

respectively. Mass flow of HF was found to reach a peak 1-minute average value of approximately 2.4 mg/s and 1.1 mg/s for Tests A and B respectively; 1-minute averages of HF mass flow were not reported for Tests C and D.

3.1.23. Larsson et al., 2017

In the analysis performed by Larsson et al. (2017), it was identified that $LiPF_6$ and other lithium salts containing fluorine are found in the electrolyte of typical Li-ion batteries. These fluorine-containing electrolytes can vaporize and be vented from Li-ion battery cells during an overheating event such as a fire or thermal runaway. In such an event, the fluorine in the electrolyte, or in other components (i.e., PVdF binders in the electrodes, flame retardants in separators, and fluorophosphates in electrode materials), can be released as HF, PF_5, and/or POF_3. It was also noted that the decomposition of $LiPF_6$ can be accelerated in the presence of water.

The analysis included experimental testing of seven different types of Li-ion batteries exposed to an external heat source which led to ignition of the battery cells. Tests within the same battery type were also conducted with various SOC. It was observed that the HRR only experienced distinct peaks when the cells were at a 100% SOC. At lower SOC, the HRR curves were relatively smooth. The peaks in the 100% SOC tests were attributed to the violent venting of cells which led to ignition of emitted gas and intense flares. While there were significant differences in the peak HRR for cells at a different SOC, the THR normalized by capacity in Wh varied little. The peak amount of HF produced was also highly dependent on the SOC, however the total amount of HF produced normalized by capacity was mostly dependent on the cell type, not the SOC.

HF was measured by FTIR and gas-washing bottles. Generally, the gas-washing bottles measured higher levels of HF, however, trends were similar across both detection methods. Pouch

type cells were found to produce the highest levels of HF; this was hypothesized that this was due to cylindrical and prismatic cells requiring a higher pressure in order to vent, thus resulting is a more rapid release of electrolyte vapors and a less complete burning of these vapors. A summary of the HRR and HF production measured during 100% SOC tests is presented in Table 31.

Table 31. HRR and HF production of Li-ion batteries (Larsson et al., 2017)

Test ID	Cell Type	Cell Geom	No. Cells	Capacity [Wh]	SOC [%]	Avg. Peak HRR [W/Wh]	Avg. THR [kJ/Wh]	Avg. HF Yield[1] [mg/Wh]	Peak HF Conc.[2] [ppm]	Max HF Prod. Rate[2] [mg/s]
A	LCO	Prism.	5	128	100	612	18.1	19.8	-	-
					50	416	18.0	18.5	-	-
					0	214	16.8	21.6	-	6.9
B	LFP	Pouch	2	128	100	538	46.9	166.8	162	55
C	LFP	Pouch	5	112	100	461	69.5	53.9	-	-
					50	149	70.5	141.3	-	-
D	LFP	Cylind.	9	92	100	315	30	24	-	-
E	LFP	Cylind.	5	132	100	235	50	52	-	-
F	NCA	Pouch	2	138	100	384	50	55	-	-
G	18650	Cylind.	2	124	100	460	28	15	-	-

[1]Measured via FTIR
[2]Excludes tests that involved application of water mist.
Prism: prismatic
Prod: production

Production of POF_3 could only be detected in two tests of Type A batteries at 0% SOC. The normalized total yield of POF_3 from these two tests was calculated to be 15 to 22 mg/Wh. The effect of the application of water mist on the production of HF was also assessed in the series of tests. Water application temporarily increased the rate of release of HF but did not have a significant impact on the total amount of HF released.

3.1.24. Lecocq et al., 2016

Singl-cell tests were conducted on pouch, LFP cells with a capacity of 1.3 Ah/4.2 Wh and a mass of 38 g. Tests were performed with either $LiPF_6$ or LiFSI electrolyte to see if electrolyte composition influenced gas emissions, HRR, and/or MLR. The cells were charged to 0, 50, or

100% SOC. The pouch cells were ignited using the Tewarson apparatus radiating a 25 kW/m^2 heat flux and a pilot flame. A hood was utilized for gas collection. Samples were analyzed for CO, CH_2O, HCN, NO_x, SO_2, HF, and fluorinated species using FTIR.

The LiFSI electrolyte cells had an abrupt heat release at 50 and 100% SOC, unlike the $LiPF_6$ electrolyte cells. Th authors proposed that the rapid release may be due to the sudden and highly exothermic redox process between the electrode and LiFSI. The exothermic process could cause the electrolyte to evaporate rapidly, resulting in rapid combustion. At 0% SOC, neither electrolyte had a significantly rapid reaction. The shorter peak at 0% SOC for the LiFSI electrolyte cells indicates that it might be more reactive than $LiPF_6$. The total gas production is shown in Table 32.

Table 32. CO, HF, and SO2 gas production (Lecocq et al., 2016)

Electrolyte	SOC [%]	Total Gas Production [g]			Peak Gas Production Rate [mg/s]		
		HF	CO	SO_2	HF	CO	SO_2
$LiPF_6$	100	207	366	0	4	21	0
	50	356	298	0	2.5	8	0
	0	437	235	0	1.8	4	0
LiFSI	100	10	279	118	0.1	25	2.8
	50	14	197	142	0.1	12	3.2
	0	47	109	200	0.2	2	3.4

The production of HF tended to decrease with SOC for $LiPF_6$. Lecocq et al. (2016) proposed that either a) certain formation processes are dominant during flaming, or that b) cells at a lower SOC have a longer fire duration and could maintain the decomposition temperature required for HF production longer. The production of HF in $LiPF_6$ is a magnitude greater than production in LiFSI. The authors noted that this difference could be due to $LiPF_6$ thermally decomposing into gaseous PF_5 rapidly. They reasoned that gaseous PF_5 is very reactive and can easily diffuse outside the cell to form HF. On the other hand, LiFSI does not decompose into a gas and release fluorine. Only

LiFSI produced SO_2, decomposition may take place inside the cell which may favor formation of Li_2SO_4.

3.1.25. Lee & Stoliarov, 2018

Lee and Stoliarov (2018) performed testing on various arrays of cylindrical LCO cells to better understand dynamics, energetics, and gaseous emissions of Li-ion battery pack failures. The individual cells had a capacity of 2.6 Ah, a nominal voltage of 3.7V, and a mass (without packaging) of 43.57 g. At 100% SOC, the average stored electrical energy was calculated to be 34.1 kJ.

A series of tests were performed to assess the amount of heat generated chemically from the reactions between the battery cell components without combustion, as well as heat generated from flaming combustion of the cells. The tests showed that at 100% SOC, approximately 59 kJ of heat was generated per failed cell, i.e., 1.73 kJ of heat generated per kJ of stored electrical energy without flaming combustion. Meanwhile, the tests showed that heat generated from flaming combustion of the cells was approximately 63 kJ; these results represented fire conditions that were under-ventilated. For well-ventilated conditions, values of 107 kJ/cell and 3.35 kJ/ kJ stored electrical energy were achieved.

The dynamics of thermal runaway within the cell arrays was also studied. Generally, it was found that a cell went into thermal runaway when, at least, one adjacent cell had undergone thermal runaway. While the propagation trends were similar throughout the tests, timing of cell failure was found to be considerably varied, despite well-controlled conditions.

3.1.26. Liu et al., 2020

The authors induced thermal runaway in Li-ion batteries to characterize combustion and fire behavior, as well as gas release. The cells used were prismatic LFP Li-ion batteries with $LiPF_6$ electrolyte. The cells had a capacity of 22 Ah and a nominal voltage of 3.2V. The cells were tested at 0, 50, 75, and 100% SOC. Cells were placed under a hood for gas sampling. A Servomex 4100 analyzer was utilized to determine O_2, CO_2, and CO concentrations. A semiconductor gas sensor was utilized for H_2, and an optical gas sensor was utilized for HF. Thermal runaway was initiated using a 500 W heating plate wrapped around the surface of the cell. Piloted ignition was used to ignite combustible gases. The HRR contribution from the igniter was subtracted from total HRR to isolate the contribution from the cells. Thermocouples were placed on the cell surface, tabs and above the safety valve to measure temperature. The 75% SOC cell was only analyzed for HRR and THR.

The authors divided flaming thermal runaway into three stages: venting, ignition and combustion, and extinguishment or jet flow. Combustion was initially stable, then thermal runaway triggered jet fire for the higher SOC cells. No jet fire or thermal runaway were observed for the 0% SOC cell. The authors found that the 100% SOC cells vented within a shorter period of time compared to the 0 and 50% SOC cells. The flaming period for the cells at 100% SOC was shorter compared to flaming period for 0 and 50%. Additionally, the 100% SOC cell had more violent jet fire and jet flow during extinguishment compared to the 50% SOC cell. The higher SOC cells ejected a larger quantity of cell contents, including electrolyte, generated gases, and materials from the separator, electrode, and binders.

Table 33 shows the peak HRR and THR of the cell for each SOC. The HRR values for the 100% SOC cells are smaller than those for the 50% SOC cells due to the significant smoke generation during the jet fire and the jet flow. The 75% SOC cells had the highest peak HRR and THR.

Table 33. Combustion characteristics of cells at different SOCs (Liu et al., 2020)

SOC [%]	Peak HRR [kW]	THR [kJ]	TR Temperature [°C]
0	5.68	1749.51	N/A
50	11.14	2034.41	198.6
75	13.91	2405.77	-
100	6.02	1214.92	184.5

CO production tended to increase with SOC, which indicated that combustion efficiency decreased with SOC. The authors attributed this trend to the longer stable combustion time in lower SOC cells, violent ejection of cell contents in higher SOC cells, and the reduction of CO_2 with Li_xC_6 for higher SOC cells. H_2 production was attributed to reactions between the PvDF binder and Li_xC_6, and only occurred in the 100% SOC cell test. Total HF released was significantly higher for 100% SOC cells. Additionally, the amount of HF absorbed into battery components is less for 100% SOC cells. The 100% SOC cells released larger quantities of HF due to the larger amounts of electrolyte bursting and the higher venting pressure. The authors note that the HF may have lost reactivity through interactions with NH_3 and the reported values give the lowest HF production.

3.1.27. Liu et al., 2021

Liu et al. (2021) performed testing on commercial LFP Li-ion batteries to assess thermal runaway behavior and the toxicity of vented gases. The batteries utilized in the tests consisted of two LFP pouch cells connected in parallel. The total nominal capacity of the battery was 243

Ah/778 Wh. The batteries were tested at 0, 50, and 100% SOC. Two cases of tests were conducted. In Case 1, an igniter at the safety valve opening was used to ignite the vent gases. In Case 2, no igniter was used, and no flaming ignition occurred. Thermal runaway was initiated via an electric heating plate and a ceramic fiber blanket enwrapped the battery and heater. Tests were conducted within a combustion chamber and products of combustion were captured via an exhaust hood and a sampling duct. Oxygen, carbon monoxide, and carbon dioxide were quantified online via a gas analyzer and HRR was determined based on these measurements and the method of oxygen consumption. Additional gases were analyzed with FTIR.

In Case 1, the cells underwent four stages of behavior during the tests. In stage 1, the safety valve opened and vented gases, which subsequently ignited and caused deflagration. In stage 2, the flame reduced in size and continued to burn in a steady state. In stage 3, a vertical jet flame occurred, however cells at 0% SOC did not experience the jet flame stage. In stage 4, the flames decreased until extinguishment.

In Case 2, the batteries released an initial jet flow of gas, but this release was of short duration. The batteries then experienced a stable state at which small amounts of smoke were emitted, with a downward behavior. The authors determined the gases released during these initial stages were electrolytes. The batteries then experienced a violent venting stage, which in the 100% SOC tests, ejected solid materials as well. Cells at 0% SOC did not exhibit the violent venting stage. After the major venting event, emissions decreased and eventually ceased. The authors noted that for flaming conditions, when compared to non-flaming conditions, the time from initial venting to the onset of thermal runaway during is decreased by 23% in the 50% SOC cases and 37% in the 100% SOC cases. Table 34 presents results from the tests regarding thermal behavior.

Table 34. Heat release and mass loss from LFP batteries (Liu et al., 2021)

Test ID	SOC [%]	TR Onset Temperature [°C]	Peak HRR [kW]	THR [kJ]	Δh_c [kJ/g]	Mass Loss [g]	Peak MLR [g/s]
1	0	NA	35.4	12839	13.7	940	<0.5
1	50	228	37.7	14101	14.3	986	1.5
1	100	194	88.6	19531	17.2	1136	5.0
2	0	NA	NA	NA	NA	918	<0.5
2	50	223	NA	NA	NA	973	1.6
2	100	188	NA	NA	NA	1112	4.5

Δh_c: heat of combustion

The effective heat of combustion was calculated as an average based on the total heat released and the total mass loss. The authors noted that the total heat released increased with increasing SOC but that the heat of combustion remained relatively constant.

Table 35 presents results from the tests regarding vent gas production. Gas production quantities were not reported for Case 2 (non-flaming) tests.

Table 35. Vent gas emissions from LFP batteries (Liu et al., 2021)

Test Case	SOC [%]	Total Gas Production [g]							Peak Gas Production Rate [g/s]						
		CO	CO_2	HF	NO	HCl	NH_3	SO_2	CO	CO_2	HF	NO	HCl	NH_3	SO_2
1	0	3.4	688	1.6	0.34	0.71	0.5	1.75	.07	8	.04	.005	.015	.01	.03
1	50	5.9	773	2.8	0.48	0.68	0.47	2.26	.07	6	.07	.006	.013	.01	.05
1	100	12.3	1683	8.1	2.61	0.79	0.56	4.32	.04	8	.13	.008	.023	.017	.08

3.1.28. Lopez et al., 2015

Cylindrical and prismatic LCO cells were tested to determine if shape, spacing, connection method, and insulation influenced thermal runaway behavior. The cylindrical cells were 18650 cells, 2.8 Ah capacity equipped with side vents. The prismatic cells had a capacity of 5.3 Ah and were equipped with a header vent.

Table 36 shows the specifications of each test.

Table 36. Module specifications (Lopez et al., 2015)

Cell Geometry	Electrical	Connection	Spacing	SOC	Material
Cylindrical	9P	M-type	1 mm	100%	None
Cylindrical	9P	M-type	2 mm	100%	None
Cylindrical	9P	M-type	4 mm	100%	None
Cylindrical	9P	S-type	1 mm	100%	None
Cylindrical	9P	S-type	2 mm	100%	None
Prismatic	9S	Alternating	2 mm	100%	None
Prismatic	4P	M-type	8 mm	100%	Radiant Barrier
Prismatic	4P	M-type	8 mm	50%	Radiant Barrier
Prismatic	9P	M-type	5 mm	50%	Intumescent

P: parallel
S: series

One cell in each module was forced into thermal runaway via film heaters. For the 9-cell modules, cell 9 at the center was the initiating cell; Cell 4 was the initiating cell for the 4-cell module. The film heaters were shut off after the initiating cell went into thermal runaway. Thermal runaway was defined as a surface temperature exceeding 200°C. The initiating cell had a 1 A current and 20V applied to it. Surface temperature and open circuit voltage (OCV) were measured to characterize thermal runaway.

The cylindrical cells adjacent to and/or electrically connected to the initiating cell had overall higher temperatures and lower OCVs. There was excessive smoke and high temperatures, but no flaming, rupture, or thermal runaway propagation. At closer spacings (1 to 2 mm), there was more char and melting plastic on the cells near the trigger cell. The average and maximum temperatures of adjacent cells were higher at closer spacings. Directly adjacent cells suffered more damage than diagonal cells. The cells connected by serpentine tabs had higher maximum temperatures and a larger decrease in open circuit voltage.

The wider spacing in the prismatic modules did not prevent thermal runaway propagation or temperature increase due to the side vents releasing hot gases that heated up surrounding cells.

Measurements showed that the surrounding cells were heated over 600°C, indicating that they also underwent thermal runaway. All cells in the 9-cell prismatic modules read 0 OCV except cells 1 and 9. With the addition of insulation, the trigger cell was able to eject without affecting the other cells. Unlike the uninsulated modules, no evidence of venting or burned tabs was found. Temperature rise was not sustained, and the cells had higher OCVs at the end of the test.

For the prismatic modules at 50% SOC, no flaming was visible, unlike 100% SOC modules. There were no sustained high temperatures or venting in cells aside from the initiating cell. Three out of the four cells had low OCVs. However, there was still significant charring and melting at initiating cell.

3.1.29. Mayonado et al., 2024

To evaluate the effectiveness of UL 9540A test standard data for predicting thermal runaway propagation and associated hazards, Jensen Hughes, Inc. conducted a meta-analysis of data from publicly available UL 9540A tests. Mayonado et al. (2024) found that protocol in UL 9540A tends to give the lab at which testing is conducted discretion on where and how to initiate thermal runaway, as well as the number of cells that are forced into thermal runaway to assess propagation. There was a larger percentage of failed cells in the module level tests compared to their respective unit level tests. The authors noted that this discrepancy may have been caused by the lower percentage of cells forced into thermal runaway during unit level testing compared to module level testing. Additionally, the authors found that a majority of UL 9540A tests reported a peak HRR of 0 kW. The authors noted that during thermal runaway, heat is generated by rapid electrical discharge, the decomposition of the cell contents, and the hot gases released. However, oxygen consumption calorimetry does not capture these sources of heat and are more suited to combustible

fires. The authors concluded that the 0-kW peak HRR measurements underestimate the heat release potential of Li-ion cells. Table 37 presents the results of the meta-analysis for LFP and NMC cell level tests. Data reporting a peak HRR or THR of 0 was excluded.

Table 37. Heat release and gas production data from UL 9540A cell level tests of LFP and NMC cells (Mayonado et al., 2024)

Cell Type	Geometry	SOC [%]	Peak HRR [kW/Wh]	THR [kJ/Wh]	Total Gas Production [L/Wh]
LFP	Cylindrical	100	0.63	10	0.74
LFP	Pouch	100	0.44	16	0.43
LFP	Prismatic	100	0.29	14	0.03
NMC	Cylindrical	100	0.57	3	0.48
NMC	Pouch	100	0.49	4	0.55
NMC	Prismatic	100	0.17	1	0.48

The authors noted that heat release behavior is significantly influenced by cell chemistry and cell geometry and that measured peak heat release rates can vary greatly depending on the measurement technology used. They also noted that cell level UL 9540A data tends to predict higher peak HRR normalized by electrical energy and lower total heat released normalized by electrical energy, when compared to results from Ditch & Zeng (2020) which evaluated a full-scale unit. Based on this, for full scale Li-ion battery peak heat release rate bounding, Mayonado et al. (2024), estimated a peak HRR of 0.2 kW/Wh. In looking at the gas production data, the authors observed that total gas quantities also vary greatly by cell chemistry and cell geometry and may also be influenced by failure modes and test instruments.

3.1.30. Meng et al., 2020

Meng et al. (2020) investigated the correlation between SOC and combustion behavior and toxicity in LFP Li-ion cells undergoing thermal runaway. The cells utilized in the test were 22

Ah/81 Wh, prismatic LFP cells charged to 0, 50, and 100% SOC. Thermal runaway was initiated via an electric heater attached to one side of the battery. The battery and heater were enwrapped with a noncombustible aluminum silicate insulation to prevent heat loss to the environment. An igniter was utilized to ignite the vent gases as they were released from the cell. The tests were conducted in a combustion chamber equipped with a collection hood and exhaust system. Gas was sampled from the exhaust duct and an oxygen analyzer was used to determine concentrations of oxygen, CO, and CO_2. HRR was determined using the oxygen consumption method. HF concentrations were determined via a gas analyzer with an optical gas sensor for HF.

In the 100% SOC and 50% SOC tests, as the cells were heated, they began to expand due to production of gases within the cell from the reaction of electrolyte and electrode materials. The internal pressure continued to increase until the safety valve opened, emitting white electrolyte and other combustible gases. These gases were ignited by the manual igniter and a stable stage of combustion occurred as gases continued to be emitted. The cells then underwent a stage of reduced combustion intensity, followed by a violent ejection of cathode and anode materials and a large amount of electrolyte and other gases, creating a vertical jet fire. Another stable combustion stage continued until the fire started to decay and eventually extinguished.

It was found that 50% SOC cells took longer to vent and enter thermal runaway, with an overall longer period of combustion. The 0% SOC cells only experienced one stage of stable combustion and no jet fire. In the 100% SOC test, which experienced the highest temperatures, the maximum surface temperature of the cell was 451°C and the maximum flame temperature was 943°C, at 5 cm above the safety valve.

Table 38 presents the results for HRR and gas production.

Table 38. Heat release and gas production data from tests of prismatic LFP cells (Meng et al., 2020)

SOC [%]	Peak HRR [kW]	THR [kJ]	Total Gas Production [g]			Peak Production Rate [g/s]		
			CO	CO_2	HF	CO	CO_2	HF
0	6.2	2116	4.6	156.4	0.4	0.016	0.50	0.004
50	12.1	1855	8.5	147.5	1.4	0.051	1.18	0.0175
100	12.3	1317	2.8	126.3	2.3	0.024	1.18	0.037

The authors noted that the production of HF increased with increasing SOC, with regards to both total production and peak production rate. Total CO_2 production increased with decreasing SOC, but the peak production rate was highest in the 50 and 100% SOC tests. Total CO production and peak CO production rate were highest in the 50% SOC test.

3.1.31. Nedjalkov et al., 2016

Li-ion cells were tested in three different scenarios by Nedjalkov et al. (2016) to assess the toxic gas emissions from damaged Li-ion batteries. Slightly overcharged (4.3V), pouch NMC cells, with a capacity of 40 Ah were used in all tests. The cells had graphite anodes, and the electrolyte composition was EMC and EC with $LiPF_6$ salt. During the tests, emission gases were pumped to analyzers. GC-MS was used to detect EMC, DEC, EC, benzene, toluene, styrene, and biphenyl. Quadruple MS was used to detect benzene, toluene, acrolein, CO, and CO_2. Ion chromatography was used to detect HF.

The three test scenarios included (1) cell catching fire, (2) no combustion of cell, and (3) no combustion of cell and gas filtration. In all three scenarios, the cell was in a barrel and punctured with a nail to induce thermal runaway. In Test Scenario 1, the barrel cover was partly shut to prevent the barrel from exploding and to retain most of the emission gases. HF, CO, and CO_2 were not measured in this test scenario. In Test Scenario 2, the cell was wrapped in a gas-permeable,

textile composite structure to prevent flaming combustion. Test Scenario 3 was run in the same manner as Test Scenario 2 except that a gas filtration unit was mounted on top of the barrel and all gas emissions were collected after filtration. The filter consisted of five levels; a coarse particulate separator, activated charcoal, potassium permanganate, activated alumina, and a fine particulate filter. It was found that Scenario 2, i.e., no flaming combustion or filtration, produced the highest concentrations for each gas. In each test, the total volume of vent gases produced from the cell was approximately 200 liters.

It was reasoned that the flaming combustion of the cell in Scenario 1 produced less toxic gas emissions because the reaction of the organic compounds with oxygen produced CO_2 and H_2O. However, only a portion of the VOCs released from the cell were combusted due to the sudden venting of the cell causing the displacement of atmospheric air within the barrel; this reduction in available oxygen prevented complete oxidation of all components, and instead, these compounds, mainly consisting of the electrolyte's chemistry of EMC and EC, were exhausted. Traces of DEC, benzene, toluene, styrene, and biphenyl were detected. In Scenario 2, almost no oxidation took place, and therefore, a larger amount of unburned organic substance was exhausted. There were 155 different constituents detected in Scenario 2. It was reasoned that this variety, along with the higher concentrations of the gases, was due to the thermal decomposition of EMC electrolyte. The EMC was thought to be decomposed into free ethyl and methyl radicals, as well as free vinyl and ethylene radicals. These radicals can lead to the formation of various VOCs and PAHs (Nedjalkov et al, 2016). HF was not measured in the flaming combustion scenario. HF was measured in Scenario 2 and found to be 1,640 ppm. Production of HF was attributed to the decomposition of the LiPF6 salt in the electrolyte.

3.1.32. Peng et al., 2020

Peng et al. (2020) studied the release of toxic gases from thermally induced failure of Li-ion battery cells. In their tests, thermal runaway of a single 68 Ah pouch cell was induced via an external heater. The cells had a nominal voltage of 3.22V, an initial mass of approximately 1250 g, and $LiFePO_4$/graphite electrodes. Tests were run with the cells at 0, 50, 75, and 100% SOC. The tests were conducted in a well-ventilated chamber, and gas samples were extracted from the exhaust stream and analyzed for toxic gases via FTIR. An electric spark igniter was placed near the bottom of the battery to ignite vented flammable gases.

The tests showed that, regardless of SOC, the cells exhibited common burning behaviors, separated into the following five stages:

1. Heating and expansion- At this stage, the cells are being heated externally. The surface of the cells shows slow expansion due to an increase of pressure inside the cell caused by the accumulation of thermal decomposition gases. Eventually, some flammable gases are vented and ignited by the electric spark igniter.
2. Stable combustion with small flame- At this stage, the vented gases from the cell are burning in a small, stable fire.
3. Jet fire- During this stage, the fire is initiated when the separator in the cell fails causing thermal runaway. A significant release of gases results in a high-speed, jet flame.
4. Second stable combustion- At this stage, the combustion returns to being stable, though larger than the Stage 2 combustion.
5. Abatement and extinguishment- At this stage, the fire decays until extinguishment.

It was observed that cells with a larger SOC had a longer and more violent jet flame in Stage 3, and a larger fire at Stage 4. HRR was also measured during each test, and cells with a higher SOC had a higher peak HRR. The heat release rate per unit area (HRRPUA) was derived from these results and calculated to be 2.1 MW/m^2 for the cells at 100% SOC. The cells at 100% SOC produced the highest THR value. THR results for each SOC are presented in Table 39, along with peak HRR and ignition times.

Table 39. Total HRR of Li-Ion cells at various SOC (Peng et al., 2020)

SOC [%]	Ignition Time [s]	Peak HRR [kW]	THR [kJ]
0	825 ± 58	3.7 ± 0.5	4165 ± 356
50	775 ± 68	25.8 ± 1.6	5644 ± 317
75	759 ± 65	70.2 ± 7.2	6388 ± 431
100	738 ± 7	80 ± 2.6	6660 ± 419

Table 40 shows the gas concentrations at various SOCs. CO production was measured during the tests, and the peak CO concentration was 258 ppm produced at 100% SOC. HF, SO_2, NO, NO_2, NO, and HCl were also analyzed during the test using FTIR. Only the peak concentration of HF (165 mg/m^3) was found to exceed the IDLH limit (24.6 mg/m^3). This measurement was taken in the exhaust stream close to the source.

Table 40. Summary of peak gas concentrations at various SOC (Peng et al., 2020)

SOC [%]	CO [ppm]	CO_2 [%]	HF [mg/m^3]	SO_2 [mg/m^3]	NO [mg/m^3]	NO_2 [mg/m^3]	HCl [mg/m^3]
100	265	1.35	165	115	17	12.5	8.4
75	200	1.1	120	105	16	10.8	6
50	25	0.5	60	60	9	3	3.6
0	0	0.1	20	5	7	2.4	4

HF production was attributed to electrolyte ($LIPF_6$), the PVdF binder, and possibly coating materials, such as AlF_3. SO_2 production was attributed to sulfur-based compounds used as reduction-type additives. NO and NO_2 are considered reaction products, and HCl production was attributed to flame-retardant additives in the plastic packaging of the cell.

In connection with the experimental tests, Peng et al. (2020) performed a toxicity analysis using the methods outlined in ISO 13571. The authors concluded that the effects of irritant gases are more significant than the effects of asphyxiant gases (CO and CO_2) although neither FED reached unity, i.e., the evaluated effect. He also concluded that HF and SO_2 would be more impactful than NO_x and HCl.

3.1.33. Premnath et al., 2022

To characterize the particle emissions produced by Li-ion battery thermal runaway events, Premnath et al. (2022) forced LFP and NMC modules into thermal runaway. The LFP modules contained 96 cylindrical cells, with a cell capacity of 8.28 Wh and a cell mass of 70 g. The NMC modules contained 30 pouch cells, with a cell capacity of 249 Wh and a cell mass of 820 g. Two LFP modules and the NMC module had thermal runaway initiated by nail penetration, and two LFP modules underwent overcharge.

An open-air calorimeter was used to sample gases. Two engine exhaust particle sizers (EEPS) were used to measure particles between 5.6 to 560 nm. One unit was coupled with a solid particle sampling system (SPSS) to measure solid particle number (PN) concentration and size distribution (Solid-EEPS). The other EEPS measured both solid and volatile components (Total-EEPS). A micro-soot sensor (MSS) with detection limits of 5 $\mu g/m^3$ and 50 mg/m^3 measured black carbon concentration. The EEPSs and MSS both took measurements in real time. Gravimetric filters

measured PM2.5 and were also sublimated to determine the volatile components. Organic carbon/elemental carbon (OC/EC) analysis was performed on samples captured by filters. Concentrations of CO_2, CO, CH_2O, NO, NO_2, HCl, HF, HCN, CH_4, and C_3H_8 were measured by FTIR. Table 41 shows a summary of measurements for all tests.

Table 41. Summary of particle results (Premnath et al., 2021)

Test	Test 1 (LFP, nail)	Test 2 (LFP, nail)	Test 3 (LFP, overcharge)	Test 4 (LFP, overcharge)	Test 5 (NMC, nail)
Duration [s]	260	266	1376	1392	1535
Black carbon [g/h]	0	0	149.9	182.78	66.52
Solid-EEPS [g/h]	0.13	0.1	220.42	170.25	123.86
Solid PN [particle/h]	1.56e15	1.12e14	8.89e16	6.11e16	1.06e17
Total-EEPS [g/h]	1.83	0.84	245.94	243.01	228.93
Total PN [particle/h]	4.24e15	1.61e15	1.13e17	1.83e17	2.08e17
PM2.5 [g/h]	1.81	0	386.09	375.97	551.03
PM2.5 volatile weight fraction [%]	-	-	19	20	8
OC [g/h]	-	-	181.5	150	94
EC [g/h]	-	-	27.5	123.6	93
OC/TC [%]	-	-	87	55	50

The LFP modules undergoing nail penetration produced visible smoke and flames. For Test 1, the fire lasted for one minute and self-extinguished. Test 2 only produced a small flame. Thermal runaway did not propagate to other cells. There were no significant peaks in gas production for Test 1, whereas Test 2 had peaks in alkyl carbonate compounds.

The LFP overcharge tests had more dramatic thermal runaway events compared to the nail penetration tests. Test 3 underwent smoke venting at 16 min after overcharging. Sparks appeared at 17 min 21 s, and the entire module caught fire, destroying the module. Similar events occurred in Test 4. There were significant peaks in CO_2, CO, and hydrocarbons. Peak HF concentration was measured at 177 ppm for Test 3. Test 4 produced similar concentrations for all gases.

Unlike the LFP nail penetration tests, the NMC module caught fire within seconds and thermal propagation spread throughout the module. By the end of the test, the entire module was destroyed. FTIR shows intense peaks in CO_2, CO, CH_2O, and NO during thermal runaway. HF was not observed in the NMC test and the authors contributed this to the lack of fluoride in the anion salt used in the cells.

Premnath et al. (2022) concluded that the initiation of thermal runaway (nail penetration vs overcharge), the cell chemistry, physical dimensions, and arrangement of cells in the module could influence emission characteristics. The HF concentrations for the LFP overcharge tests exceeded the IDLH threshold, i.e., 30 ppm, and the formaldehyde concentration for NMC nail penetration test exceeded the IDLH threshold, i.e., 20 ppm.

3.1.34. Sturk et al., 2015

Sturk et al. (2015) tested LFP and NMC pouch cells individually and in 5- or 10-cell modules to investigate the effects of abuse conditions. Modules were tested with physical connection only or with electrical and physical connection to assess if the electrical connection influenced thermal runaway behavior. The cells were charged to 25, 50, 75, or 100% SOC. Some cells were also completely discharged and short-circuited to produce 0V cells. HF production and HRR were measured for each test. Table 42 indicates the test specifications.

Table 42. Test specifications and methods (Sturk et al. 2015)

Test ID	Cell type	Geometric Configuration	SOC	# of tests	Fire exposure regime
A	LFP, 7 Ah	Single cell and bundles of 5 and 10 cells, respectively	0V and 100%	10	Test objects were exposed to a bonfire with a 15 kW flame for 15 minutes followed by 30 kW for an additional 5-25 minutes.
B	LFP, 7 Ah	Bundles of 5 cells	25%, 50%	4	Test objects were exposed to a bonfire with a 15 kW flame for 10 minutes followed by 30 kW for an additional 15 minutes.

			and 75%		
C	NMC, 14 Ah	E-vehicle battery pack: 200 cells arranged in 10 modules, total pack voltage 402V	80%	1	The burner underneath the pack supplied a HRR of 1.5 MW (comparable to a burning passenger car generating approximately 4 MW). The burner was on for 15 minutes. The battery pack was allowed to self-burn for an additional 15 minutes before extinguishing with water. Thermocouples were used to measure temperatures in 20 different locations in the pack.
D	NMC, 14 Ah	Bundles of 5 cells	25% and 75%	4	Test objects were exposed to a bonfire with a 15 kW flame for 10 minutes followed by 30 kW for an additional 15 minutes.
E	NMC, 14 Ah	Bundles of 5 cells	0V, 50% and 100%	5	Test objects were exposed to a bonfire with a 15 kW flame for 10 minutes followed by 30 kW for an additional 15 minutes.
F	NMC, 14 Ah	Bundles of 5 and 10 cells electrically connected cells in parallel	100%	5	Two 5-cell bundles and two 10-cell bundles were placed lying horizontally with respect to the flame. One 5-cell bundle was placed with cells oriented vertically with respect to the flame. Test objects were exposed to a bonfire with a 15 kW flame for 10 minutes followed by 30 kW for an additional 15 minutes.

While SOC tended to increase HRR for LFP cells, it appears that the activating effect of SOC rapidly dropped. There was no significant difference between the HRR for 50 and 75% SOC LFP cells. At 75 and 100% SOC, NMC cells showed a more rapid HRR onset and a rapid decrease in HRR. The cells with lower SOC had lower peak HRRs and a sustained curve. The peak HRR and for NMC cells was significantly greater than LFP cells. The higher HRR rates could be due to the higher reactivity in the NMC chemistry. The number of cells tended to increase the overall peak HRR; however, the contribution per cell decreased significantly. The modules at 100% SOC had a higher peak HRR compared to 0V.

The total energy released per cell remained relatively similar between LFP and NMC cells, for all SOCs. However, due to the higher capacity of the NMC cells, the energy released per Ah

capacity was significantly higher for the LFP cells. The total heat generated determined from tests of each cell chemistry at various SOCs is provided in Table 43.

Table 43. THR from tests of LFP and NMC 1-, 5-, and 10-cell configurations (Sturk et al., 2015)

Cell Type	THR per Ah [kJ/Ah]				
	0V	25% SOC	50% SOC	75% SOC	100% SOC
LFP	160	197	201	195	218
NMC	108	102	106	103	114

The NMC cells released significantly less HF than the LFP cells. For both cell chemistries, SOC tended to increase the total HF production; however, the total HF produced for the pouch cells at 0V was comparable to HF production at 75 or 100% SOC. The total HF generated per cell is provided in Table 44.

Table 44. HF production for LFP and NMC 5-cell physically connected modules (Sturk et al., 2015)

Cell Type	# Cells	Total HF Production [g]					Max HF Production Rate [mg/s]				
		0V	25% SOC	50% SOC	75% SOC	100% SOC	0V	25% SOC	50% SOC	75% SOC	100% SOC
LFP	1	1.5	-	-	-	0.9	11	-	-	-	5
LFP	5	12.4	5.6	11.7	12.0	14.3	13	6.5	13	18.5	18
LFP	10	37.6	-	-	-	41.1	19	-	-	-	26
NMC	5	3.66	1.55	2.86	2.19	4.76	5	-	10	-	27.5

An additional test (Test C) on an E-vehicle battery pack was conducted. The battery contained 200 NMC cells within 10 modules. The total pack voltage was 402V, and it was tested at 80% SOC. The NMC battery pack generated an HRR of 0.5 MW. No fluorinated compounds, including HF, were detected by FTIR. The authors did not offer an explanation as to why the battery pack produced no HF, whereas the NMC pouch cells still produced HF. The flames were extinguished

with water. While the battery did not reignite, it continued producing gases and maintained an internal temperature of 300 to 350°C for hours after quenching. Sturk et al. (2015) concluded that cell level test data on HF emissions and heat release rate cannot be easily extrapolated to multicell assemblies.

3.1.35. Sturk et al., 2019

Testing on two types of Li-ion pouch cells, LFP and NMC/LMO, was performed by Sturk et al. (2019) to assess the gases formed under heating conditions without ignition. The LFP cells had a rated capacity of 7 Ah and were charged to 3.3V and the NMC cells had a rated capacity of 14 Ah and were charged to 4.1V. The LFP cells each weighed 236 g and the NMC cells each weighed 385 g. In each test, five cells at 100% SOC were clamped together and placed on a heating plate. The heating plate induced thermal runaway of the bottom cell, which then propagated upwards through the other four cells. HF, as well as other gases of interest, were detected via FTIR and additional VOCs were analyzed using GC-MS.

The test results showed that the LFP cells produced a total gas volume of 50 L (42 L/kg of battery) oven an event duration of approximately 45 minutes while the NMC/LMO cells produced a total gas volume of 1500 L (780 L/kg of battery) over an event duration of approximately 4 minutes. The venting times of the LFP cells were observed to be approximately 10 times longer than the NMC/LMO cells. The total amount of HF measured via FTIR was 1.8 g (1.5 g/kg battery) for the LFP cells and 1.7 g (0.9 g/kg battery) for the NMC/LMO cells. While the total amounts for the two cells are nearly equivalent, when normalized to the cell energy, the LFP had a significantly higher yield of 16 g/kWh compared to 6.0 g/kWh for the NMC/LMO cells. Sturk et al. (2019) concluded that these results indicate that $LiPF_6$ quantities are not necessarily

proportional to battery weight and therefore, total production of HF can be hard to predict based on battery weight alone. It was also identified that the test results suggest that extended duration of a thermal event favors the production of HF. Other gases detected via FTIR included DEC, DMC, EMC, and PC. POF_3 could not be conclusively identified for either of the cell types. Additional VOCs identified using GC-MS and FID included benzene and toluene for the NMC/LMO cells.

3.1.36. Willstrand et al., 2020

Research Institutes of Sweden (RISE) performed a study of combustion characteristics and toxic gases produced during combustion of electric vehicles (EV) and internal combustion engine vehicles (ICEV). The analysis was divided into three parts- a literature review assessing both ICEV and battery electric vehicle (BEV) fires, full-scale fire testing on EVs, ICEVs, and Li-ion batteries, and FDS simulations of EV fires in an underground parking garage. RISE was particularly interested in the production of HF gas during combustion of EVs. The HF production was attributed to fluorinated materials in the vehicle battery packs, such as electrolytes containing $LiPF_4$.

As part of the literature review, available data on full-scale vehicle fire testing peak HRR, THR, heat of combustion, and emissions was gathered. In addition, the peak HRR and THR from Li-ion battery fires was obtained from previous fire testing of cells, cell arrays, and modules. Based on this analysis, it was concluded that there are no simple rules for estimating heat release rate of Li-ion battery fires, especially for large batteries or battery packs. HRR depended on the type of battery, SOC, configuration of the cells, and how the cells are exposed. The data retrieved from the literature review for peak HRRs was plotted by Willstrand et al. (2020). The trend was not

closely linear when considering the data sets independently. The same methodology was applied for total heat released and the correlation was found to be approximately linear, especially for assemblies with a high energy content.

A review of the BEV fire emissions found that HF was of particular concern. Other compounds identified PAHs, polychlorinated dibenzo-p-dioxins (PCDD), heavy metals including nickel, manganese, cobalt, and lithium, asphyxiant gases such as CO and HCN, and irritant gases including HCl, SO_2, and NO_2 being possible heat concerns.

Full-scale vehicle fire tests were performed on three vehicles below a collector hood: two EVs, referred to as BEV A and BEV B, and one ICEV, referred to as ICEV A. ICEV A (diesel engine) and BEV A (pouch, NMC cells) were full-size vans of the same model and manufacturer. BEV-B (prismatic, NMC cells) was a small, family car from Manufacturer B. In the tests, both BEVs were at 80% SOC, and the ICEV contained 44 liters of fuel. The fuel for the ICEV was split between its fuel tank and a diesel pool located directly below the tank. The pool was ignited to simulate a realistic fire scenario. The BEVs were ignited via a 30-kW propane burner located under the battery pack. The burner remained active for the entire test duration. Gas yields were collected through the hood with a 24 m^3/s flow rate and analyzed via FTIR, FID, gas washing bottles, and XAD-2 sorbent tubes.

Gas yields measured in the exhaust duct were not significantly different between the three vehicles, except for the production of HF. It was observed that the yields of HF from the two BEVs (2.3 and 2.1 mg/g) were orders of magnitude higher than the yield from the ICEV (.04 mg/g). HCN was detected in the tests for each of the three vehicles; however the peak yield only exceeded the defined detection limit in the test for BEV B. The gas yields are shown in Table 45.

Table 45. Gas yields from combustion of ICEV and BEVs (Willstrand et al., 2020)

Gas	ICEV A [mg/g]	BEV A [mg/g]	BEV B [mg/g]
CO_2	1,400	1,400	1,100
CO	25.5	31.5	23.8
THC	9.4	12.7	6.9
HF	0.04	2.3	2.1
HCl	4.4	6.4	4.5
HBr	0.1	0.5	0.2
HCN	-	-	0.4
SO_2	1.9	2.3	1.6
NO	1.8	1.5	1.5
NO_2	0.2	0.1	0.2
PAH	0.4	0.1	0.8

Table 46 shows the THR, mass loss, and effective heat of combustion for the ICEV and BEV tests. Contributions from the propane burner were excluded. ICEV A and BEV B have higher THRs compared to BEV A due to the larger combustible load in the full-sized vans. Mass loss was higher in BEV B due to the additional weight of the battery.

Table 46. Heat release and mass loss for vehicle fire tests (Willstrand et al., 2020)

	ICEV A	BEV A	BEV B
THR [GJ]	5.9	5.2	6.7
Mass loss [kg]	252	247	400
Mass loss [%]	19.0	15.6	25.6
Effective Δh_c [MJ/kg]	23	21	17

To evaluate scalability of testing, RISE performed small and medium scale fire tests of Li-ion batteries. These tests were performed using 40 Ah, prismatic, LMO/NMC cells with a capacity of 150 Wh and a nominal voltage of 3.9 V. The tests were performed in configurations of a single cell, two cells (300 Wh), a module (1.2 kWh), and a pack (8.4 kWh). The battery was at approximately 80% SOC. Emissions were sampled through a hood with a flow rate of 0.3, 1.0, and

12 m^3/s for single cell, double cell and module, and battery pack, respectively. FTIR, NDIR, gas washing bottles with high-pressure ion chromatography (HPIC), and a paramagnetic analyzer were used to analyze gas emissions.

The results showed that total heat released had a linear relationship with electrical energy. However, the peak HRR of the tests was not linearly correlated to energy, because a larger amount of heat was released over a longer period. This was attributed to the typical characteristics of thermal runaway in which the battery cells are not induced into thermal runaway or vented at the same time. When merged with THR and peak HRR data from the literature review and full-scale vehicle tests, the data showed good agreement with the previous data. Additionally, the full-scale fire test and battery test data were relatively close to the line of best fit (48.5 kJ/Wh).

The gas production from the battery tests were measured via FTIR and gas-washing bottles. HF was detected in all tests. HCl and HBr were detected in the module and pack tests, and SO_2 and NO were detected in the module tests. Table 47 provides the quantities of gases detected in each test.

Table 47. Gas yields from combustion of BEV packs, modules, and cells (Willstrand et al., 2020)

Gas	Pack	Module	Module	2 Cells	2 Cells	1 Cell	1 Cell	1 Cell	1 Cell
CO_2 [kg]	34	4.7	3.9	0.93	0.91	0.44	0.41	0.44	0.43
CO [g]	250	14	7.2	0.3	0.4	0.1	0.2	0.3	0.2
THC [g]	298	-	-	-	-	-	-	-	-
HF [g]	244	50	42	11	9.1	3.5	4.0	4.8	5.1
HCl [g]	111	1.9	2.0	<LOD	<LOD	<LOD	<LOD	<LOD	<LOD
HBr [g]	4.8	0.07	<LOD	<LOD	<LOD	<LOD	<LOD	<LOD	<LOD
SO_2 [g]	<LOD	18	22	<LOD	<LOD	<LOD	<LOD	<LOD	<LOD
NO [g]	<LOD	2.2	1.1	<LOD	<LOD	<LOD	<LOD	<LOD	<LOD
PAH [g]	8.8	-	-	-	-	-	-	-	-

Plotting of the HF quantities measured in all the battery tests showed a linear trend between total HF produced and the energy of the batteries. The quantity of HF production attributed to the battery pack in the full vehicle tests was compared to the trendline established by the battery-only tests; the total amount of HF produced by the vehicle batteries, when mounted in a fully equipped vehicle, is less than what is expected. The observed HF production was close to the lower limit determined from the cell tests. The study pointed out that this may have been the result of wall losses, as HF typically reacts when it contacts materials. With the battery located in the vehicle, many material surfaces are present compared to the open air burning of the battery cells and packs. Therefore, the probability of HF contacting a surface and reacting, prior to being transported in the plume, was greater.

3.1.37. Willstrand et al., 2023

Willstrand et al. (2023) performed tests on large format, prismatic NMC cells with a capacity of 157 Ah to determine whether SOC and the method of triggering thermal runaway affect gas production, mass loss, and thermal runaway onset. The cells were tested at 25, 50, 75, and 100% SOC, as well as an overcharge condition. The trigger methods were a heating ramp of 1 and 20°C/min, an external fire using a propane burner, a local heater, nail penetration, or overcharging. The fire tests were performed in both an inert, closed pressure vessel and a calorimeter open to ambient. In some tests, cells exploded, in which case, the results were excluded.

The cell SOC impacted total gas volume, gas production rate and composition, mass loss, thermal runaway onset and maximum temperatures. Thermal runaway onset temperatures tended to decrease by 18°C per 25% SOC, while maximum temperatures increased by 90°C per 25% SOC. As SOC increased, the percentage of mass loss also increased. However, mass loss due to

vaporization and gas production was approximately 23% for all SOC. The thermal runaway trigger methods did not increase total gas production; however, more CO and less CO_2 was produced as SOC increased. HF was only detected in the open atmosphere, flaming experiments and the peak HF concentration detected in any test was 4.2 mg/Wh. SO_2, NO, NO_2, HCl, and HCN were analyzed for using FTIR but were note detected or were not quantifiable in any of the tests. A higher SOC was correlated with increased total gas volume and gas production per Ah.

The characteristic, or peak, gas production rate was found to be an average of approximately 130, 79, 73, 12, and 5 L/s for cells at overcharge, 100, 75, 50, and 25% SOC, respectively. Willstrand et al. (2023) concluded that trigger method and SOC both affected gas production rate, mass loss, and maximum temperature of the cell. The trigger method affected gas production rate, mass loss percentage, and maximum temperature. However, it did not seem to affect total gas volume produced or gas composition. Similar to the findings of others, Willstrand et al. (2023) indicated that the large cell format may enhance the effect of the trigger method and specific total gas production. Additionally, the authors found that surrounding pressure and temperature had a low impact on the characterization of thermal runaway.

3.1.38. Yang et al., 2022

In this study, gas production of Li-ion cells during thermal runaway was evaluated in an inert environment. The cells utilized in the tests included NMC cells with capacities of 50 Ah/215 Wh, 115 Ah/495 Wh, and 165 Ah/710 Wh and a total mass of 908, 1815, and 2158 g, respectively. Tests also included LFP cells with a capacity of 196 Ah/715 Wh and a total mass of 3349 g. All tests were of single cells at 100% SOC. The form of the cells (pouch, cylindrical, prismatic) was not identified in the publication. Thermal runaway was initiated via heating plates. The cells were

tested in a sealed pressure chamber purged with nitrogen. Pressure and temperature measurements from within the chamber were used to calculate the volume of gases produced during thermal runaway, according to the ideal gas law. After thermal runaway, and after temperature and pressure reached a steady state, gases from within the chamber were sampled and analyzed with gas chromatography. Thermal runaway critical temperature was defined as the surface temperature of the cell at which the temperature rises sharply, and the cell enters thermal runaway. The cell gas exhaust time was defined as the time from the opening of the cell valve to the end of the pressure relief of the cell. Table 48 presents results from the tests for each cell type and capacity.

Table 48. Vent gas emissions from NMC and LFP cells in an inert environment (Yang et al., 2022)

Cell Type	Cell Capac. [Wh]	TR Critical Temp. [°C]	Mass Loss [%]	Venting Duration [s]	Total Gas Production [mol/Ah]	Percent Volume		Total Gas Production [mol/Ah]	
						CO	CO_2	CO	CO_2
NMC	215	155	38	76	0.079	32.4	35.3	0.023	0.02
NMC	495	121	38	84	0.104	29.6	28.1	0.031	0.029
NMC	710	131	73	62	0.123	60.3	13.0	0.063	0.014
LFP	715	145	23	408	0.053	10.0	26.0	0.005	0.014

The authors noted that the LFP cells had the lowest mass loss percentage and contributed this to the observation that the LFP cells ejected unreacted electrolytes while the NMC cells ejected black solid particles. The large mass loss percentage of the 165 Ah NMC cells was attributed to the ejection of internal coil materials during thermal runaway. HF was not detected in any of tests. The authors contributed this to the inert environment, which has a low water content, which did not allow PF_5 to react and be converted to HF. For CO, it was observed that concentrations increased linearly with capacity.

3.1.39. Yuan et al., 2020

NIOSH conducted 18 tests on cylindrical Li-ion cells with various chemistries to identify gases and concentrations released during thermal runaway. The cells utilized in the testing were LFP cells with a 3.8 Ah/12.2 Wh capacity and a mass of 90.1 g, LTO cells with a 1.3 Ah/3.1 Wh capacity and a mass of 38.6 g, and two types of NMC cells from different manufactures, both with a 3.2 Ah/11.7 Wh capacity and a nominal mass of 45 g. The cells tested via ARC. Thermal runaway was initiated via an electric heater applied to the canister containing the cell. Temperature and pressure within the canister were measured and used to calculate the total quantity of gas produced at ambient temperature and pressure. Gas samples were collected after thermal runaway and analyzed with gas chromatography. The gas analysis was not capable of detecting trace gases.

In identical tests conducted outside the canister, flaming was observed for the NMC cells but not for the LFP cells. Additional tests were also conducted for LFP single, 2-, and 3-cell bundles in a larger canister. Table 49 presents the recorded temperatures and gas production characteristics for the tests.

Table 49. Temperatures and vent gas emissions from cylindrical LFP, LTO, and NMC cells (Yuan et al., 2020)

Cell Type	No. Cells	Cell Capac. [Wh]	Flaming?	TR Onset Temp. [°C]	Max Cell Surface Temp. [°C]	Max Gas Temp. [°C]	Total Gas Production [L]	Percent Volume	
								CO	CO_2
LFP	1	12.2	No	200	399	275	3.29	4.5	25.39
LFP	1	12.2	No	-	263	-	3.79	-	-
LFP	2	12.2	No	-	360	-	8.98	-	-
LFP	3	12.2	No	-	432	-	11.72	-	-
LTO	1	3.1	-	163	305	245	3.20	6.3	37.6
NMC1	1	11.7	Yes	145	835	244	9.77	30.30	13.22
NMC2	1	11.7	Yes	140	998	313	11.08	28.06	19.91

The authors noted that the quantity of gas produced was very similar for the tests of single LFP cells in different size canisters (3.29 L and 3.79 L) and that the total gas quantity scaled proportionally with the number of cells tested. In the single cell test, in the smaller canister, the total volume of gas was released in approximately 15 seconds.

3.1.40. Zhang et al., 2019

Zhang et al. (2019a) forced a 50 Ah, 3.65V, prismatic Li-ion cell at 100% SOC into thermal runaway via an external heater to characterize the settleable particulate matter released from the Li-ion battery. The mass of the cell was 870 g. The cathode material of the cell was mainly NMC type. The anode material was mainly graphite. The cathode current collector was aluminum foil, and the anode current collector was copper foil. The shell material of the cell was an aluminum alloy.

The test was conducted within a chamber purged with nitrogen. An element analyzer was used to detect carbon and sulfur, while fluorine was detected by a tester with a detection limit of 1 mg/kg. ICP-MS was used to detect nonradioactive metals, phosphorus, boron, and silicon with a detection limit of 1 mg/kg. Thermal runaway was found to initiate at 167°C and the temperatures measured in the vent gas jet zone were found to reach a peak of 350°C. Vent gases were sampled at 185ºC (VG185) and then reheated for detection at 90ºC (VG90). The VG90 was analyzed using gas chromatography for CO, CO_2, H_2, and hydrocarbons. GC-MS was used to detect DMC, DEC, and EMC. Ion chromatography was used for HCl.

Vent gases were categorized by the temperature at which they were stable. Seventeen gases were stable at 25ºC (VG25), eight were stable from 25ºC to 90ºC (VG25 to VG90), and six gases were stable from 90ºC to 185ºC (VG90 to VG185). The vent gases have a wide distribution of

boiling points. The majority of VG90 emissions were made of CO, CO_2, and H_2. Hydrocarbons were present, but at a much smaller percentage. The total amount of vent gas was determined to be 3.83 mol. A total of 876, 1031, 2.02, and less than 0.13 mmol of CO_2, CO, Benzene, and HCl were produced, respectively.

Overall, the total mass lost was 248.2 g, approximately 28.53% of the total cell mass. Settleable PM made up 17% of the total emissions. VG25 made up 32.52% and VG90 to VG185 plus dust made up 50.25% of the total emissions. The rest was composed of VG25 to VG90 (0.23%).

3.1.41. Zhang et al., 2022

In an evaluation of the effect of water spray on combustion of Li-ion cells, Zhang et al. (2022) performed thermal runaway tests on NMC cells, during which some had no water spray applied. The cells utilized in the test were cylindrical cells with a capacity of 4 Ah/14.8 Wh and a mass of 68.5 g.

Cells were tested at 0, 50, and 100% SOC in the experiments without an applied water spray. Thermal runaway was initiated via a cylindrical heater adjacent to the cell. Tests were conducted in an explosion proof tank within a combustion chamber equipped with a collection hood and exhaust system. Gas was sampled from the exhaust duct for the duration of the tests and analyzed via FTIR.

The cell at 0% SOC did not achieve thermal runaway but did vent limited amounts of gas. The cells at 50 and 100% SOC underwent flaming combustion. In the 100% SOC test, the cell experienced a violent ejection of material particles, followed by a jet fire. The ejection of solid materials explained the increased mass loss percentage of 41.5% versus 10.8% and 19.4% in the 0 and 50% SOC tests. Table 50 shows the temperature and gas production at various SOCs.

Table 50. Temperature and gas production data from tests of cylindrical NMC cells (Zhang et al., 2022)

SOC [%]	TR Onset Temp. [°C]	Max Cell Surface Temp. [°C]	Mass Loss [%]	Total Gas Production [g]			Peak Gas Production Rate [g/s]		
				CO	CO_2	HF	CO	CO_2	HF
0	NA	366	10.8	-	-	-	-	0.15	-
50	186	775	19.4	0.4	4.2	0.1	.009	0.216	0.003
100	153	800	41.5	1.3	3.0	0.2	.041	0.245	0.004

The authors noted that total CO production increased with increasing SOC while total CO_2 production, and this was attributed to more incomplete combustion in the higher SOC tests.

3.2. UL 9540A BESS Testing

UL 9540A, Test Method for Evaluating Thermal Runaway Fire Propagation in Battery Energy Storage Systems is a standard fire test that assesses thermal runaway, fire, and explosion behavior of a BESS at the cell, module, unit, and installation level. The current edition was published in 2019 by UL and is designated as an American National Standard by the American National Standard Institute (ANSI) and a National Standard of Canada by the Standards Council of Canada (SCC). The tests are performed progressively, i.e., if the BESS meets the requirements at a lower level, e.g., cell level, no further testing is required. The testing data is used to determine the required fire and explosion protection for the BESS installation.

Cell level testing is performed 100% SOC after undergoing a minimum of two charge-discharge cycles at 100% SOC. The cell is placed inside a pressure vessel at atmospheric pressure with less than 1%vol of oxygen. Thermal runaway is initiated via flexible film heaters with a heating rate of 4 to 7 °C/min. The film heaters should cover as much of the cell case as possible. If the film heaters do not initiate thermal runaway, it is acceptable to use alternative heating methods or mechanical or electrical stresses. Cell surface temperature is measured using K-type

thermocouples to determine venting temperature and onset of thermal runaway. GC is used to measure for CO, CO_2, and total hydrocarbons and other gases requested for measurement. A sensor capable of measuring H_2 in excess of 30%vol is used. LFL is determined from the cell gas composition in accordance with ASTM E918.

Module level testing is performed at 100% SOC after undergoing a minimum of two charge-discharge cycles at 100% SOC. The module should be placed on top of a noncombustible surface in the orientation of installation. The test is conducted under a smoke collection hood for gas collection. A sufficient number of cells are forced into thermal runaway to create cell-to-cell propagation within the module. The number of cells required for this condition can vary. Thermal runaway is initiated using the same methods for cell level testing. The chemical HRR is measured using oxygen consumption calorimetry with a paramagnetic oxygen analyzer, NDIR CO_2 and CO sensors, velocity probe, and K-type thermocouple. The velocity probe and thermocouple are also used to determine vent gas velocity and temperature. Vent gas composition is determined via FTIR or an equivalent gas analyzer. FID is used to detect THC content. Smoke release rate is calculated using light transmission measurements from a photo detector.

Unit level testing is conducted with BESS units at maximum operating SOC installed per manufacturer instructions. There is an initiating unit, where thermal runaway is initiated and adjacent target units that represent the installation spacing. Tests are conducted indoors, unless there are controls and certain environmental conditions. BESS units may be tested for indoor, outdoor, or rooftop/garage, residential or non-residential use, or floor-, wall-, or ground-mounted installations. Integral fire suppression systems are allowed, but electronic and software controls (i.e. battery management systems) are not permitted.

For indoor installations, the vent gas composition, THC content, chemical HRR, and smoke release rate measurement methods are the same as those used for module level testing. The gas data is compared to the smallest room installation specified by the manufacturer. Convective HRR is calculated using the relationship between exhaust flow rate, exhaust temperature, and specific heat. For BESS units installed in locations with combustible construction, wall surface temperatures is measured. Schmidt-Boelter heat flux gauges and K-type thermocouples are used for heat flux and temperature measurements. Outdoor and rooftop/garage unit tests do not need to evaluate chemical and convective HRR, gas composition, temperature, and velocity, and smoke release rate if they will only be listed as outdoor use.

Installation level testing assesses fire and explosion mitigation methods for the BESS and is only intended for indoor, non-residential use. The effectiveness of sprinklers and the fire protection plan are assessed. A similar setup to the unit level test initiating and target units is used.

Google Search was utilized to obtain UL 9540A test data for various Li-ion BESS manufacturers and models. These test reports were reviewed for applicable information on equipment composition and specifications, thermal runaway characteristics, fire behavior, and products of combustion. Tests were only included if they were performed at the unit level or if the cell and module level tests were associated with a unit level BESS. Furthermore, units had to be designed for an outdoor, ground-mounted installation. Tests were also excluded if the relevant product information, i.e. cell chemistry, capacity, were not available online.

3.2.1. Enphase IQ Battery 5P

The search found UL 9540A cell (Project Number: 4790222974), module (Project Number 4790222974), and unit (Project Number: 4790527540) level tests performed by UL. The reports

were summarized by Enphase (2023, UL 9540A); the original UL reports were not found. The IQ Battery 5P was certified for both indoor wall- or floor-mounted and outdoor wall- or ground-mounted installations.

The Enphase IQ Battery 5P is a BESS using LFP cell chemistry. It is rated for 5.0 kWh at 76.8V with a power rating of 3.84 kW. The unit is populated with a single module and cannot be connected to other units. The dimensions of the IQ Battery 5P are 0.98 m by 0.55 m by 0.188 m. (Enphase, 2023, IQ Battery 5P).

In the cell level testing, the vent gas composition was reported to be approximately 60.9% H_2, 17.4% CO_2, 6.9% CO, 4.5% methane, and 3.5% ethylene, along with various other hydrocarbons at less than 1% each. The test results showed that thermal runaway was induced in the cell, and the vent gas composition was flammable. As a result, the cell level testing did not pass the performance criteria; thus, module level testing was required.

In the module level testing, the modules were rated at 64.4 Ah at 76.8V and consisted of LFP type battery cells with a total module mass of 35 kg. There were 24 cells in the module connected in series. During the test, only smoke was observed. There were no flames, sparks, or flying debris. There was 937 L of total hydrocarbons, 543 L of CO_2, 47 L of CO, and 163 L of H_2 produced.

In the unit level testing, the initiating unit was populated with one module with the same specifications as those tested previously. Three target units were placed 3 to 6 feet away from the initiating unit. During the test, no external flaming, debris, or reignition were observed. There was 1,394 L of total hydrocarbons, 0.06 L of CO_2, 0.41 L of CO, and 251 L of H_2 produced.

3.2.2. Fortress Power eVault Max

The search found a UL 9540A unit (Project 80128223) level test performed by CCIC-CSA International Certification Co., Ltd. Kunshan Branch and Shanghai Huahui Testing Co., Ltd (Wang et al., 2022) on a Fortress Power eVault Max. The cell level testing (64.280.21.60315.01) was performed by TÜV SÜD New Energy Testing (Guangdong) Co., Ltd; however, the report was not found online. Module level testing was not performed. The eVault Max was tested for indoor floor-mounted installation, which is considered representative of outdoor ground-mounted installation.

The eVault Max uses LFP type cells. The individual unit is rated for 360 Ah at 51.2V (18.5 kWh) but can be scaled up to 370 kWh when combined with other units. The unit dimensions are 0.515 m by 0.515 m by 1.073 m and it has a total weight of 235 kg. The eVault Max holds four modules.

Unit level testing of the eVault Max was performed by CCIC-CSA and Shanghai Huahui Testing on May 18, 2022. No fire detection or suppression is provided in the unit. Film heaters were used to initiate thermal runaway in the second module from the bottom of the rack.

During the test, six cells underwent thermal runaway. Cells vented and released heavy smoke during thermal runaway. No flying debris or deflagration was observed. The test was terminated due to temperatures inside the modules returning to ambient. No flames were observed. Gases measured were O_2, CO, CO_2, H_2, and total hydrocarbons.

3.2.3. Samsung SDI Model PHR0000-004AE3D

The search found UL 9540A unit (Project Number: 4789231760) level tests performed by UL (UL, 2020) on a Samsung SDI Model PHR0000-004AE3D. Summaries of the cell (Project

Number: 4788881139) and module (Project Number: 4788881153) level testing were included in the unit level report. While only one model was tested, the Samsung SDI Model PHR0000-004AE3D is considered representative of the Samsung SDI Model PHR2383-001A. The Samsung PHR0000-004AE3D is designed for outdoor, ground-mounted installations.

The Samsung PHR0000-004AE3D is a metal rack frame without a door. The dimensions are 0.465 m in length, 1.392 m in width, and 2.690 m in height. The Li-ion cells utilized in the Samsung BESS are prismatic cells with a combination of NCA, NMC, and LMO chemistries. Each module has compressed epoxy sheet impregnated with Novec 1230.

In the cell level testing performed by UL, the cells associated with the Samsung PHR0000-004AE3D were Model CS1000RT001A rated for capacity of 100 Ah with a nominal voltage of 3.8V and mass of 2100 grams. The cells were forced into thermal runaway via external temperature ramp heaters. The total cell gas volume was 240 L. The cell vent gas composition was reported to be approximately 39.6% H_2, 25.2% CO_2, 16.6% CO, and 18.7% total hydrocarbons. The test results showed that thermal runaway was induced in the cell, and the vent gas composition was flammable.

In the module level testing performed by UL, the modules were Model EM1762AL001A rated for capacity of 200 Ah with a nominal voltage of 88.32V and mass of 120 kg grams. The modules contained 48 of the previously tested cells in 24S2P format, i.e., 24 cells in series and 2 cells in parallel. Thermal runaway propagated through all cells in the module. External flaming and flying debris were observed; no reignition occurred. CO, CO_2, H_2, and hydrocarbons were not observed pre-flaming, and20 L of CO and 800 L of hydrocarbons were produced after flaming. Peak heat release rate was 1,000 kW.

Unit level testing of the Samsung PHR0000-004AE3D was performed by UL on March 9, 2022. The unit was populated with the same modules as those tested in the module level testing, i.e., Samsung SDI, CS1000RT001A, combination NCA/NMC/LMO prismatic cells. The unit was populated with fourteen EM1762AL001A modules connected in series. The unit was rated for 247.3 kWh at 1236.5V. The equivalent BESS unit Samsung SDI Model PHR2383-001A has 27 modules and is rated for 238.5 kWh with an operating voltage of 1036.8 to 1344.6V. A cell in the third module from the bottom was forced into thermal runaway.

During the test, thermal runaway did not propagate from module-to-module or cell-to-cell. No external flaming or flying debris was observed and the peak heat release rate was below detectable limits. Cell venting was not observed. Approximately 80 L of hydrocarbons were produced, but CO, CO_2, and H_2 levels were below detectable limits. The peak smoke release rate was less than 1 m^2/s and there was 262 m^2 of total smoke released.

3.2.4. Simpliphi BOSS 12 Cabinet

The search found summaries of UL 9540A module and unit level tests provided by Simpliphi Power (Von Burg & Cross, 2022) on a Simpliphi BOSS 12 Cabinet. Additionally, summaries of both tests (UL, 2021, AACD.E527394B; UL, 2021, AACD.E527394C) were found on the UL database. While only one model was tested, the Simpliphi BOSS 12 Cabinet is considered representative of the Simpliphi BOSS 6 Cabinet. The Simpliphi BOSS 12 Cabinet was certified for both indoor and outdoor installation.

The Simpliphi BOSS 12 Cabinet is a BESS contained in a steel enclosure. The BOSS 12 is 0.75 m in length, 0.51 m in width, and 1.93 m in height, weighing 194 kg. The BOSS 6 Cabinet is

0.914 m in length, 0.406 m in width, and 0.914 m in height, weighing 81.64 kg (Simpliphi, BOSS). No fire protection systems are provided in the cabinet.

The BOSS 12 can fit up to twelve modules, while the BOSS 6 can fit up to six modules. The cabinets are compatible with several Simpliphi modules, including the AmpliPHI or PHI 3.8, 3.5, or 3.4 (Simpliphi, BOSS). The Li-ion cells utilized in the BOSS cabinets are cylindrical, LFP cells.

Module level testing was completed for the PHI 3.8 battery module rated for 3.8 kWh at 48V. In this test, the modules consisted of 336, LFP type battery cells, arranged in 16S21P format. The total module mass is 35.5 kg (Simpliphi, Phi). Seven cells were forced into thermal runaway via film heaters. Only cell-to-cell propagation and smoke were observed. There were no flames, sparks, or flying debris. Levels of CO, CO_2, and H_2 were below the detectable limit. Approximately 1 L of hydrocarbons was produced.

Unit level testing of the BOSS 12 involved the same modules as those previously tested, i.e., Phi 3.8, LFP type battery cells. The unit was populated with 12 modules with a total capacity of 45.6 kWh. Thermal runaway was induced through simultaneous heating of 7 cells within a single module via film heaters. The module was the center module located in the row second from the bottom of the unit. During the test, there was no module-to-module propagation, flaming, flying debris, or smoke. Only cell-to-cell propagation was observed. As such, the smoke production rate and peak HRR were both 0. Gas composition was not reported.

3.2.5. Tesla MegaPack 2

The search found UL 9540A cell level tests performed by UL and unit levels tests performed by TÜV SÜD (2022) on a Tesla Megapack 2 (MP2). Other publicly available data included a summary in Bowes and Rogers (2022) of a UL 9540A module level test performed by TÜV SÜD

and summary in Fisher (2022) of unit level testing performed internally by Tesla on an MP2. The MP2 is designed for outdoor ground-mounted installations.

The Tesla Megapack 2 (MP2) is a BESS contained in a steel enclosure. The steel enclosure is 7.25 m in width, 1.63 m in length, and 2.51 m in height with a maximum weight of 38,100 kg. The enclosure is comprised of eight bays separated by metal panels with openings for electrical connections. One of the eight bays is designated as a customer interface bay, six bays are designated as battery module bays, and one bay is designated as a thermal bay.

The battery module bays can each contain up to three modules, and an additional module can be placed in the thermal bay. Each module consists of 112 Li-ion cells. As such, each battery module bay can contain up to three modules for a total of 1,008 cells. Between the six battery module bays and the thermal bay, the MP2 is capable of housing 19 modules for a total of 6,384 Li-ion cells. The Li-ion cells utilized in the MP2 are prismatic LFP cells. When fully loaded, the MP2 has a maximum energy of 2.891 MWh for 2 hours and 3.101 MWh for 4 hours at 100% SOC. The MP2 is equipped with the following fire safety features:

- Integrated battery management system tracking performance, voltage, and SOC with capability to isolate or permanently disconnect affected modules.
- 24/7 remote monitoring, diagnostics, and troubleshooting supported by Tesla's Network Operations Center
- Tesla Site Controller links Tesla operations center with the local Supervisory Control and Data Acquisition System
- Battery module overcurrent protection via single-use fusible links
- Inverter AC and DC protection installed in each module.

- Ground fault protection via DC ground fault detection system and AC circuit breaker with ground-fault trip settings.
- Twenty-two passive overpressure vents installed on the rooftop rated at 12 kPa with sealed battery module bays rated at 30 kPa.
- Twelve sparkers designed to ignite flammable gases early in a thermal runaway event to prevent accumulation of flammable gases and the possibility of an explosion.

In the cell level testing performed by UL, the cells associated with MP2 were prismatic Contemporary Amperex Technology Co., Limited (CATL) Model CB5T0, LFP type cells with $LiPF_6$ electrolyte. The cells had a capacity of 156 Ah with a nominal voltage of 3.2V and mass of 2991 ± 60 grams. The tests applied flexible thin film heaters to force a single cell at 100% SOC into thermal runaway inside a 70-L pressure vessel.

The cell did not achieve flaming combustion, and the total cell gas volume was 97.2 L. On average, the time from the beginning of cell venting to thermal runaway was approximately 780 seconds. The average cell vent temperature was 175°C, and the average thermal runaway temperature was 233°C. For the MP2, the cell vent gas composition was reported to be approximately 47% H_2, 29% CO_2, 11% CO, 6% methane, and 3% ethylene, along with various other hydrocarbons at less than 1% each. Benzene was detected at a concentration of 0.004%. The test results showed that thermal runaway was induced in the cell, and the vent gas composition was flammable.

Results of an MP2 UL 9540A module level test performed on November 17, 2021 were summarized by Bowes and Rogers (2022). In this test, the modules consisted of 112 CATL, LFP type battery cells rated for 156 Ah at 360.64V with a total module mass of 390.3 kg. Thermal

runaway was initiated via film heaters and was achieved at a cell surface temperature of 233 °C. During the test, only smoke was observed. There were no flames, sparks, or flying debris. The total mass loss of the module was 1.0 kg (0.3%). Even though the MP2 module contained the thermal runaway event, the cell vent gas was identified as flammable.

Unit level testing of the MP2 was performed by TÜV Rheinland on March 9, 2022. The unit was populated with the same modules as those tested in MP2 Module Test #1 and Test #2, i.e., CATL, CB5T0, LFP cells. Thermal runaway was induced through simultaneous heating of 6 cells within a single module via film heaters. The initiating cells were located in the center of the module.

During the test, three of the heated cells went into thermal runaway after 1-hour and 9 minutes of heating, and the other three heated cells went into thermal runaway 15 minutes later. Smoke was observed approximately 6 min after the second set of cells went into thermal runaway. Six minutes later, or 27 minutes after the first cell went into thermal runaway, thermal runaway propagated to one additional cell. The heaters were turned off shortly after and thermal runaway did not propagate further. Approximately 15 minutes after the last cell went into thermal runaway, smoke from the unit ceased. No flames were observed outside the MP2 unit. HRR was not measured during the test.

No air or gas samples were taken during the unit level test performed by TÜV Rheinland. However, Tesla performed internal testing, identical to the UL 9540A test, with an MP2 unit during which samples were taken (Fisher, 2022). The thermal runaway observed during the test conducted by Tesla was very similar to the TÜV Rheinland test. Thermal runaway only propagated to one additional cell beyond the six cells heated directly, and no flames were observed (Fisher, 2022).

During this test, gas samples were taken 20 feet upwind and 5 feet downwind. The gas samples were analyzed for 27 metals including: aluminum, arsenic, barium, beryllium, cadmium, calcium, chromium, cobalt, copper, iron, lead, lithium, magnesium, manganese, mercury, molybdenum, nickel, phosphorus, selenium, silver, sodium, tellurium, thallium, titanium, vanadium, yttrium, zinc, and zirconium. No traces of these metals were detected at either location. The gas samples were also analyzed for VOCs and HF. The only VOCs detected were chloromethane and acetone at concentrations of 0.52 ppb and 1.9 ppb, respectively. Mercury was not detected. HF was detected at concentrations of 0.10 and 0.12 ppm, which is significantly below the IDLH value of 30 ppm (Fisher, 2022).

3.3. BESS Incident Case Studies

Previous incidents were reviewed to evaluate the performance of installation level BESS during thermal runaway and fire events. The second goal was to identify historical Li-ion BESS incidents and the common health impact quantification practices. Google Search was utilized to identify literature that included the keywords “lithium-ion BESS thermal runaway incident,” “BESS fire incident,” and “health impact.” These incidents were also reviewed to gather data on environmental and health impacts from actual BESS failure events. An internet search was conducted to identify BESS incidents. The BESS incidents are summarized below in Table 28. The Air Quality Index (AQI)[4] was used to assess environmental impact in some incidents.

[4] A higher AQI is associated with a lesser air quality and has the potential to result in negative health impacts. A range of of 30 is considered a "good" AQI. A range of 151 to 200 is considered an "unhealthy" AQI. For more information on ranges, go to https://www.airnow.gov/aqi/aqi-basics/

Table 51. Historical BESS thermal runaway incidents

Event	Conditions	Evac/Shelter in Place	BESS Specs	Fire Cause & Spread	Air Monitoring	Water Monitoring	Soil Monitoring	Other Monitoring
McMicken (Surprise, AZ) [Hill, 2020]	Apr. 19, 2019 16:54 (explosion at 20:04) 83-94 F	-	LG Chem NMC Rack level runaway (2 MW, 10584 cells)	Cascading thermal runaway in single rack caused explosion	Air dispersion model: minimal impact (emissions not provided)	-	Surface and soil samples near fire site: chemicals of concern were undetectable/similar to control	-
Victoria, AUS [Blum et al., 2022]	July 30, 2021 10:00-16:00 23-35 mph N	Air quality warning (issued before taking air quality measurements)	Tesla 212 MegaPack NMC 300 MW/450 MWh	Liquid coolant caused arcing, wind pushed flames to 2nd MP	EPA (2 mobile stations w/in 2 km): good AQI (0-50) 2 hours post-fire extinguishment	Runoff firewater contained and analyzed, minimal environmental impact	-	-
Valley Center, CA [EPRI, 2023]	Apr. 5, 2022 17:15-20:15 Low 50s to upper 60s No precipitation	-	LG Energy NMC 139 MW/560 MWh	Water cascade over single enclosure triggered by nearby prescribed burn	-	-	-	-
Moss Landing, CA [Grant et al., 2023]	Sept. 20, 2022 01:30-19:00 No wind until 2:30, 3-6 mph E-SE by 4 am No precipitation Upper 50-60 F	Shelter-in-place (issued before taking air quality measurements)	Tesla 256 MegaPack NMC	Single enclosure	EPA tested for fluoride and HF, no PM: good AQI	-	-	-
East Hampton, NY [[New York State, 2023]	May 31, 2023 ~10:00 to ~12:00 59-mid 60s F 6-8 mph SSE	Nearby road closures Railroad branch closure: reopened at 11:20	5 MW/40 MWh	Single enclosure	NYSERDA: air sampling inside BESS done on 6/14-16	DEC determined that groundwater sampling was unnecessary based on soil sampling results	NYSERDA via project developer: Surficial soil and soil 1 foot below surface was collected on 10/4 from area that firewater ranoff to. Background levels collected from west and southeast sides. Concentrations	NYSERDA: Surface sampling inside BESS on 6/14-16 and analyzed for heavy metals. No guidelines or

		(issued before taking air quality measurements)					below commercial NYSDEC Soil Cleanup Objectives or EPA Regional Screening Levels.	reference samples were provided for comparison.
Warwick, NY (Bus Garage on County Road 1A near by Warwick Valley Central Schools) [[New York State, 2023]	June 27 to July 29, 2023 65-68 F 6-12 mph SSE Heavy rain, high wind, power outages	Evacuation of school district: reopening 7/3 (issued before taking air quality measurements) Shelter-in-place (issued before taking air quality measurements)	Powin Energy 6 53' Centipedes LFP	Water leakage into multiple enclosures (no fire or thermal runaway propagation to other units) Alarms were triggered at a 2nd site (Church St) on 6/26 and 6/29 but no fire was detected	Industrial Hygiene Services and Air Quality: Air sampling performed on 6/28 while fire was burning, school located downwind. 0.1-0.5 ppm of CO and VOC outside. School indoor H2S below 0.2 ppm and CO and VOC were not detected. School indoor levels of PM2.5 were lower than outside.	-	-	Industrial Hygiene Services and Air Quality: surface sampling found no hazardous concentrations No lithium, bromide, or fluorine detected on any surface samples
Village of Chaumont, NY [New York State, 2023]	July 27 13:00 to August 1, 2023 11:00 mid 50s-70s F 12-17 mph max wind speeds Rain on July 27 and 30	Shelter-in-place: 1 mi lifted on Jul 27 at 21:00 (issued before taking air quality measurements)	General Electric NMC 4 discrete 5 MW BESS and one 2.5 MW BESS with 22.5 MW solar panel facility	Single enclosure	NYSERDA via OFPC: No readings except for maximum of 4 ppm HCN at the base of the container on 7/27. Low concentrations of CO and VOC (1 ppm) on 7/29. No readings on air monitors on 7/30. CO, VOC, and HCN present only	NYSERDA: groundwater sampling from 11 drinking water wells. Samples were taken 8/4. Two wells had individual PAH levels exceed guidelines, but total PAH was acceptable. No other compounds exceeded acceptable levels. The wells were	NYSERDA: surficial soil and bedrock samples taken at baseline and downwind locations. Samples were taken on 8/24. At SS-4, barium exceeded NYSDEC limits for commercial soil but not for groundwater soil. No other samples exceeded NYSDEC limits. No guidance on some compounds. One sample for SS-9 compounds not present in other sampling sites. Enclosures were removed on 11/14, samples directly beneath the	-

					at the base of the enclosures on 8/1.	resampled on 12/4, results have not been released.	enclosures were taken. Results have not been released.	
Valley Center, CA [Murray, 2023]	Sept. 18, 2023 17:15 6-7 mph W Upper 60s-70 F	Evacuation: 0.25 mi from 17:45 to 20:30 (issued before taking air quality measurements) Shelter-in-place: 0.5 mi (issued before taking air quality measurements)	LG Energy NMC 139 MW/560 MWh	Single enclosure	San Diego County: good air quality	San Diego County: good water quality	-	-
Bouldercombe (Queensland, AUS) [Hines & McGhee, 2023] [Peacock, 2023]	Sept. 26, 2023 19:45 6-10 mph average N-NW	Shelter-in-place	Tesla 40 MegaPack 2 50 MW/100 MWh LFP	Failure in power electronics interface (grid-side fault) propagated through modules in single enclosure	No fixed stations nearby FD monitoring showed good AQI	-	-	-

The organizations responsible for air, soil, and water monitoring stated that there was little to no human and environmental health impact from the reviewed BESS incidents. The conclusions, however, must be put in context with some gaps in the testing methods. The McMicken, Victoria, Valley Center, and East Hampton incidents had no real-time air quality monitoring during the fire. Measurements were taken after the incident when the plume had already dispersed, making it difficult to ascertain the public impact during the event when gas production was highest. There was no water or soil quality monitoring for several incidents as well. When testing for environmental impact, some testing did not evaluate pollutants such as HF or other halogenated compounds, hydrocarbons, PAHs, per- and polyfluoroalkyl substances (PFAS), semi-volatile organic compounds (SVOC), or VOCs. Several incidents only analyzed AQI, which does not consider the impact of the aforementioned compounds. Furthermore, in some cases, it is unknown when and where monitoring was performed. In other cases, monitoring was performed well after the incident (e.g., East Hampton incident) with no consideration for weather-related impacts like precipitation that could dilute original contaminant concentrations in the soil. The lack of significant findings could indicate that either no significant contamination occurred or that contaminants were water soluble, biodegradable, and did not persist over time. As the monitoring results are inconclusive, this study aims to develop a methodology to better characterize the pollutant concentrations most relevant to human health and environmental impact.

3.4. Model Program Selection

The third goal was to identify modeling programs and practices that could be used to characterize Li-ion thermal runaway health impacts. Google Scholar was utilized to identify literature that included the keywords “lithium-ion thermal runaway,” “fire modeling,” and “plume

dispersion modeling." Plume dispersion modeling was utilized to demonstrate how human health impacts could be characterized for a simulated thermal runaway event in an outdoor BESS installation. The modeling considered a thermal runaway event in a single unit that propagates without flaming, as well as a thermal runaway in a single unit that propagates with flaming. The selected scenarios were based upon failure modes reported in testing and real incidents. The objective of the modeling was to determine the concentrations of toxic gases contained in the fire plume at varying distances from the fire origin. The concentrations were compared against human health exposure limits to assess the potential impact on the surrounding population in the modeled scenario, and demonstrate a methodology that can be used in hazard evaluations

The plume dispersion modeling program had to be capable of modeling both a fire plume and gas release. The program needed to simulate combustion from a point source over a short time scale (i.e. minutes) using inputs of emission yields and mass loss rate. In addition, the program had to model plume development close to the compartment and hundreds of meters downwind to capture both the near and far-field health impacts. Table 52 provides a list of modeling programs assessed and their capabilities. Models that were developed solely for wildfire propagation, with no consideration for smoke plume development, were excluded. Based on the requirements for modeling, FDS was chosen. FDS is a CFD model developed by the National Institute of Standards and Technology (NIST) fire modeling. It has been used by others to model BESS thermal runaway events (Franqueville et al., 2023) and is validated for plume dispersion (McGratten et al., 2024a; McGratten et al., 2024b). While there are modeling programs that are able to model larger domains, the fire modeling was restricted to certain types of fires and did not allow for 3D modeling of the BESS unit. Pyrosim, a program developed by Thunderhead Engineering, was

utilized as an interface for FDS during the modeling process. Smokeview, in conjunction with FDS and Pyrosim, was used to visualize the results.

Table 52. Fire and plume dispersion modeling programs and their specifications

Model Name	Domain (Cell Size)	Developed for?	Physics	Plume Modeling	Fire Modeling	Toxic Gas Inputs
FDS	m- ~1-2 km, computationally expensive at km (cm-m, multi-mesh)	Multiple plume and combustion scenarios, chemistry only for CO, may not predict unsteady dispersion well	TKE+LES (CFD)	Yes	Yes	Species mass loss rate
FLARE/ BUOYANT	Km (Determined automatically by CORINE, 100s m)	Forest or pool fire plumes, no phase changes in plume, no pollution, developed with HARMONIE (region locked to Finland)	Simple physics	Yes, can't handle vertical profiles well	Yes, simple	No
HIGRAD/ FIRETEC	~1 km, 100s ft to 10s mi. Computationally expensive (cm-m)	Wildfire- flame front, combustion	LES (CFD)	Yes	Yes, wildfire specific fuel combustion	No
WRF-SFIRE-CHEM	km or larger, landscape scale. Limited to 10 m above ground (10s m, multi-mesh)	Wildfire- atmospheric physics/chemistry, smoke & gaseous product transport, focus on fire propagation. CHEM for chemistry of emissions and yields. Dependent on WRF data	Eulerian Simplified combustion, focused on fireline/ atmosphere	Yes	Yes, Rothermel fire spread w/ prescribed fuel (can't input own fuel). No ignition point/fire history	No, emissions depend on pre-loaded fuel class
WFDS	~1 km, computationally expensive beyond 4 km (cm-m)	Wildfire- flame front, combustion, use WFDS-LS for fireline propagation	LES (CFD)	Yes	Yes	No, emissions depend on pre-loaded fuel class
ForeFire	-	Wildfire propagation, validated for large industrial fire	Simplified combustion focused on fireline propagation	No	Yes	No

4. Risk Assessment Methodology

4.1. Thermal Runaway and Plume Dispersion Modeling

The modeled scenario involved a 3 MWh, outdoor BESS unit undergoing thermal runaway in a rural area with flat terrain and low-lying vegetation. It was assumed that there were no surrounding buildings or complex terrain. Non-flaming and flaming thermal runaway scenarios were modeled with both LFP and NMC cell chemistry. No fire suppression was modeled. A bounding analysis on wind and temperature was conducted to determine the impact of meteorological conditions on plume dispersion. No precipitation or variation in relative humidity was modeled. In addition, 0 m/s wind scenarios were run with an ambient temperature of 22°C to provide the baseline toxic gas concentrations in the plume. While these conditions do not account for all possible factors, they serve as a basic scenario to identify relevant factors and develop a modeling approach for outdoor, large-scale, Li-ion BESS thermal runaway incidents. For a given project, the modeled scenario should be based on reasonably expected site conditions and BESS failure scenarios.

The enclosure dimensions, ventilation, and module arrangement of the Tesla MP2 was used as a basis for the configuration of the modeled BESS unit because configuration data was publicly available. Other large-scale BESS models, such as the LG Chem Model JP3, GE Energy RSU-4000, and Powin Energy Smart enclosure have similar dimensions and capacity. The MP2 configuration was also utilized, because it includes up to 57 modules with over 6,000 prismatic cells; based upon the review of publicly available UL 9540A data, the MP2 configuration represents the greatest number of modules (and cells) expected within a single unit, i.e., a worst-

case scenario. Only the configuration of the MP2 was utilized for modeling purposes; the modeled fire scenarios (including HRR and gas production) were not specific to an MP2 fire and were derived from a compilation of data sets as discussed in Section 4.2. Modeling was performed for all simulations using the MP2 unit layout. Figure 1, Figure 2, and Figure 3 present the isometric and front views of the BESS unit modeled in Pyrosim. The front wall was hidden to show the inside structure and module layout of the unit. The red rectangles are the burner vents modeling combustion. The green rectangles are the supply vents modeling toxic gas release. In the non-flaming simulations, the combustion vents were removed, and only three gas burner vents were left in place.

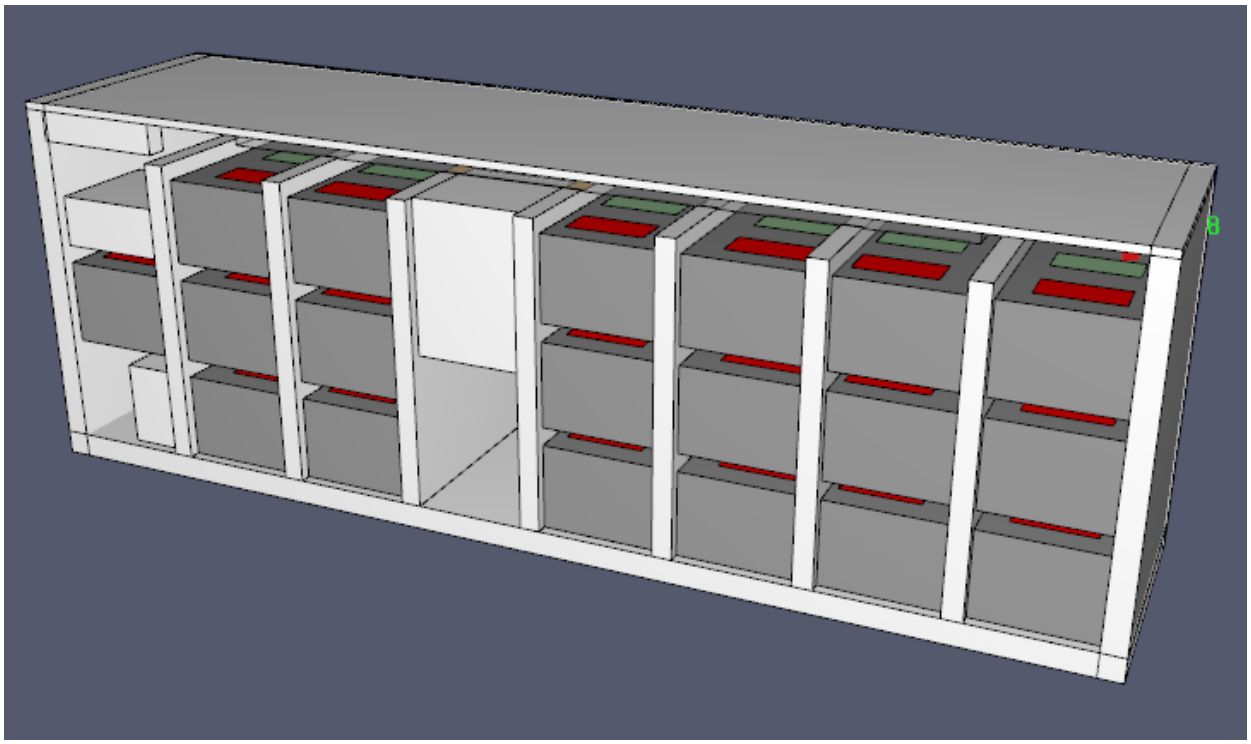

Figure 1. Isometric view of the Pyrosim model of the flaming BESS unit

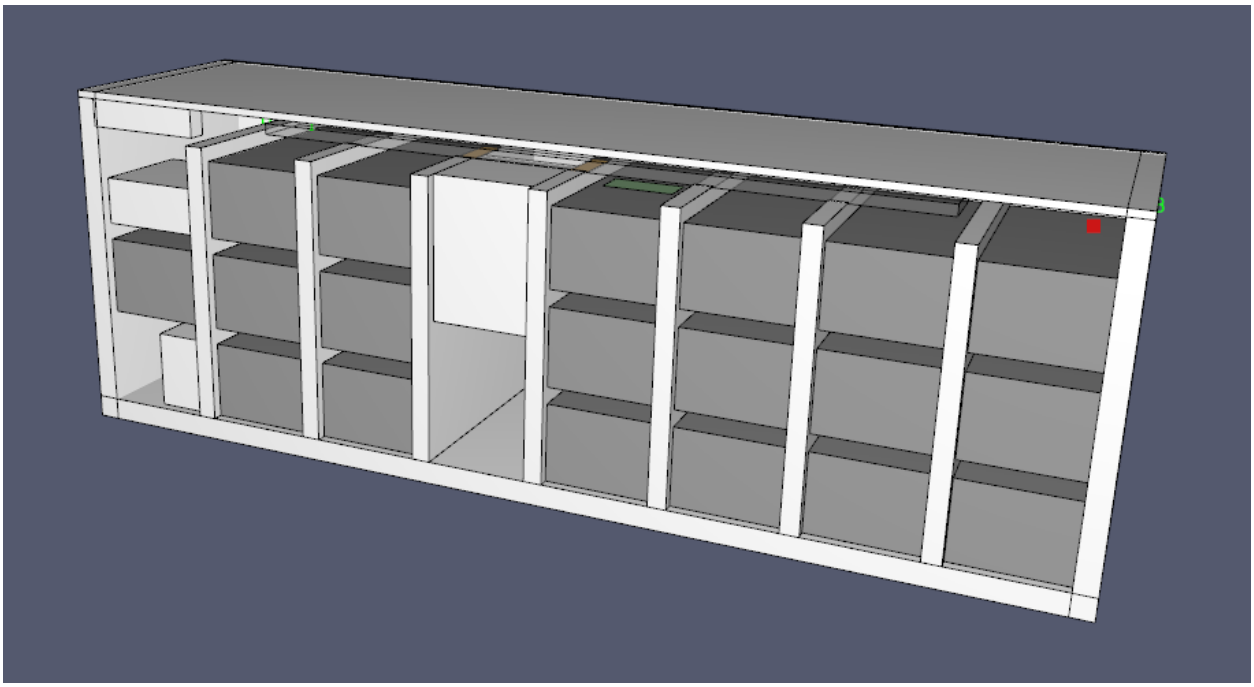

Figure 2. Isometric view of the Pyrosim model of the non-flaming BESS unit

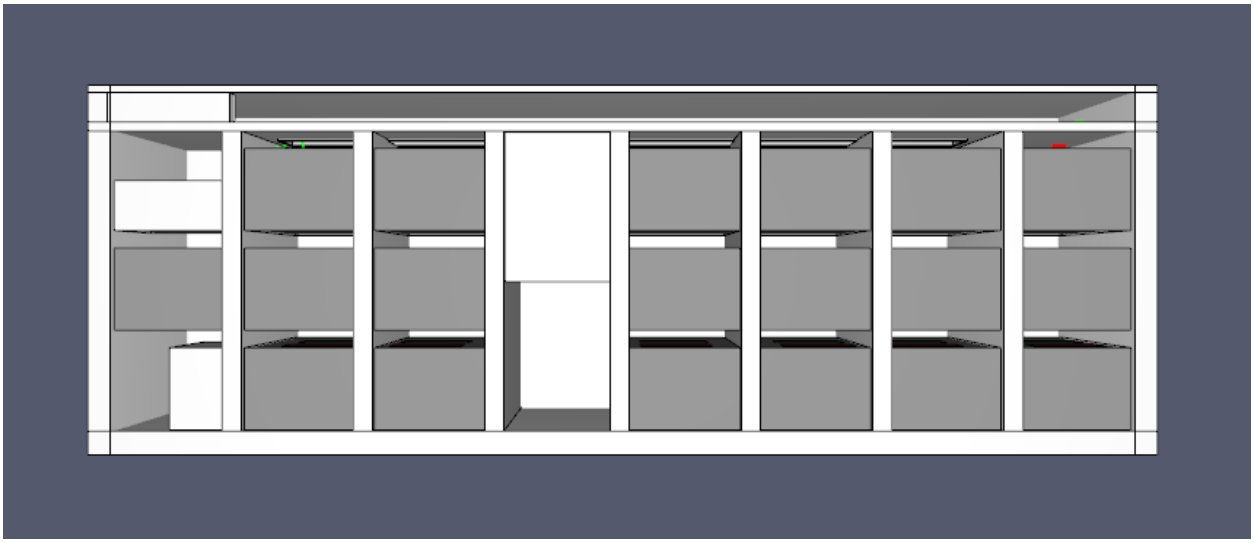

Figure 3. Front view of the Pyrosim model of the BESS unit

User defined inputs in the FDS model included computational domain, ambient temperature, wind velocity, MLR, fuel, gas emission factors, and gas temperature. Modeling was limited to several hundred meters downwind of the BESS unit due to the computational expense of running

a larger-scale simulation. The width of the computational domain was 32 m for all scenarios to encompass the full width of the plume. Iterations of the model were run to determine where HF fell below community exposure limits, and this was used to define the length and height of the domain. The computational domain dimension are provided in Table 53.

Table 53. FDS computational domain dimensions

Thermal Runaway Conditions	Width [m]	Length [m]	Height [m]
Flaming	32	100	43
Non-flaming		200	26

Cells containing the BESS unit were set to 0.125 m, and gradually expanded to 0.25 m and 0.5 m cells. All cells were uniform. Figure 4 and Figure 5 show the cell size expansion around the modeled BESS unit from the X-Y and Y-Z plane in Smokeview.

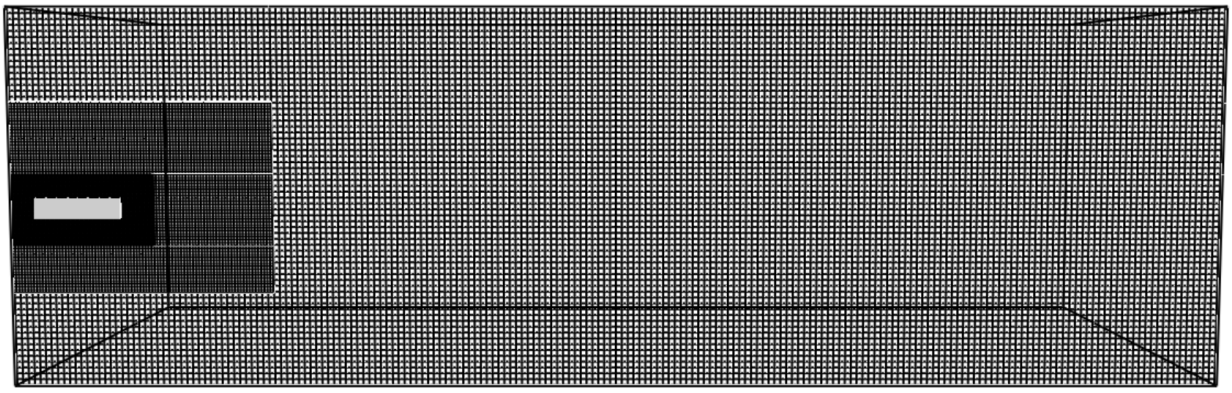

Figure 4. FDS cell sizes in the X-Y plane

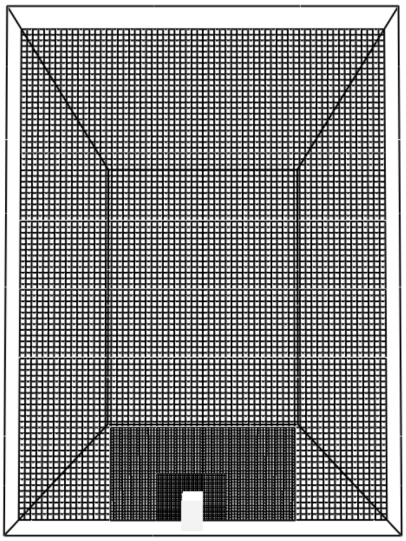

Figure 5. FDS cell sizes in the Y-Z plane

For the large eddy simulation code used in FDS, the grid can be resolved by dividing the characteristic length by cell size to find the number of cells along the characteristic length. There should be at least 10 cells along the characteristic length for good resolution (Trouvé, 2023). For the flaming thermal runaway, the fire was contained to the 0.125 m and 0.25 m cells. The length of the fire was approximately the length of the BESS unit, so the characteristic length scale is approximately 7 meters. At the largest cell size (0.25 m), there are 28 cells, i.e., greater than 10 cells, along the length of the fire which provides an adequate grid resolution.

The model simulations were run using cloud computing. Each simulation required 32 CPU cores with 1 Gb of RAM per CPU. The flaming simulations took approximately 6 to 13 hours to run, while the non-flaming simulations took approximately 3 to 16 hours. The total computational time ranged from 192 to 416 hours for the flaming simulations and 96 to 512 hours for the non-flaming simulations.

4.2. Gas Production and Mass Loss Rate

To calculate gas concentrations, the release rates at the source must first be identified. To quantify the release of specific species during combustion, the MLR, which is dependent on HRR, must be estimated. Data from the literature review was used to estimate HRR values, and subsequently MLR values, for the flaming model scenarios. An average, steady state MLR was modeled for each scenario and gas production rates were determined based on yield data obtained from the literature review. In the case of non-flaming thermal runway, gas production is a result of thermal decomposition[5] of the cell's internal chemistry, not combustion. HRR describes the heat energy released during combustion and hence is not useful in predicting the MLR of a material undergoing thermal decomposition. As such, a different approach was required to predict MLR in the non-flaming scenarios, and in these cases, the MLR was estimated based on total gas volume production.

An average, steady state gas volume release was modeled for each scenario and gas production rates for specific species were determined based on percentage gas composition data obtained from the literature review. It was noted that average gas production rates do not capture peak gas production values, and as such, the peak values would not be considered in the health impact evaluation. However, the data sets showed that peak concentrations typically lasted a few seconds. Community exposure limits are evaluated on the magnitude of minutes to hours. As such, use of

[5] Thermal decomposition involves the breakdown of a compound into smaller constituents in the presence of heat alone. Combustion involves a reaction between a fuel and oxygen that produces heat and light, e.g., a flame.

the average gas production rates was considered a reasonable approach. Calculations for the average gas production rates in non-flaming and flaming scenarios are described below.

4.2.1. Non-Flaming Scenario

For the non-flaming simulations, calculations were performed assuming consumption of only one bay or nine modules in the BESS unit. The total capacity of the consumed modules was 0.49 MWh. Thermal runaway propagation is dependent on heat transfer between adjacent modules (Barowy et al., 2021). Huang et al. (2020) showed that heat transfer in Li-ion battery modules is primarily driven by radiation and conduction through the connections between Li-ion cells. In a non-flaming scenario, modules will release less heat due to the lack of flames. In the modeled configuration, the bays are separated by steel walls, which would further hinder thermal runaway propagation between bays. It is expected that the other bays would not experience enough heat transfer to initiate thermal runaway, hence, the modeled scenario is considered to be worst case.

Based on the review of available literature, non-flaming thermal runaway does not produce HRR as there is no oxygen consumption from the flame (Huang et al., 2021). To model mass loss from the cell off-gassing, data on total gas production normalized by capacity in Wh was used to estimate the total volume of gas produced from a single bay of cells. To estimate the gas release rate (L/s) for a non-flaming scenario, the predicted total gas production in L from the bay was divided across an estimated event duration.

Data on total gas production for non-flaming thermal runaway was found from the studies reviewed in Section 3.1 and UL 9540A data reviewed in Section 3.2. If capacity was not provided, a typical nominal voltage of 3.2 V for LFP cells and 3.6 V for NMC cells was assumed and used

to calculate capacity from current. Sturk et al. (2019) measured HF quantities via both FTIR and gas-wash bottles. The gas-wash bottles were found to report approximately twice the amounts of HF than FTIR, due to treating all soluble fluorinated species as HF. As such, Sturk et al. (2019) suggested the gas-wash bottle method overpredicts HF quantities, however, to be conservative, the average of the values measured from both methods, when provided by the study, are indicated in the tables below. Table 54 provides the total gas production for LFP cells.

Table 54. Total gas volume normalized by cell capacity for LFP cells

Source	Cell Geometry	Total Gas Production [L]	Cell Capacity [Wh]	Total Gas Production [L/Wh]
Archibald (2021)	Cylindrical	33.5	284	0.12
DNV (2019)	Cylindrical	10.0	8	1.25
DNV (2019)	Cylindrical	7.0	8	0.88
DNV (2019)	Cylindrical	21.0	8	2.63
DNV (2019)	Cylindrical	5.0	4.8	1.04
DNV (2019)	Cylindrical	5.0	4.8	1.04
Golubkov (2014)	Cylindrical	1.1	4	0.32
Golubkov (2015)	Cylindrical	1.2	4	0.35
Golubkov (2015)	Cylindrical	0.7	4	0.20
Golubkov (2015)	Cylindrical	0.7	4	0.20
Golubkov (2015)	Cylindrical	0.9	4	0.26
Golubkov (2015)	Cylindrical	0.7	4	0.20
Golubkov (2015)	Cylindrical	1.4	4	0.39
Golubkov (2015)	Cylindrical	1.3	4	0.37
MP2 UL 9540A (2022)	Prismatic	97.2	502	0.19
Sturk (2019)	Pouch	50.0	115.5	0.43
Yang (2022)	Prismatic	232.7	715	0.33
Yuan (2020)	Cylindrical	3.3	12.2	0.27
Yuan (2020)	Cylindrical	3.8	12.2	0.31
Yuan (2020)	Cylindrical	9.0	24.4	0.37
Yuan (2020)	Cylindrical	11.7	36.6	0.32

The average total gas production normalized by capacity for LFP cells was 0.55 L/Wh. This number was multiplied by the capacity of the involved modules for a total LFP gas production of 269,000 L.

Table 55 provides the total gas production for NMC cells.

Table 55. Total gas volume normalized by cell capacity for NMC cells

Source	Cell Geometry	Total Gas Production [L]	Cell Capacity [Wh]	Total Gas Production [L/Wh]
Amano (2023)[1]	Pouch	1.0	9.25	0.11
Amano (2023)[1]	Pouch	3.0	9.25	0.32
Amano (2023)[1]	Pouch	3.0	9.25	0.32
Archibald (2021)	Prismatic	221.6	346	0.64
Bordes (2022)	Pouch	37.7	70	0.54
DNV (2019)	Pouch	458.0	226.8	2.02
DNV (2019)	Pouch	223.0	226.8	0.98
Essl (2020a)	Pouch	57.0	156	0.37
Essl (2020b)	Pouch	94.0	216	0.44
Essl (2020b)	Pouch	167.0	216	0.77
Essl (2020b)	Pouch	103.0	216	0.48
Essl (2020b)	Prismatic	94.0	216	0.44
Essl (2020b)	Prismatic	159.0	216	0.74
Essl (2020b)	Prismatic	106.0	216	0.49
Golubkov (2014)	Cylindrical	5.9	10	0.60
Golubkov (2014)	Cylindrical	3.3	6	0.59
Nedjalkov (2016)	Pouch	200.0	172	1.16
Nedjalkov (2016)	Pouch	85.8	172	0.47
Sturk (2019)	Pouch	1500.0	287	5.23
Willstrand (2023)[1]	Prismatic	409.0	565.2	0.72
Willstrand (2023)[1]	Prismatic	332.4	565.2	0.59
Willstrand (2023)[1]	Prismatic	221.4	565.2	0.39
Willstrand (2023)[1]	Prismatic	113.0	565.2	0.20
Willstrand (2023)	Prismatic	55.0	565.2	0.10
Yang (2022)	Prismatic	88.5	215	0.41
Yang (2022)	Prismatic	267.9	495	0.54
Yang (2022)	Prismatic	454.6	710	0.64

1. Average total gas production over tests conducted

The average total gas production normalized by capacity for NMC cells was 0.76 L/Wh. This number was multiplied by the capacity of the consumed modules for a total NMC gas production of 372,000 L.

Table 56 presents the times for peak gas venting to occur in large capacity (>100 Wh) LFP and NMC cells identified from the literature review. When finding average peak gas venting duration, only large capacity cells were considered as they represent a worst-case scenario cell size used in large scale BESS units. The cell capacity is expected to impact the duration of venting due to the higher gas production, so smaller cells were excluded.

Table 56. Peak cell venting duration for LFP and NMC large capacity cells (>100 Wh)

Source	Cell Chemistry	Cell Geometry	Peak Venting Time [s]
Archibald (2021)	NMC	Prismatic	3.0
Essl et al. (2020a)	NMC/LMO	Pouch	4.0
Essl et al. (2020b)	NMC	Pouch	3.5
Essl et al. (2020b)	NMC	Pouch	5.2
Essl et al. (2020b)	NMC	Pouch	3.1
Essl et al. (2020b)	NMC	Prismatic	2.0
Essl et al. (2020b)	NMC	Prismatic	1.1
Essl et al. (2020b)	NMC	Prismatic	11.5
Huang et al (2021)	LFP	Prismatic	229.8
Sturk et al (2019)	NMC	Pouch	21
Sturk et al (2019)	LFP	Pouch	300

Based on these values, the average peak venting time is 6 seconds for NMC cells and 265 seconds for LFP cells. The large difference in vent time is consistent with general findings of the literature review that show NMC cells experience a more violent failure at thermal runaway whereas LFP cells vent steadily over a longer duration.

To estimate cell propagation within the modules for a NMC cell scenario, it was assumed that, due to the very short vent duration, only one cell vents simultaneously. This results in a total event duration of 101 minutes for a single bay. To bound the analysis of this scenario, event durations of 0.5 hours and 2 hours were used. For an LFP cell scenario, assuming one cell venting at a time would result in a total event duration of 74 hours. This is consistent with historical data for non-flaming BESS unit incidents which has shown that these events can continue for multiple days. For example, the Powin Energy BESS fire in Melba, ID continued for over 3 days and the Powin Centipede BESS fire in Warwick continued for at least 2 days. However, modeling of a scenario for this duration was expected to produce negligible results regarding health impacts. In the longer incident durations, the MLR and gas concentrations would be lower compared to the shorter incident durations. As such, incidents lasting multiple days are unlikely to represent the worst-case scenarios. Therefore, to gauge the impact of more catastrophic thermal runaway events, it was assumed that 10% of a module's cells vent simultaneously, or 11.2 cells, rounded up to 12 cells. This results in a total event duration of 6.2 hours for a single bay. To bound the analysis of this scenario, event durations of 6 hours and 12 hours were used. The resulting average gas release rates are provided in Table 57.

Table 57. Non-flaming average gas production rates for various durations

Cell Chemistry	Duration [hr]	Average Gas Production Rate [L/s]
LFP	6	12
LFP	12	6
NMC	0.5	207
NMC	2	52

4.2.2. Flaming Scenario

Unlike the non-flaming simulations, the calculations for the flaming simulations were performed under the assumption that all cells in the BESS unit would undergo thermal runaway. This scenario is based on the historical handling of flaming BESS thermal runaway events, as indicated in Section 3.3. It is common practice to let the BESS unit burn out, resulting in full consumption of all modules. Additionally, a flaming scenario is more likely to initiate thermal runaway propagation to the other modules due to convective and radiative heat transfer from the flames. Thus, it is expected that the full 3 MWh capacity of the modeled unit would be consumed in a flaming scenario.

To estimate the HRR for a flaming scenario, the predicted total heat released (THR) from the unit was divided across an estimated event duration. Data on THR normalized by capacity (Wh) for flaming thermal runaway was pulled from the studies reviewed in Section 3.1. If only THR was provided, it was normalized by the provided capacity or a nominal capacity calculated using a typical nominal voltage of 3.2 V for LFP cells and 3.6 V for NMC cells.

Bordes et al. (2022) indicated that 2.5 MJ was contributed to their reported THR values by combustion of plastic components; this quantity was subtracted from the THR values reported by the authors. Ditch & Zeng (2020) indicated that an additional 5% should be added to their reported THR as the fire was extinguished before full mass consumption; this quantity was added to the values reported by the authors.

Table 58 and Table 59 provide the normalized THR for LFP and NMC cells.

Table 58. THR normalized by capacity for LFP cells

Source	Cell Geometry	THR [MJ]	Cell Capacity [Wh]	THR [kJ/Wh]
Andersson (2013)	Pouch	6.826	112	60.95
Andersson (2013)	Pouch	6.645	112	59.33
Andersson (2013)	Pouch	7.13	112	63.66
Andersson (2013)	Pouch	7.356	112	65.68
Andersson (2013)	Pouch	7.46	112	66.61
Andersson (2013)	Cylindrical	2.409	92	26.18
Bordes (2022)	Pouch	8	210	38.10
Bordes (2022)	Pouch	10.5	210	50.00
Ditch & Zeng (2020)	Prismatic	143	5200	27.50
Ditch & Zeng (2020)	Prismatic	1209.6	31200	38.77
Ditch & Zeng (2020)	Prismatic	3810	83600	45.57
Larsson (2016)	Cylindrical	2.766	92	30.07
Larsson (2016)	Cylindrical	2.502	92	27.20
Larsson (2016)	Cylindrical	6.605	132	50.04
Larsson (2017)[1]	Pouch	-	128	46.90
Larsson (2017)[1]	Pouch	-	112	69.50
Larsson (2017)[1]	Pouch	-	112	70.50
Larsson (2017)[1]	Cylindrical	-	92	30.00
Larsson (2017)[1]	Cylindrical	-	132	50.00
Liu (2020)	Prismatic	1.749	70.4	24.84
Liu (2020)	Prismatic	2.034	70.4	28.89
Liu (2020)	Prismatic	2.40577	70.4	34.17
Liu (2020)	Prismatic	1.21492	70.4	17.26
Liu (2021)	Pouch	12.839	778	16.50
Liu (2021)	Pouch	14.101	778	18.12
Liu (2021)	Pouch	19.531	778	25.10
Meng (2020)	Prismatic	2.116	81	26.12
Meng (2020)	Prismatic	1.855	81	22.90
Meng (2020)	Prismatic	1.317	81	16.26
Peng (2020)	Pouch	6.66	219	30.41
Peng (2020)	Pouch	6.388	219	29.17
Peng (2020)	Pouch	5.644	219	25.77
Peng (2020)	Pouch	4.165	219	19.02
Sturk (2015)	Pouch	-	Varied	50.00
Sturk (2015)	Pouch	-	Varied	61.56
Sturk (2015)	Pouch	-	Varied	62.81
Sturk (2015)	Pouch	-	Varied	60.94
Sturk (2015)	Pouch	-	Varied	68.13

1. Average THR over tests conducted

Table 59. THR normalized by capacity for NMC cells

Source	Cell Geometry	THR [MJ]	Cell Capacity [Wh]	THR [kJ/Wh]
Bordes (2022)	Pouch	33.5	210	38.10
Bordes (2022)	Pouch	10.0	210	50.00
Quant (2023)	Unk	7.0	50000	16.00
Sturk (2015)	Pouch	21.0	Varied	30.00
Sturk (2015)	Pouch	5.0	Varied	28.33
Sturk (2015)	Pouch	5.0	Varied	29.44
Sturk (2015)	Pouch	1.1	Varied	28.61
Sturk (2015)	Pouch	1.2	Varied	31.67
Willstrand (2020)	Pouch	0.7	Varied	48.50

The THR normalized capacity has a wide range of values. To account for uncertainty and ensure that the mass loss rate is conservative, the average and positive standard deviation were calculated and added together to get the THR value. The normalized THR for LFP cells is 58 kJ/Wh and 43 kJ/Wh for NMC cells. The normalized THR was then multiplied by the maximum capacity of the BESS unit to find a THR of 180,000 MJ for LFP cells and 135,000 MJ for NMC cells.

Barowy et al. (2021) found that in full-scale testing on a BESS rack with NCA cells, it took approximately 20 minutes for flaming thermal runaway to propagate from the initiating rack to an adjacent rack. Thermal runaway then propagated from the first module in the adjacent bay to the top module over a period of 40 minutes. In total, it took 2.5 hours for thermal runaway to propagate to all modules. Assuming a fire/thermal runaway starts in a center bay of the modeled unit, and assuming a similar horizontal propagation rate of 20 minutes from bay-to-bay, it would take at least 80 minutes for the event to propagate to modules in all 8 bays. Then, assuming the same vertical propagation time (40 minutes) for the entire rack of modules in a bay, the total time for all

modules in the bay to become involved would be 120 minutes. This is still less than the total time for the test run by Barowy et al. (2021), despite the rack in the test only having a total capacity 58 kWh, compared to the 3 MWh capacity on the modeled unit. Additionally, Ditch and Zeng (2020) found that flaming thermal runaway continued for 98 minutes and 160 minutes in BESS racks with LFP cells and LNO/LMO cells, respectively. Applying this vertical propagation time in conjunction with the horizontal propagation time of Barowy et al. (2021) produces total event times of 3 hours and 4 hours. Therefore, use of a 2-hour duration for a flaming thermal runaway event was considered conservative, as the shorter the event duration the greater the MLR and gas production.

This is supported by the historical incident data which shows that for incidents where flaming combustion occurred, in both NMC and LFP cells, the minimum event duration was 2-hours. This occurred in the East Hampton incident, where the fire was contained by the enclosure's sprinkler system and therefore, it is expected the fire would have burned even longer if suppression had not been applied. The Moss Landing and Victoria fires continued for durations of approximately 7.5 hours and 6 hours, respectively, and these events involved NMC cells. Therefore, to account for a range of incident durations, flaming thermal runaway scenarios of 2, 4, and 6 hours were run. Despite evidence from the literature review that LFP cells experience longer flaming thermal runaway durations (Sturk, 2015), this was in the case of small modules (up to 10 cells). It is expected that once a full BESS unit becomes fully involved in a fire, the differences in propagation rates due to cell chemistry become negligible because of the high heat conditions and rapid flame spread. As such, the same event durations were utilized for both NMC and LFP flaming scenarios. The resulting average MLRs are provided in Table 60.

Table 60. Flaming average MLR for various durations

Cell Chemistry	Duration [hr]	Average MLR [g/s]
LFP	2	1444
LFP	4	722
LFP	6	481
NMC	2	1082
NMC	6	541
NMC	4	361

4.3. Toxic Gas Emissions

It is well understood that nearly all fuels, when burned, release chemicals and that the released constituents, if at a sufficient dose, can be harmful to human health. The types and concentrations of chemicals, i.e., emissions, are dictated by the chemical composition of the fuel and the burning conditions. It is not surprising that combustion of Li-ion batteries results in the release of chemicals with the same elements found in the fuel, e.g., fluoride; the conservation of mass necessitates that the same number of carbons, hydrogens, fluorides, etc. involved in the reaction will also be present as products of combustion.

The literature review identified the following toxic gases produced during Li-ion thermal runaway: benzene, CO, CO_2, HBr, HCl, HCN, HF, NH_3, NO_2, and SO_2. Data on constituent gas yields was pulled from the studies reviewed in Section 3.1. The yield quantification methods used were a) species mass produced normalized by mass consumed in mg/g, b) percent gas volume composition, and c) species mass produced normalized by cell capacity in mg/Wh. The full list of yields can be found in Appendix 7.1. Model input yields were calculated by finding the average and positive standard deviation of the data points, then adding them together. If only one non-zero data point, e.g. yield was not found to be 0, was found for a constituent, it was excluded from

review. For species with multiple non-zero data points and data points where the yield was 0, the 0 values were included when calculating the average and standard deviation.

4.3.1. Non-Flaming Scenario

Mass production rate for each constituent was calculated utilizing the percent volume composition of gas constituents and the average total gas production rate found in Section 4.2.1. The percent volume for specific constituents, multiplied by the average total gas production rate, then, was converted to mass using the ideal gas law under STP or the provided reference temperature. STP was used when the gases were quantified after they had cooled to ambient temperature. Where percent volume composition was not available for a gas constituent, species mass normalized by capacity was used to determine the total expected mass release of the constituent over the duration of the event. The total quantity was then divided by event duration to estimate an average MLR. Percent volume was prioritized over mass normalized by capacity, as it was applied as a ratio of the average total gas production rate; mass normalized by capacity has the potential to under- or overestimate the constituent to total volume ratio. Any chemicals that only had one non-zero data point were excluded from the evaluation. Table 61 and Table 62 provide the species yields and mass production rates for the non-flaming simulations.

Table 61. Non-flaming species yields and mass production rates for LFP cells

Species	Yield			Mass Production Rate [g/s]	
	%vol	mg/g	mg/Wh	6 hr	12 hr
Benzene	7.5	-	-	3.26	1.63
CO	14.6	-	-	2.28	1.14
CO_2	66.7	-	-	16.34	8.17
HCl	1.9	-	-	0.39	0.19
HCN	0.5	-	-	0.08	0.04
HF	2.7	-	-	0.30	0.15
NO_2	7.9	-	-	2.02	1.01

Table 62. Non-flaming species yields and mass production rates for NMC cells

Species	Yield			Mass Production Rate [g/s]	
	%vol	mg/g	mg/Wh	0.5	2
Benzene	4.1	-	-	29.56	7.39
CO	38.7	-	-	100.04	25.01
CO_2	44.8	-	-	181.97	45.59
HCl	0.2	-	-	0.67	0.17
HCN	-	-	0.02	0.01	0.01
HF	0.2	-		0.37	0.09
NO_2	0	-	-	0	0

No data was found for HBr or SO_2 for LFP non-flaming thermal runaway. There were zero percent volume data points for NH_3 and only one mass produced normalized by capacity data point in non-flaming LFP thermal runaway, so it was excluded. No data was found for HBr for NMC non-flaming thermal runaway. There were zero percent volume data points for NH_3 and SO_2 and only one mass produced normalized by capacity data point for NH_3 in non-flaming NMC thermal runaway, so those constituents were excluded. Several data points were available for percent volume of HCl in NMC non-flaming thermal runaway with five points being zero and the other two points being 0.2% and 9.7% reported by DNV (2019). However, the 9.7% value is considerably larger compared to the other six data points and is more than 4 standard deviations from the average. As such, the data point was considered an outlier and excluded from the dataset.

Toxic gas release was modeled as supply vents on three modules in one bay of the BESS unit. The species mass flux function was used to input gas production rates for individual species. Figure 2 shows the vent configuration of the non-flaming BESS unit.

In addition to the species mass production rates, FDS required inputs for gas temperature. The average gas temperature was pulled from non-flaming experiments and flaming experiments if the

temperature was measured prior to ignition of the gases. Cell venting temperatures from flaming experiments where HRR contributed to an increase in temperature were excluded. The LFP cell venting temperature was calculated using values from Archibald (2021) and Yuan et al. (2020), resulting in an average temperature of 232°C. The NMC cell venting temperature was calculated using values from Bordes (2022), Yuan et al. (2020), and Zhang et al. 2019, resulting in an average temperature of 329°C.

4.3.2. Flaming Scenario

Mass production rate for each constituent was calculated utilizing the species mass normalized by amount of mass consumed and the average MLR found in Section 4.2.2. Where yields normalized by mass consumed were not available, yields normalized by capacity were used. Yields normalized by mass consumed were prioritized over yields normalized by capacity due to the law of conservation of mass governing a more direct correlation between reactants and products. Yields normalized by mass burned or capacity were not available for soot production, so a yield normalized by cell mass was utilized. Table 63 and Table 64 provide the species yields and mass production rates for the flaming simulations.

Table 63. Flaming species yields and mass production rates for LFP cells

Species	Yield		Mass Production Rate [g/s]		
	mg/g	mg/Wh	2 hr	4 hr	6 hr
CO	35.1	-	50.7	25.3	16.9
CO_2	1463	-	2112.5	1056.2	704.2
HCl	0.7	-	1.0	0.5	0.3
HF	24.8	-	35.8	17.9	11.9
NH_3	0.5	-	0.7	0.4	0.2
NO_2	1.9	-	2.7	1.4	0.9
SO_2	3.5	-	5.1	2.5	1.7
Soot	56[1]	-	148.5	74.3	49.5

1. Normalized by cell mass

Table 64. Flaming species yields and mass production rates for NMC cells

Species	Yield		Mass Production Rate [g/s]		
	mg/g	mg/Wh	2 hr	4 hr	6 hr
Benzene	-	145.5	62.7	31.3	20.9
CO	42.6	-	46.1	23	15.4
CO_2	420	-	454.8	227.4	151.6
HBr	-	0.6	0.3	0.1	0.1
HCl	0.4	-	0.4	0.2	0.1
HCN	-	0.3	0.1	0.2	0.04
HF	8.2	-	8.9	4.4	3.0
NO_2	-	4.5	1.9	1.0	0.6
SO_2	-	17.7	7.6	3.8	2.5
Soot	52[1]	-	137.9	69	46

1. Normalized by cell mass

No data was found for HBr for LFP flaming thermal runaway. There were no data points normalized by mass and only one data point normalized by capacity for HCN and benzene in flaming LFP thermal runaway, so those constituents were excluded. There were no data points normalized by mass and only one data point normalized by capacity for NH_3 in flaming NMC thermal runaway, so it was excluded. While there was only one data point normalized by mass for HCl, it was prioritized over the yields normalized by capacity.

The flaming scenario was modeled using two separate vents, one for combustion products (CO, CO_2, and soot) and the other for toxic gases. One of each vent was assigned to all nineteen modules. The toxic gas release was modeled using supply vents at the average non-flaming cell venting temperature found in Section 4.3.1. Combustion was modeled using burner vents with the average MLR found in Section 4.2.2. Figure 1 shows the configuration of the flaming BESS unit vents.

Because it is proprietary, the exact composition of chemical constituents in the combustible BESS cells and modules materials was not found in the literature and data searches. As such, a generic methane and H_2 mixture was utilized to model the fuel. Both gases are produced during

Li-ion thermal runaway and are expected to ignite and contribute significantly to the combustion behavior. Additionally, methane burns cleanly without producing other constituents that could influence end concentrations. If only methane was burned, the incorrect yield for CO_2 would be produced. H_2 was added to produce the stoichiometry that would result in the required combustion yields.

The FDS combustion calculator (Swenson) was utilized to calculate the ratio of methane to H_2, as well as the yields for CO, CO_2, and soot required to produce the same yields found in Section 4.3. FDS accepts inputs for fuel ratio and yields for CO, soot, and HCN. Calculations for HCN were not performed as it was assumed that the majority of HCN production would be due to the cell contents. The model then calculates a yield for CO_2 based on the inputs. To balance the mixture, percentages of methane were tested to find the correct inputs. The expected yield of CO_2 was then confirmed using the FDS combustion calculator.

Table 65 and Table 66 present the calculations for the percent methane in the fuel mixture, the required yield inputs for CO and soot, and the CO_2 production calculated in FDS under those inputs.

Table 65. Combustion calculations for LFP cells

Percentage Testing				
	CO	**CO2**	**HCN**	**Soot**
Yield Required [kg/kg]	0.0351	1.4630	0.0000	0.1029
% methane	0.6900			
Inputs [kg/kg]	0.0509	-	0.0000	0.1491
Yield Calculated [kg/kg]	0.0509	2.1222	0.0000	0.1491
Yield if %fuel is burned [kg/kg]	0.0351	1.4643	0.0000	0.1029

Table 66. Combustion calculations for NMC cells

Percentage Testing				
	CO	**CO2**	**HCN**	**Soot**
Yield Required [kg/kg]	0.0426	0.4204	0.0000	0.1275
% methane	0.3600			
Inputs [kg/kg]	0.1183	-	0.0000	0.3541
Yield Calculated [kg/kg]	0.1183	1.1728	0.0000	0.3541
Yield if %fuel is burned [kg/kg]	0.0426	0.4222	0.0000	0.1275

The resulting mixture was 69% methane and 31% H_2 for the LFP simulations and 36% methane and 64% H_2 for the NMC simulations. This ratio of methane to H_2 was released from the burner vent as fuel for combustion.

4.3.3. Unique Hazard of Li-ion Emissions

Emission factors for flaming Li-ion battery thermal runaway and ventilated fires involving various other fuels were gathered from the literature reviewed in Section 3.1 for comparison purposes. Gas yields associated with flaming Li-ion battery thermal runaway are provided in the first two rows of Table 67. In addition, Table 67 presents gas yields for a range of other common fire fuels. Only flaming thermal runaway was compared as the yields were quantified under fire conditions. Cells highlighted in green indicate a yield that is less than expected in a Li-ion battery fire. Cells highlighted in yellow indicate a yield that is like that expected in a Li-ion battery fire. Cells highlighted in red indicate a yield that is higher than expected in a Li-ion battery fire.

Table 67. Yield comparison between flaming Li-ion thermal runaway and non-Li-ion fires

Fuel Type	Gas Yields [mg/g]								Source
	HF	CO	CO_2	HCN	HBr	HCl	NO_x	SO_2	
LFP Flaming	24.8	35.1	1463	-	-	0.7	1.9	0.5	Table 63
NMC Flaming	8.2	42.6	420.4	-	-	0.4	-	-	Table 64
Furnished living room	-	44	2960	-	-	-	-	-	NFRL, 2020
Oil spill (Megantic Lake, 5500 tons)	-	35	2640	-	-	-	0.5	23	INERIS, 2022[c]
Prescribed burning (savannah and forest)	-	115	-	-	-	-	-	-	Lemieux et al., 2004
Agricultural burning	-	58	-	-	-	-	-	-	
Land clearing	-	16	-	-	-	-	-	-	
Home appliance products	0.54	29	1400	6	0	3.2	5.3	7	INERIS, 2022[c]
Miscellaneous furniture	-	41	890	1.3	0.26	0.37	-	6	
Computer equipment (crushed)	0	14	4100	2	14	6.8	9.5	0	
PU[a]	0	30	1500	1.8	0	0	90	0	
PE[b]	0	24	2800	0	0	0	1.7	0	
Raw wood	-	56	1600	-	-	32	2.3	-	
Yard waste	-	56	-				-	-	Lemieux et al., 2004
Household waste	-	42	-				-	0.5	
Waste basket	-	-	-				-	-	Blomqvist et al., 2007
Electrical cables	8.3	180	560	22	22	54	8.8	9.7	INERIS, 2022[c]
Vehicle (car, boat, train)	-	62.4	-	-	-	-	2	-	Lemieux et al., 2004
ICEV (car)	0.04	26	1400	-	0.1	4.4	2	1.9	Willstrand et al., 2020

Note a: PU is found in upholstered furniture, insulation, paints, and foam toys
Note b: PE is used to make bottles, plastic containers, rope, and plastic bags
Note c: Where maximum, minimum, and means values were provided, the mean value is presented in this table

As shown in Table 67, the NMC Li-ion battery flaming thermal runaway yields for HF (8.2 mg/g for NMC) is observed to be similar to the HF emission factors for electric cables (8.3 mg/g) but significantly more than those for the other fuels, all of which had an emission factor of less than 1 mg/g. The LFP cell chemistry had an HF yield (24.8 mg/g) that was a magnitude greater than that of the NMC cell chemistry and the electric cables. Conversely, CO_2 yields were higher or similar to the yields produced by the LFP and NMC Li-ion batteries. Yields for CO, HCl, NO_x, and SO_2 vary significantly across fuels, with some fuels registering yields at less than 1 or 0 mg/g, while other fuels are a magnitude or two larger. Electric cables, raw wood, the furnished living room, agricultural and prescribed burns, yard waste, and vehicles produced similar or worse yields compared to Li-ion battery flaming thermal runaway. For Li-ion battery flaming thermal runaway, the most unique toxic gas produced is HF. Only HF was produced at consistently higher yields in comparison to the other fuels. This is congruent with the general focus of the industry on HF production as the main toxicological hazard of Li-ion battery combustion.

4.4. Meteorological Conditions

The modeling included a sensitivity analysis for wind and temperature using minimum, average, and maximum conditions. The plume was modeled over a relatively flat terrain. Weather conditions were chosen based on southern California, as it is one of the areas in the U.S. where BESS installations are prevalent, and include the parameters presented in Table 68.

Table 68. FDS model weather inputs

	Minimum	Average	Maximum
Wind [mph (m/s)]	0	5.2 (2.32)	10 (4.47)
Temperature [°F (°C)]	45 (7)	72 (22)	95 (35)

Note: Adapted from Weather Spark. Climate and Average Weather Year-Round in California.

The Monin- Obukhov Similarity was applied in FDS to account for the change in wind velocity by height due to the boundary layer. FDS requires inputs for base windspeed, which is provided in Table 68, reference height, terrain roughness, thermal stability, and temperature lapse rate. The reference height chosen was 10 m since weather stations in the U.S. typically read surface wind measurements at this height. A roughly open terrain (z_0 = 0.1) was chosen to mimic the base conditions (flat terrain with low-lying vegetation). The model was run with a very thermally unstable parameter (L = -100 m). Temperature lapse rate was set to 0 °C/m, which created a constant temperature profile with height.

4.5. Methods to Evaluate Health Impact

There are various human health exposure guidelines in the United States that have been developed, primarily, by OSHA, NIOSH, and American Conference of Governmental Industrial Hygienist (ACGIH), and the EPA. The various exposure limits defined by the aforementioned organizations are widely used and accepted in the safety and health industry, and in some cases, are mandated through statutes. The plume gas concentrations were compared to the following exposure guidelines to determine the furthest distance at which concentrations exceeded guideline thresholds within the computational domain. Distances were evaluated at 1.5 m, the breathing height of the average human. In the FDS simulations, 2D-slice files were added at breathing height to record concentrations during the simulation. The FDS simulation data was processed using pyFDStools, a Python package developed by Hodges (2020) that assists in developing and post-processing FDS data. The Python package is able to generate plots and excel sheets from the 2D-slice files measuring concentration in FDS. Concentrations were averaged for each constituent over the period at which the plume had reached the end of the domain and become steady.

Exposure limit distances were evaluated by finding the furthest point downwind or to the side of the BESS unit where concentrations exceeded either occupational (IDLH) or community (AEGL-1, ERPG-1, or TEEL-1) exposure limits within the domain. If a gas was above an exposure limit at the furthest points in the domain, it was documented in the results, but not evaluated outside of the boundaries of the domain.

4.5.1. Occupational Exposure

Occupational exposure levels were assessed to focus on the impact on those in the immediate vicinity of the equipment, e.g., emergency response personnel. The IDLH values were developed by NIOSH to protect workers from high-risk exposures to toxic chemicals in the workplace and to determine when (and what type of) respiratory protection is required. IDLH values represent the maximum airborne concentration a healthy adult workers (without a respirator) could be exposed for 30-minutes without suffering permanent or escape-impairing health effects (NIOSH, 2004). Table 69 presents the IDLH values for the evaluated toxic gases.

Table 69. IDLH Guidelines

Chemical	IDLH [ppm]
Benzene	500
CO	1200
CO_2	40,000
HF	30
HCl	50
HCN	50
HBr	30
NO_2	13
SO_2	100

Note: Adapted from NIOSH, Immediately Dangerous To Life or Health (IDLH) Values, February 2021

The steady state gas concentrations of all constituents were evaluated at IDLH to determine if a negative health impact is likely based on distance from the enclosure and weather conditions.

Concentrations were evaluated downwind of and in the area surrounding the BESS unit. Justifications for IDLH values from NIOSH are provided in Appendix 7.3.

4.5.2. Community Exposure

In this study, it was assumed that the public and communities were not in the immediate vicinity of the BESS unit. As such, acute exposure guidelines, rather than occupational exposure limits, were used to evaluate community health impact and to aid in determining implementation for shelter-in-place or evacuation.

The Protective Action Criteria for Chemicals (PACs) is a database provided by the U.S. Department of Energy (DOE) that compiles emergency exposure limits for uncontrolled release of hazardous chemicals. These values are used to evaluate the severity of the event and provide the necessary information to plan emergency response. The PACs hierarchy requires that final and interim 1-hour exposure duration Acute Exposure Guideline Levels (AEGL) values are used preferentially, followed by Emergency Response Planning Guidelines (ERPG) values, then Temporary Emergency Exposure Guidelines (TEEL) values when evaluating consequences (DOE NNSA). The EPA AEGL are used for rare releases of chemicals into the air, such as the toxic gas production that occurs during an unwanted fire event. The AEGLs are provided for a range of exposure doses at which the general population and susceptible individuals will experience a given impact. There are three levels of AEGL guidelines associated with different health effects and are defined by the EPA as follows:

1. **AEGL-1**: “The concentration of a substance above “which it is predicted that the general population could experience, including susceptible individuals, notable

discomfort, irritation, or certain asymptomatic non-sensory effects."

2. **AEGL-2**: "The concentration of a substance above which it is predicted that the general population could experience, including susceptible individuals, including susceptible individuals, could experience irreversible or other serious, long-lasting, adverse health effects or an impaired ability to escape."
3. **AEGL-3**: "The concentration of a substance above which it is predicted that the general population could experience, including susceptible individuals, life-threatening health effects or death." (EPA, 2023, About AEGL)

Each AEGL is divided into exposure for 10 minutes, 30 minutes, 1 hour, 4, hours, and 8 hours. Depending on the chemical, the AEGL may change due to the dose-time relationship. For the purposes of this study, exposure considerations will be limited to AEGL-1 as evacuation or shelter-in-place orders would need to be given before irreversible health effects or impairment of ability to escape. Table 70 provides a list of AEGL-1 values for the evaluated toxic gases.

Table 70. AEGL-1 Guidelines

Chemical	1-hour Exposure Duration AEGL-1 [ppm]
Benzene	52
CO	See Note a.
CO_2	See Note b.
NO	See Note a.
NO_2	0.50
HF	1.0
HCl	1.8
HCN	2.0
HBr	1.0
SO_2	0.20

a. Data is insufficient, no guideline established.
b. Not assessed.

Note: Adapted from EPA, Access Acute Exposure Guideline Levels (AEGLs) Values, retrieved 10/22/2024.

Justifications for AEGL-1 values from the EPA are provided in Appendix 7.2.

The ERPGs were developed by the American Industrial Hygiene Association (AIHA). Unlike AEGLs, ERPGs are not designed with susceptible individuals in mind. The ERPGs are also divided into three tiers based on different health effects. These tiers are defined by the AIHA as follows:

1. **ERPG-1**: "The maximum airborne concentration below which nearly all individuals could be exposed for up to 1 hour without experiencing more than mild, transient adverse health effects or without perceiving a clearly defined objectionable odor."
2. **ERPG-2:** "The maximum airborne concentration below which nearly all individuals could be exposed for up to 1 hour without experiencing or developing irreversible or other serious health effects or symptoms which could impair an individual's ability to take protective action."
3. **ERPG-3:** "The maximum airborne concentration below which nearly all individuals could be exposed for up to 1 hour without experiencing or developing life-threatening health effects" (NOAA, 2023, ERPGs).

Similarly, for the purposes of this study, exposure considerations will be limited to ERPG-1. Table 71 provides a list of ERPG-1 values for the evaluated toxic gases.

Table 71. ERPG-1 Guidelines

Chemical	ERPG-1 [ppm]
Benzene	See Note a.
CO	200
CO_2	See Note b.
NO	See Note b.
NO_2	See Note a.

HF	See Note a.
HCl	See Note a.
HCN	See Note a.
HBr	See Note a.
SO_2	See Note a.

a. AEGL values were available, therefore ERPG values were not provided
b. Not assessed.
N/A: not appropriate
Note: Adapted from NOAA, CAMEO Chemicals, retrieved 10/22/2024.

The TEELs were developed by the DOE and are used to evaluate short-term chemical releases when neither AEGLs nor ERPGs are available. TEELs are designed with both the general population and susceptible individuals in mind. Unlike AEGLs and ERPGs, TEELs are not derived from review of animal and human studies. Recognizing that the method of defining AEGLs and ERPGs is more accurate, TEELs are replaced when an AEGL or ERPG value is available. The TEELs are also divided into three tiers based on different health effects. These tiers are defined by the DOE as follows:

1. **TEEL-1**: "The airborne concentration of a substance above which it is predicted that the general population, including susceptible individuals, when exposed for more than one hour, could experience notable discomfort, irritation, or certain asymptomatic, nonsensory effects. However, these effects are not disabling and are transient and reversible upon cessation of exposure."

2. **TEEL-2**: "The airborne concentration of a substance above which it is predicted that the general population, including susceptible individuals, when exposed for more than one hour, could experience irreversible or other serious, long-lasting, adverse health effects or an impaired ability to escape."

3. **TEEL-3**: “The airborne concentration of a substance above which it is predicted that the general population, including susceptible individuals, when exposed for more than one hour, could experience life-threatening adverse health effects or death.” (NOAA, 2023, TEELs)

Similarly, for the purposes of this study, exposure considerations will be limited to TEEL-1. Table 72 provides a list of TEEL-1 values for the evaluated toxic gases.

Table 72. TEEL-1 Guidelines

Chemical	TEEL-1 [ppm]
Benzene	See Note a.
CO	See Note a.
CO2	30,000
NO	0.5
NO_2	See Note a.
HF	See Note a.
HCl	See Note a.
HCN	See Note a.
HBr	See Note a.
SO2	See Note a.

a. AEGL and ERPG values are available, therefore TEELs were not provided.

Note: Adapted from NOAA, CAMEO Chemicals, retrieved 10/22/2024.

The steady state gas concentrations derived from the non-flaming and flaming models were compared against the 1-hour AEGL-1, ERPG-1, and TEEL-1 values to determine if a negative health impact is likely based on distance from the enclosure and weather conditions. AEGL-1, ERPG-1, and TEEL-1 values were utilized to evaluate only the area downwind of the BESS unit within the domain. Further, it was assume the public and communities are not in the immediate vicinity of the BESS unit.

5. Results and Discussion

The results in this section represent a range of possible gas concentration profiles and exposure limit distances that could result from different types of BESS thermal runaway events. The results are derived from the full range of HRR, THR, MLR, and gas species data currently available in the literature for NMC and LFP chemistries. The results are not intended to represent probably outcomes of a thermal runaway event in a specific product and should not be used in that manner without verifying that the inputs are applicable to the scenario(s) in question.

Figure 6 through Figure 9 show the HRR and species gas production rates for each cell chemistry and thermal runaway condition (non-flaming vs. flaming) for the shortest incident duration. For the LFP and NMC non-flaming scenarios, the shortest incident duration was 6 and 0.5 hours, respectively. For the flaming scenarios, the shortest incident duration was 2 hours. The HRR and species gas production rate curves for longer incident durations have the same trends as the graphs presented below.

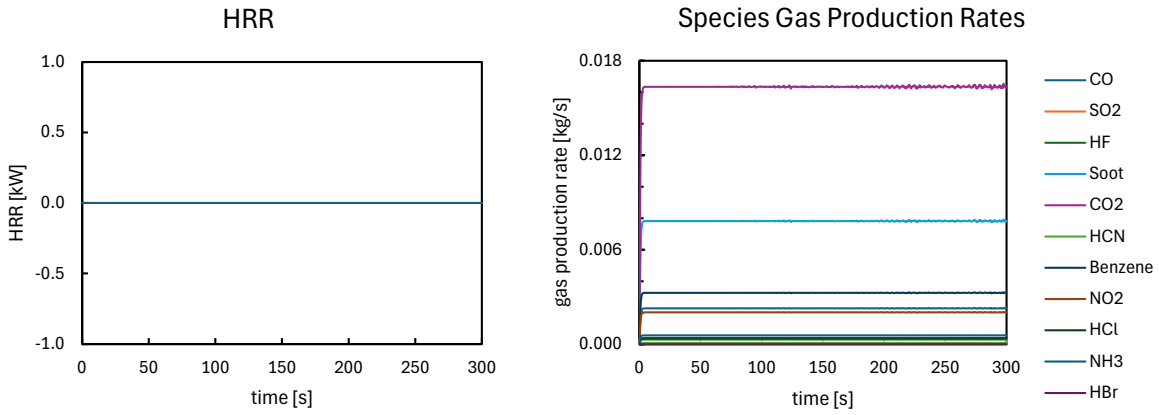

Figure 6. HRR and species gas production rates for the LFP non-flaming scenario at a 6-hour incident duration

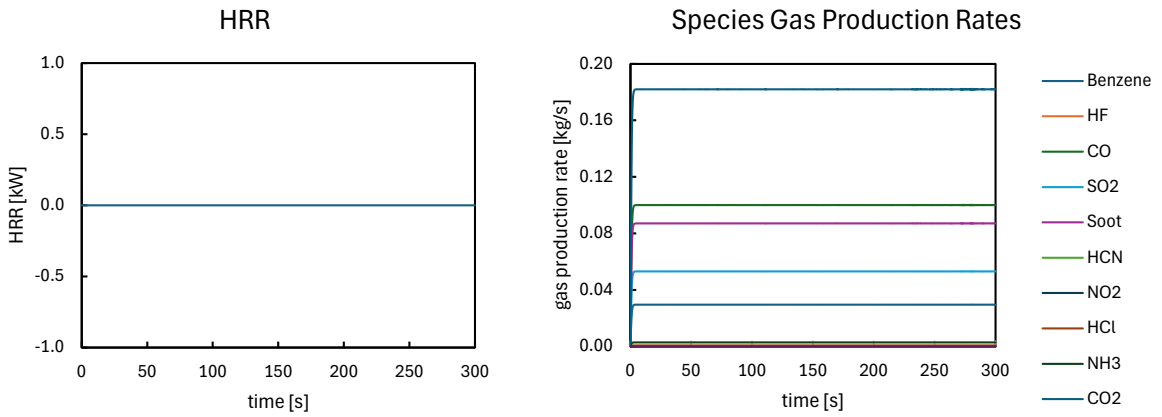

Figure 7. HRR and species gas production rates for the NMC non-flaming scenario at a 0.5-hour incident duration

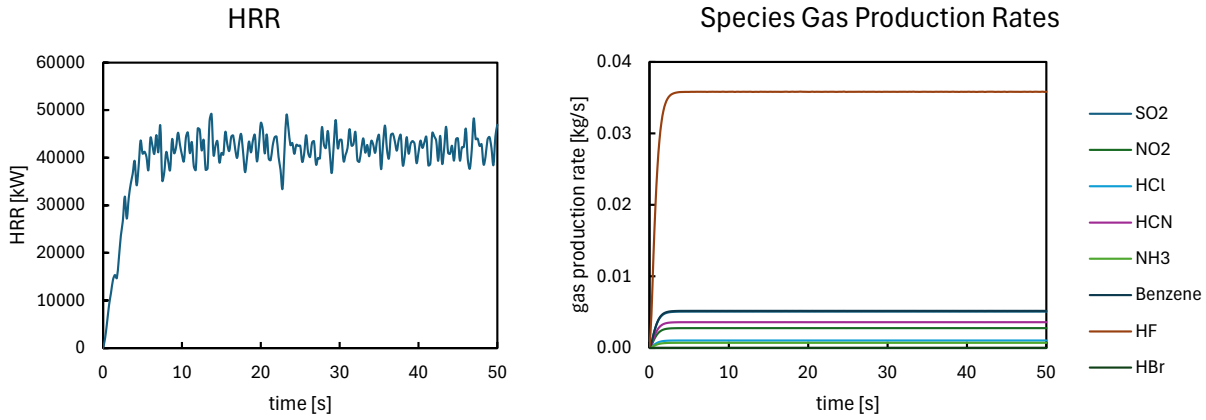

Figure 8. HRR and species gas production rates for the LFP flaming scenario at a 2-hour incident duration

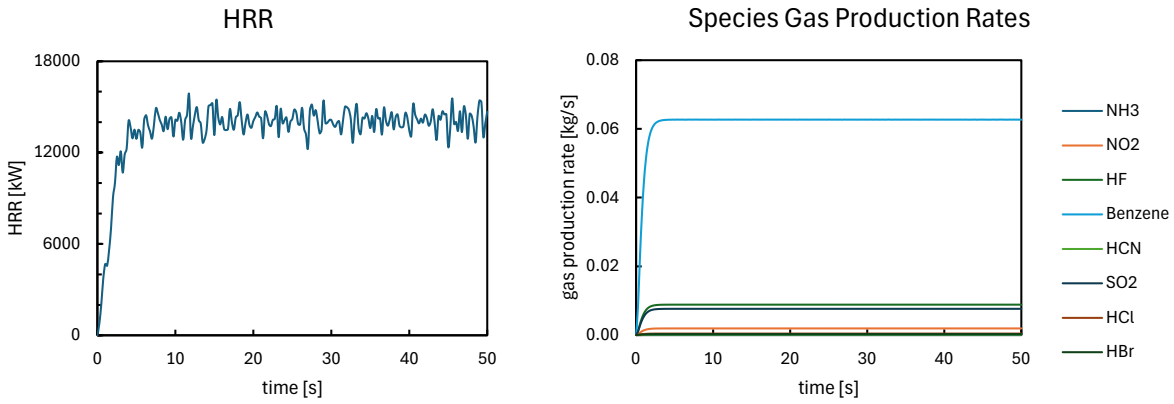

Figure 9. HRR and species gas production rates for the NMC flaming scenario at a 2-hour incident duration

The full list of exposure limit distances for each scenario are provided in Appendix 7.4. Exposure limit distances evaluated by AEGL concentrations are always further than IDLH distances due to the more conservative nature of AEGL limits. Across all factors (non-flaming vs. flaming, cell chemistry, wind, temperature, and duration), CO_2 is the only gas that remained below both IDLH and TEEL-1 concentrations outside the BESS unit.

The furthest IDLH distance for LFP, non-flaming is 70 m and is produced by NO_2 under a 5 m/s wind speed at 35°C for a 6-hour duration incident. The furthest AEGL-1 distance for LFP non-flaming exceeds the length of computational domain (200 m) and is by NO_2 produced under all wind speeds, ambient temperatures, and incident durations. The furthest IDLH distance for NMC non-flaming is 22 m and is produced by CO under a 10 m/s wind speed at 35°C for a 0.5-hour duration incident. The furthest AEGL-1 distance for NMC non-flaming is 140 m and is produced by HF under a 10 m/s wind speed at 35°C for a 0.5-hour duration incident. Figure 10 through Figure 13 present the concentration plots for the non-flaming cases that produced the furthest distances assessed by occupational and community exposure limits.

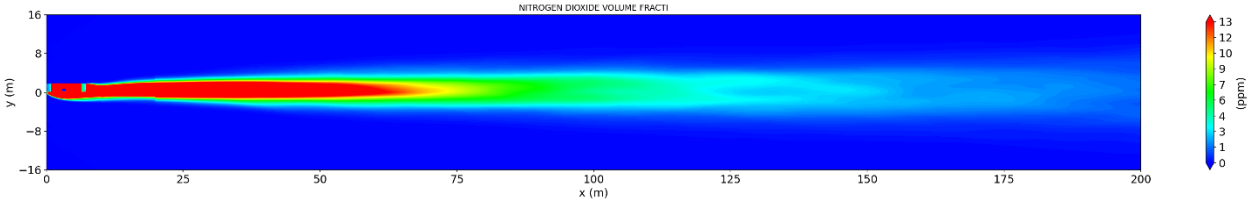

Figure 10. LFP non-flaming NO_2 IDLH concentrations at 2 m/s, 35°C, and 6-hour duration

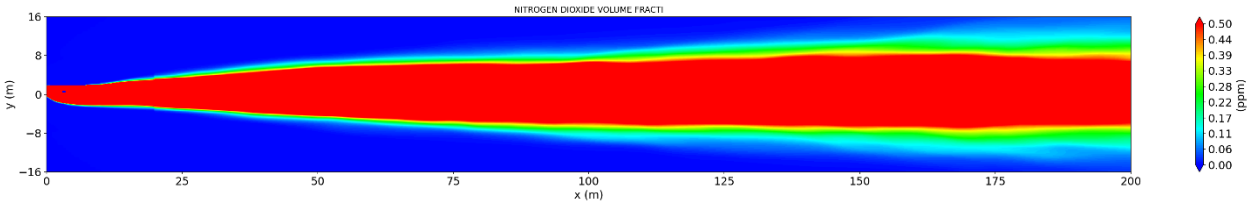

Figure 11. LFP non-flaming NO_2 AEGL-1 concentrations at 2 m/s, 22°C, and 6-hour duration

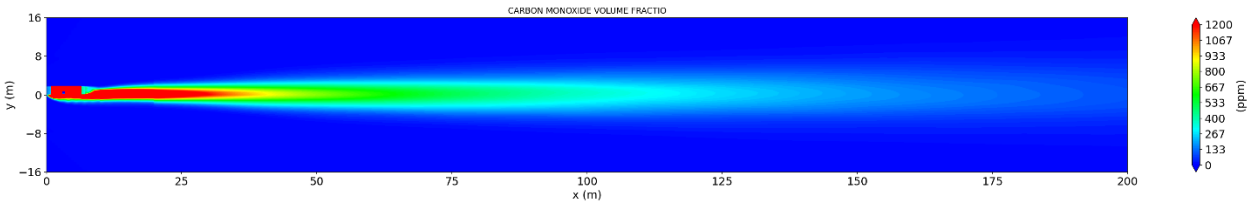

Figure 12. NMC non-flaming CO IDLH concentrations at 10 m/s, 35°C, and 0.5-hour duration

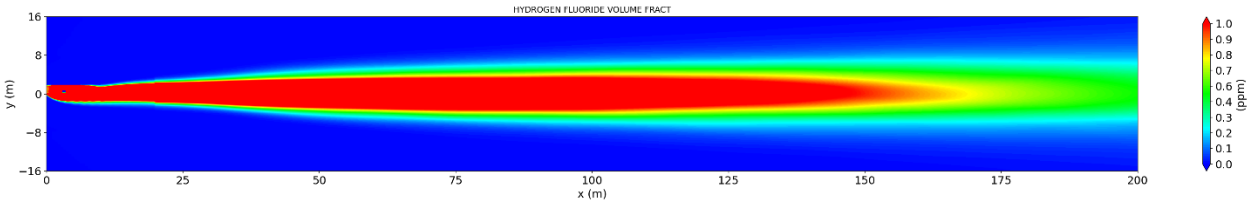

Figure 13. NMC non-flaming HF IDLH concentrations at 10 m/s, 35°C, and 0.5-hour duration

The furthest IDLH distance for LFP flaming is 1.125 m and is produced by HF under a 10 m/s wind speed at 22 and 35°C for a 2-hour duration incident. The furthest AEGL-1 distance for LFP flaming is 16 m and is produced by HF under a 10 m/s wind speed at 22°C for a 4-hour duration incident. The furthest IDLH distance for NMC flaming is 1 m and is produced by HF under a 10 m/s wind speed at 7, 22, and 35°C for a 2-hour duration incident. The furthest AEGL-1 distance for NMC flaming is 15 m and is produced by SO_2 under a 10 m/s wind speed at 35°C for a 6-hour duration incident. Figure 14 through Figure 20 present the concentration plots for the flaming cases that produced the furthest distances assessed by occupational and community exposure limits.

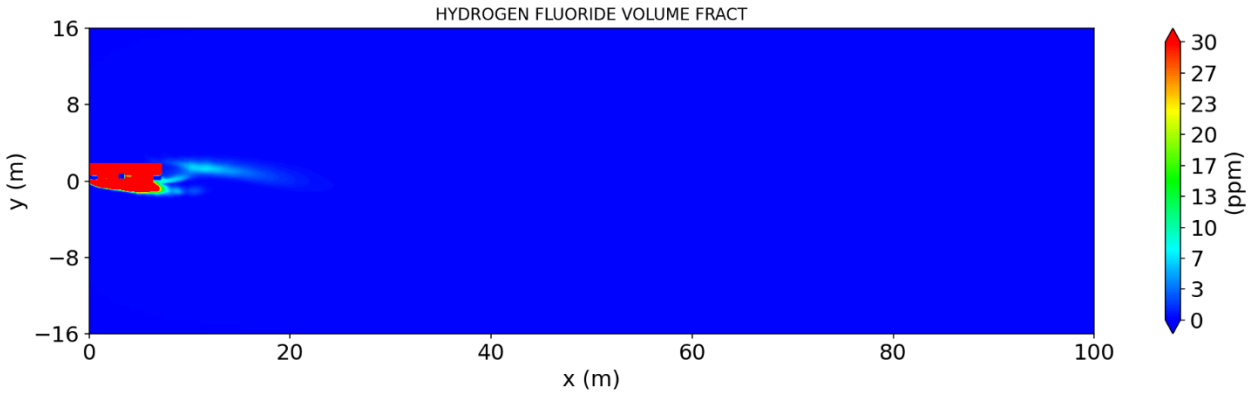

Figure 14. LFP flaming HF IDLH concentrations at 10 m/s, 22°C, and 2-hour duration

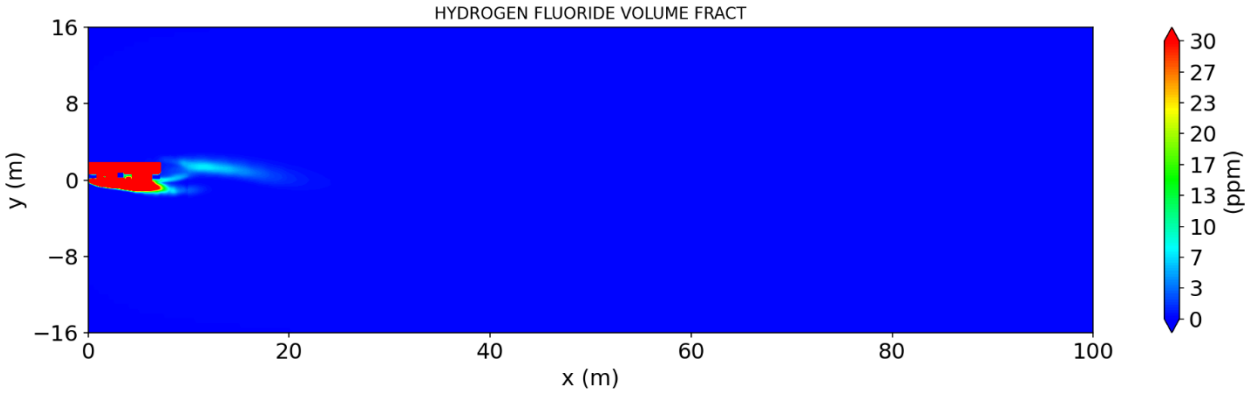

Figure 15. LFP flaming HF IDLH concentrations at 10 m/s, 35°C, and 2-hour duration

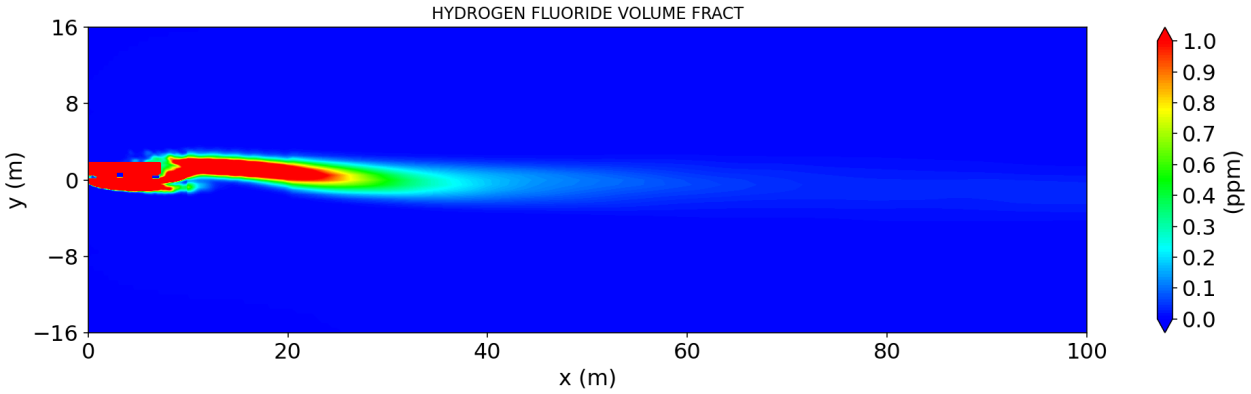

Figure 16. LFP flaming HF AEGL-1 concentrations at 10 m/s, 22°C, and 4-hour duration

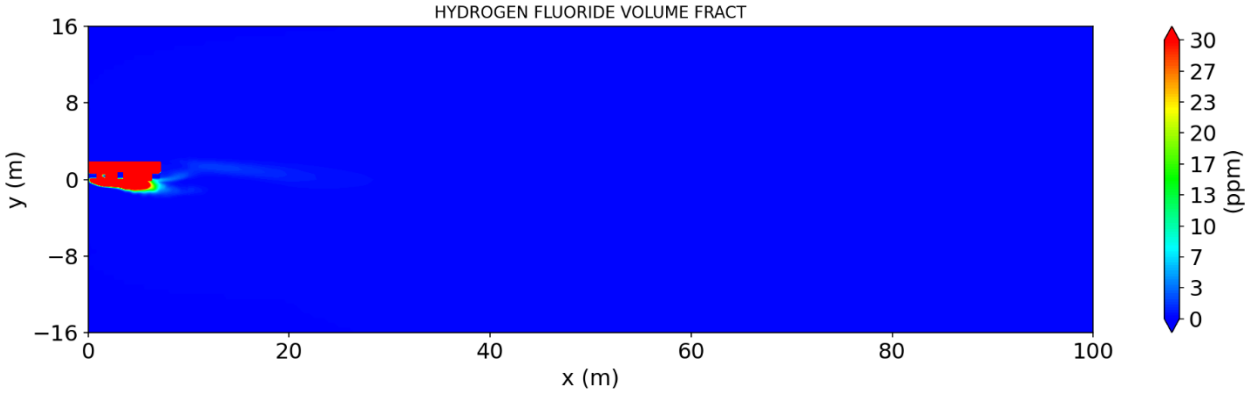

Figure 17. NMC flaming HF IDLH concentrations at 10 m/s, 7°C, and 2-hour duration

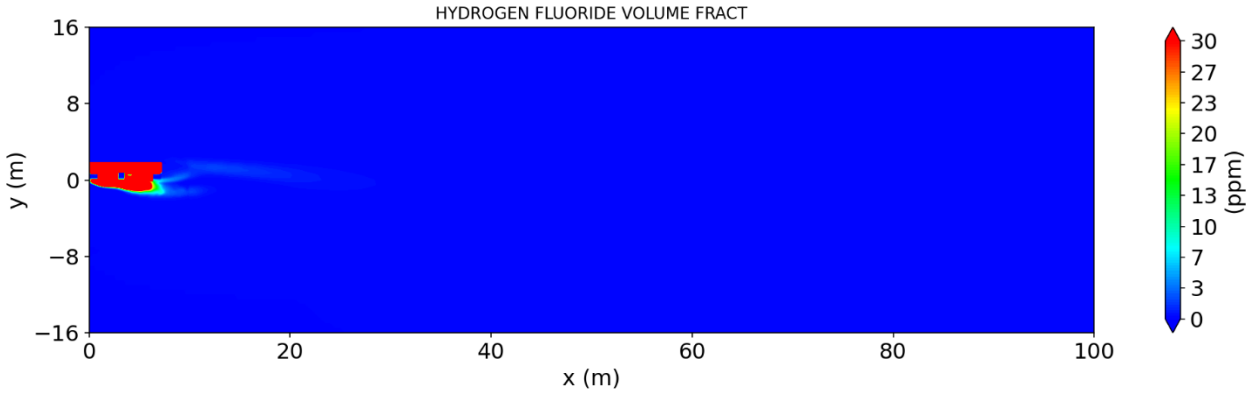

Figure 18. NMC flaming HF IDLH concentrations at 10 m/s, 22°C, and 2-hour duration

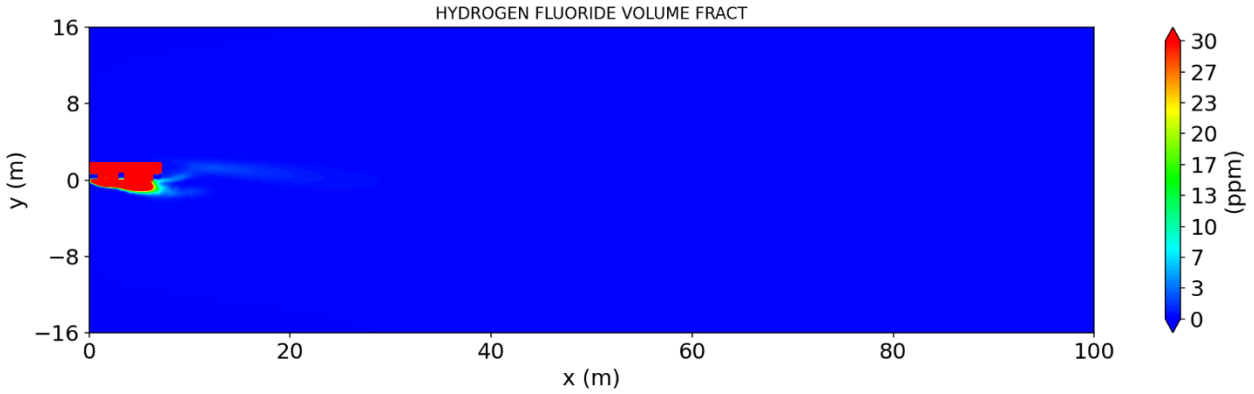

Figure 19. NMC flaming HF IDLH concentrations at 10 m/s, 35°C, and 2-hour duration

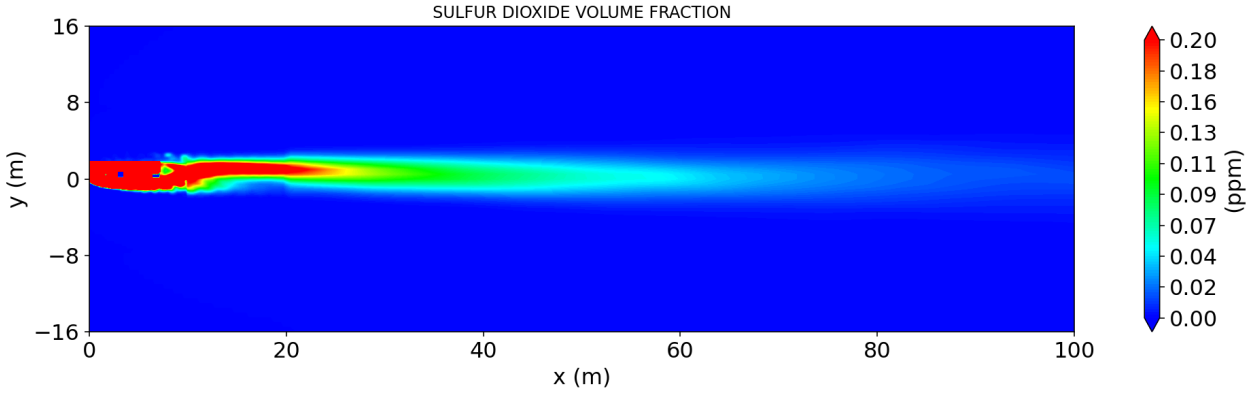

Figure 20. NMC flaming SO_2 AEGL-1 concentrations at 10 m/s, 35°C, and 6-hour duration

While Figure 14 through Figure 19 show the furthest distances for the flaming LFP and NMC evaluated at IDLH, all distances evaluated at IDLH are within half a meter of each other. The

flaming and non-flaming concentrations above represent the worst-case scenario for occupational and community exposures using the given methodology and data sets. The proceeding sections discuss the factors that impact exposure limit distances; these factors should be considered when conducting a site-specific hazard evaluation.

5.1. Factors Affecting Non-Flaming Exposure Limit Distance

The constituents evaluated for the LFP non-flaming scenarios were benzene, CO, CO_2, HCl, HCN, HF, and NO_2. Of these gases, benzene, CO, CO_2, HCl, and HCN never reached IDLH limits outside the BESS unit. Additionally, CO_2 never reached the TEEL-1 limit for the LFP scenarios. The constituents evaluated for the NMC flaming scenarios were benzene, CO, CO_2, HCl, HCN, and HF. Of these gases, CO_2, HCl, and HCN never reached IDLH limits outside the BESS unit. HCN never reached the AEGL-1 limit, and CO_2 never reached the TEEL-1 limit outside the BESS unit for the NMC scenarios.

Overall, the furthest distances determined by community exposure limits for the LFP simulations are larger than the furthest distances for the NMC simulations. The average gas production rate for NMC (207 L/s) is two orders of magnitude higher than the LFP average gas production rate (6 L/s) due to the higher total gas production from NMC cells and the shorter duration over which the gases are released. Gas production rates for benzene, CO, CO_2, HCl, and HF are higher in the NMC cells. However, only benzene and CO distances for the NMC simulations are further than distances for the LFP simulations. This can be attributed to the difference in plume development. Figure 21 and Figure 22 present the plume development for the LFP and NMC non-flaming scenarios under a 2 m/s wind speed at 22°C for a 6-hour and 0.5-hour

incident duration, respectively. An artificial soot density was added to the non-flaming scenarios to aid in visualization of the smoke plume. It is expected that a plume from a non-flaming thermal runaway condition would be opaque, as soot is not produced during non-flaming conditions.

Figure 21. LFP non-flaming plume at 2 m/s, 22°C, and 6-hour duration

Figure 22. NMC non-flaming plume at 2 m/s, 22°C, and 0.5-hour duration

As shown above, the LFP plume is closer to breathing height compared to the NMC plume. The lower gas production rate of the LFP plume causes the plume to be less dense and buoyant. Additionally, the average cell venting temperature of LFP cells is lower compared to the NMC cells, which decreases buoyancy. Benzene and CO have gas production rates that are one order and two orders of magnitude, respectively, above the LFP production rates; the increased production rates overcame the impact caused by the buoyancy of the NMC plume at breathing height.

Higher constant ambient temperatures consistently increase the furthest distance that both occupational and community exposure limits are reached. All non-flaming worst-case scenarios are evaluated at 35°C ambient temperature. Although it was expected that the higher wind speeds would produce long distances, this was not the case for the non-flaming scenarios. The wind speed that produces the furthest exposure limit distance for LFP is dependent on species, incident duration, temperature, and the type of exposure limit. When evaluated at IDLH, HF and NO_2 tend to produce further distances at the 5 m/s wind speed in the 6-hour duration simulations, whereas the 2 m/s wind speed produces further distances in the 12-hour duration simulations. However, HF produces further distances at 5 m/s regardless of incident duration when evaluated at AEGL-1. CO follows a similar pattern, although none of the 12-hour incident duration simulations reach ERPG-1 limits outside of the BESS unit. The reason the lower wind speeds (2 m/s and 5 m/s) cause concentrations to exceed exposure limits at a further distance may be due to the plume density. As shown in Figure 21 and Figure 22, the LFP non-flaming plume is closer to the ground and less dense compared to the NMC plume. Figure 23 presents the LFP non-flaming scenario under a 10 m/s wind speed at 22°C for a 6-hour incident duration.

Figure 23. LFP non-flaming plume at 10 m/s, 22°C, and 6-hour duration

When comparing the 2 m/s and 10 m/s scenarios, the plume is more dispersed in the 10 m/s scenario. The already low buoyancy and density that characterizes the LFP non-flaming plume allows the plume to be dispersed more readily at higher wind speeds. At the 10 m/s wind speed, the LFP non-flaming plumes have dispersed too much to reach concentrations that exceed exposure limits, despite the plume being closer to breathing height. Since the 12-hour incident duration simulations release gas at a lower rate, the plume is more likely to disperse at a 5 m/s wind speed compared to the 6-hour incident duration simulations.

When evaluated at community exposure limits, HCl and benzene tend to produce further distances at the 5 m/s wind speed in the 6-hour duration simulations and at the 2 m/s wind speed in the 12-hour duration simulations. HCN follows a similar pattern at lower temperatures (7°C). At higher temperatures (22°C and 35°C), HCN tends to produce further distances at 2 m/s regardless of duration. It is possible that the different trends between each species are due to the varying molecular weights; however, the exact effect is unclear. More research is required to see how molecular weight impacts concentrations at lower gas production rates.

For the NMC simulations evaluated at community exposure limits, the 0.5-hour duration simulations produce further distances at the 10 m/s wind speed, whereas the 5 m/s wind speed produces further distances for the 2-hour duration simulations. The 2 m/s wind speeds always produce the shortest distance for the NMC simulations. HF and benzene barely reach IDLH concentrations outside of the BESS unit (0.25 m). Only CO levels reach IDLH limits at a significant distance and followed the same pattern as the community exposure limits, except at 35°C for the 0.5-hour incident duration simulations. The effect of duration on wind speed furthest distance patterns may be due to the difference in gas release. Figure 24 presents the plume

development for the NMC non-flaming scenario under a 2 m/s wind speed at 22°C for a 0.5-hour incident duration.

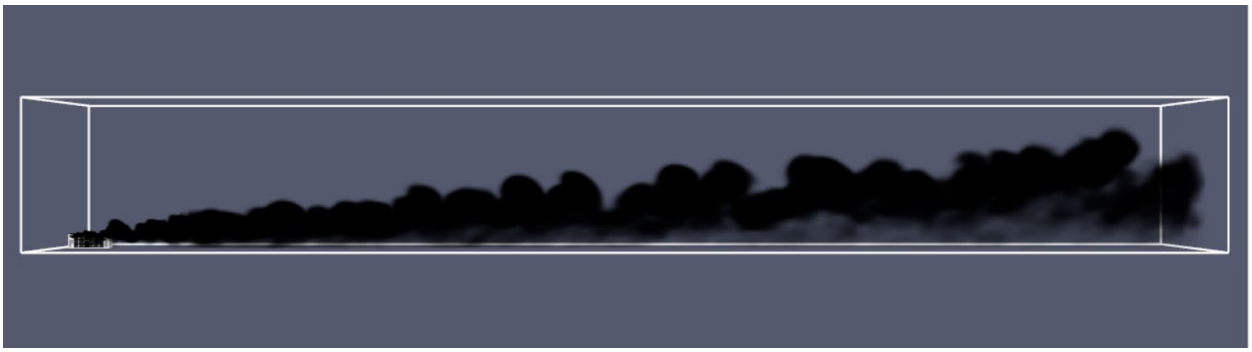

Figure 24. NMC non-flaming plume at 2 m/s, 22°C, and 2-hour duration

Compared to the 0.5-hour incident duration plume, the 2-hour incident duration plume is closer to the ground and less buoyant. This causes the 2-hour incident duration plume to disperse more readily and behaves similarly to the LFP non-flaming plume. The 0.5-hour plume has a higher gas release rate that allows the plume to maintain its shape and buoyancy. Thus, the primary factor controlling exposure limits is the wind which can push the plume to breathing height.

5.2. Factors Affecting Flaming Exposure Limit Distance

The constituents evaluated for the LFP flaming scenarios are CO, CO_2, HCl, HF, NH_3, NO_2, and SO_2. Of these gases, CO, CO_2, HCl, NH_3, and SO_2 never reach IDLH limits outside the BESS unit. CO, CO_2, HCl, and NH_3 never reach community exposure limits for the LFP scenarios. The constituents evaluated for the NMC flaming scenarios are benzene, CO, CO_2, HBr, HCl, HCN, and HF. Of these gases, benzene, CO, CO_2, HBr, HCl, and HCN never reach IDLH limits outside the BESS unit. CO_2, HCl, and HCN never reach community exposure limits for the NMC scenarios.

In general, the LFP and NMC flaming cases produce similar furthest distances. The LFP cell chemistry produces higher total MLRs compared to the NMC cell chemistry. Species production for HF, CO, CO_2, HCl, NO_2, HCN, and NH_3 are higher for the LFP cell chemistry. However, the gas concentrations in the plume had less impact on the furthest distance compared to the plume development and effect of wind. Figure 25, Figure 26, and Figure 27 provide the plume development for the LFP flaming scenario under a 2, 5, and 10 m/s wind speed at 22°C for a 2-hour incident duration, respectively. The NMC and LFP flaming plumes have similar profiles. The plume development for the 2 m/s wind scenario appears to flatten at the mesh boundary; however, running the simulation with a taller domain shows that the plume continues to rise and bends sideways approximately at the mesh domain.

Figure 25. LFP non-flaming plume at 2 m/s, 22°C, and 2-hour duration

Figure 26. LFP non-flaming plume at 5 m/s, 22°C, and 2-hour duration

Figure 27. LFP non-flaming plume at 10 m/s, 22°C, and 2-hour duration

As shown above, the proximity of the plume to breathing height is significantly affected by the increase in wind speed. Both the LFP and NMC simulations produce similarly buoyant plumes. As expected, the higher wind speeds push the plume down further, resulting further occupational and community exposure limit distances. All worst-case scenarios for the flaming cases are evaluated at the 10 m/s wind speed, regardless of temperature or cell chemistry. Duration tends to decrease the distance at which exposure limits were exceeded but does not have as pronounced effect compared to wind speed. Constant ambient temperature has little effect.

5.3. Comparison Between Non-Flaming and Flaming Cases

The non-flaming cases produce further distances at which concentrations exceeded exposure limits at breathing height compared to the flaming cases, despite the overall higher toxic gas concentrations in flaming plumes. This is due to the difference in buoyancy between the two cases. The non-flaming plumes have a lower MLR and temperature, causing them to have a closer proximity to breathing height. Conversely, the flaming plume is too buoyant to sink closer to the ground and in some cases, escapes the vertical domain entirely. For the non-flaming cases, it is unlikely that the plume will be a hazard further away from the BESS unit, apart from the NMC

non-flaming scenarios with a 2-hour incident duration. In most non-flaming cases, the plume mixes with air as it travels and continues to disperse within the domain.

The impact of different factors is more apparent with the non-flaming scenarios. While wind is the main controlling factor in exposure limit distances for the flaming scenarios, the non-flaming scenarios vary significantly by all factors. Cell chemistry, temperature, and species, which significantly change the trends in the non-flaming cases, have little impact in the flaming cases. Additionally, duration has a larger impact on exposure limit distances in the non-flaming scenarios compared to the flaming scenarios.

5.4. Limitations and Future Research

Health impact was primarily quantified through toxic gas inhalation; however, there are other fire plume hazards that may cause adverse health effects. Flaming thermal runaway of BESS units has the potential to disperse heavy metals and particulate matter. This study does not evaluate these hazards, and FDS has not been validated for particulate matter deposition. However, there are other programs that model particulate matter deposition which can be used to evaluate heavy metal and particulate matter deposition.

Other factors, such as relative humidity, precipitation, and topography can influence the results. While these factors were not explored in this research, it is important to consider how they may impact plume buoyancy and development and associated toxic gas concentrations and exposure limit distances. It should also be noted that while the model was run with an Obukhov length of -100 m to indicate thermal instability, the environmental temperature lapse rate was set to 0 °C/m. Due to this error, the ambient temperature of the atmosphere remained constant with

height. When the environmental lapse rate is greater than the dry adiabatic lapse rate of the plume, e.g. the plume cools slower than the surrounding atmosphere, the atmosphere is considered very thermally unstable. If the environmental lapse rate is lower than the moist adiabatic lapse rate of the plume, e.g. plume cools faster than atmosphere, the atmosphere is considered very thermally stable (Nugent & DeCou, 2019). A thermally neutral atmosphere occurs when there is no heat transfer between the air and the ground (Huertas et al., 2021). The modeled atmosphere did not cool, so all scenarios were unintentionally modeled in a thermally stable environment. A thermally stable environment will reduce vertical mixing and turbulence, causing the plume to rise and disperse less. Huertas et al. (2021) showed that for pollutant dispersion evaluated near a road in a flat region, a very thermally stable environment is correlated with higher concentrations near-surface compared to an unstable or neutral atmosphere. A very thermally unstable atmosphere would produce lower concentrations compared to a stable or neutral atmosphere.

This project was primarily focused on the impact within a couple hundred meters of the BESS unit. While most non-flaming plumes dispersed within the domain, the flaming plumes extended beyond the horizontal and vertical limits; The model and analysis did not consider further plume dispersion outside of the domain. In cases where the plume travels large vertical distances, the impact of atmospheric temperature changes with height should be considered to determine if the plume is likely to dissipate above the domain or invert. Air dispersion models, like AERMOD, can be used to explore particulate deposition and plume dispersion over long distances.

The relationship between molecular weight and concentrations under lower gas production rates should also be further explored. Plumes with higher mass release rates were more buoyant and less likely to have variation in the exposure limit distance by species. However, there were

significantly different trends in the toxic gas profiles for the LFP non-flaming scenario at a 12-hour incident duration. FDS takes molecular weight as an input when species are defined. It is possible that this input had some influence on plume dispersion, and it became more visible when the plume was less concentrated, e.g., LFP, non-flaming, 12-hour scenario.

6. Conclusion

This research presents a methodology to assess thermal runaway events in outdoor, large-scale, Li-ion BESS units. Through application of the methodology, a relationship between exposure limit distance and wind speed, ambient temperature, event duration, cell chemistry, and toxic gas species can be assessed. A literature review was conducted to aggregate available data on Li-ion thermal runaway, historical Li-ion BESS incidents, and Li-ion thermal runaway modeling practices. The literature review revealed variations in thermal runaway test methods. Studies had different methods for thermal runaway initiation, type and arrangement of the cells, and HRR, THR, MLR, and gas characterization and quantification. Additionally, the definition of thermal runaway varied between researchers with different temperature ranges or measurements being suggested to define thermal runaway. The variation in approaches presents challenges when comparing data sets. While UL 9540A provides a standardized testing method, there is no requirement for quantification of the full range of gases produced during thermal runaway, e.g., toxic gases. As such, data sets from UL 9540a tests, while more easily comparable, are limited in scope. A review of actual incidents revealed that, oftentimes, the unit model and specifications are not made publicly available.

Non-flaming thermal runaway does not produce heat, so the mass loss was determined by dividing total gas production by event duration. The flaming thermal runaway was characterized by dividing THR by event duration. Total gas production and THR were found by taking the average total gas production or THR normalized by capacity and multiplying by the capacity modeled in each scenario. The worst-case amount of fuel consumed for the non-flaming scenario was one bay or 0.49 MWh due to heat transfer being restricted and unlikely to initiate thermal runaway in other bays. The worst-case amount of fuel consumed for the flaming scenario was the full BESS unit or 3 MWh based on historical incidents. Duration for the non-flaming cases was based on cell venting times. Duration for the flaming cases was based on historical incidents. This provided an average MLR or total gas production rate for each scenario that was applied to gas emission yields to find species production rates. Typically, yields were quantified in mass produced normalized by mass consumed or percent volume composition. Sometimes, they were also quantified in mass produced normalized by capacity. The methodology prioritized mass produced normalized by mass consumed and percent volume composition, because they could be directly applied to the average MLR and are unlikely to over- or underestimate the mass loss. HF was identified as the most unique hazard of Li-ion BESS thermal runaway events, based on the literature review. Models were run with a bounding wind and temperature analysis in FDS. Scenarios were evaluated by measuring the distance at which occupational or community exposure limits were exceeded, e.g. IDLH and PAC, respectively.

NO_2 resulted in the furthest distances for the LFP non-flaming scenarios for both occupational and community exposure limits. CO resulted in the furthest distance for the NMC non-flaming scenarios for occupational exposure limits, while HF resulted in the furthest distance for

community exposure limits. HF resulted in the furthest exposure limit distance for the flaming scenarios for both occupational and community exposure, except the NMC scenario evaluated for community exposure limits which was controlled by SO_2. The non-flaming cases produce further exposure limit distances compared to the flaming thermal runaway cases due to the less buoyant plume. The LFP non-flaming cases have distances of 70 m for occupational exposure and over 200 m for community exposure. The NMC non-flaming cases have distances of 22 m for occupational exposure and 140 m for community exposure. The LFP flaming cases have distances of 1.125 m for occupational exposure and 16 m for community exposure. The NMC flaming cases have distances of 1 m for occupational exposure and 15 m for community exposure. In the modeled scenarios, the flaming distances evaluated at community exposure limits did not reach outside of the horizontal domain; however, because the flaming plume does not disperse within the vertical domain, further evaluation of thermal stability and dispersion is warranted but outside of the scope of this research. For the non-flaming cases, cell chemistry, wind speed, duration, and temperature had significant impact on exposure limit distances. In some cases, the type of toxic gas also influenced trends. For the flaming cases, wind speed was the controlling factor, with duration having some influence on exposure limit distances. The study findings related to exposure distances are specific to the modeled hazard scenarios and associated inputs; the consulting engineer apply the findings from the research in a site-specific hazard analysis without verifying that the modeled scenarios (and associated inputs) are applicable.

7. Appendices

7.1. Emissions Tables

Table 73. LFP non-flaming yields

	% Volume										Mass Produced [mg/wh]									
Source	**HF**	**CO**	**CO_2**	**HBr**	**HCl**	**NO_2**	**SO_2**	**HCN**	**NH_3**	**Benzene**	**HF**	**CO**	**CO_2**	**HBr**	**HCl**	**NO_2**	**SO_2**	**HCN**	**NH_3**	**Benzene**
Archibald (2021)	-	7.8	24.0	-	-	-	-	-	-	-	-	35.3	73.9	-	-	-	-	-	-	-
DNV (2019)	1.6	7.6	44.3	-	1.1	4.9	-	0.1	-	0.0	16.4	108.7	995.9	-	-	115.1	-	1.4	-	0.0
DNV (2019)	1.6	15.9	20.2	-	0.8	9.7	-	0.1	-	0.7	11.4	159.3	317.9	-	-	159.6	-	1.0	-	19.6
DNV (2019)	0.1	26.1	20.9	-	0.3	1.3	-	0.1	-	13.6	2.1	784.2	986.7	-	-	64.1	-	2.9	-	1139.6
DNV (2019)	1.9	12.0	22.5	-	2.1	4.8	-	0.4	-	0.6	16.2	143.1	421.5	-	-	94.0	-	4.6	-	20.0
DNV (2019)	3.7	13.9	23.0	-	1.9	5.6	-	0.7	-	0.0	31.5	165.7	430.9	-	-	109.7	-	8.1	-	0.0
Golubkov (2014)	-	4.8	53.0	-	-	-	-	-	-	-	-	19.2	30.2	-	-	-	-	-	-	-
Golubkov (2015)	-	1.8	93.5	-	-	-	-	-	-	-	-	7.9	642.8	-	-	0.0	-	-	-	-
Golubkov (2015)	-	3.1	85.3	-	-	-	-	-	-	-	-	7.6	330.5	-	-	-	-	-	-	-

Golubkov (2015)	-	4.8	66.2	-	-	-	-	-	-	-	-	12.2	264.8	-	-	-	-	-	-	-
Golubkov (2015)	-	6.4	62.6	-	-	-	-	-	-	-	-	20.9	320.8	-	-	-	-	-	-	-
Golubkov (2015)	-	9.1	48.3	-	-	-	-	-	-	-	-	23.2	193.2	-	-	-	-	-	-	-
Golubkov (2015)	-	6.4	52.2	-	-	-	-	-	-	-	-	28.1	398.0	-	-	-	-	-	-	-
Golubkov (2015)	-	7.7	55.8	-	-	-	-	-	-	-	-	35.5	404.6	-	-	-	-	-	-	-
Huang (2021)	-	-	-	-	-	-	-	-	-	-	0.0	6.4	13.5	-	4.0	-	-	-	3.9	-
Sturk (2019)	-	-	-	-	-	-	-	-	-	-	26.0	-	-	-	-	-	-	-	-	-
Yang (2022)	0.0	10.0	26.0	-	-	-	-	-	-	-	0.0	38.4	168.9	-	-	-	-	-	-	-
Yuan (2020)	-	4.5	25.4	-	-	-	-	-	-	-	-	15.2	134.5	-	-	-	-	-	-	-
MP2 UL 9540A	-	11.0	29.0	-	-	-	-	-	-	0.004	-	-	-	-	-	-	-	-	-	-

Table 74. NMC non-flaming yields

	% Volume									Mass Produced [mg/wh]										
Source	**HF**	**CO**	**CO_2**	**HBr**	**HCl**	**NO_2**	**SO_2**	**HCN**	**NH_3**	**Benzene**	**HF**	**CO**	**CO_2**	**HBr**	**HCl**	**NO_2**	**SO_2**	**HCN**	**NH_3**	**Benzene**
Amano (2023)	-	-	-	-	-	-	-	-	-	-	0.001	1.2	0.0	-	-	-	-	0.005	-	-
Amano (2023)	-	-	-	-	-	-	-	-	-	-	0.002	3.4	0.0	-	-	-	-	0.01	-	-
Amano (2023)	-	-	-	-	-	-	-	-	-	-	0.004	5.0	6.4	-	-	-	-	0.03	-	-

Archibald (2021)	-	21.3	29.9	-	-	-	-	-	-	-	-	170.6	376.2	-	-	-	-	-	-	-
Bordes (2022)	-	-	-	-	-	-	-	-	-	-	1.0	77.1	358.6	-	-	-	-	-	-	-
DNV (2019)	0.7	29.2	19.6	-	9.7	-	-	0.0	-	4.1	11.6	675.0	711.9	-	-	-	-	0.0	-	264.3
DNV (2019)	0.1	19.0	65.9	-	0.2	-	-	0.0	-	1.9	0.8	213.8	1165	-	-	-	-	0.0	-	59.6
Essl (2020a)	0.0	17.0	38.0	-	-	-	-	-	-	-	0.0	77.6	273.1	-	-	-	-	-	-	-
Essl (2020b)	0.0	26.0	30.0	-	-	-	-	-	-	-	0.0	141.2	256.5	-	-	-	-	-	-	-
Essl (2020b)	0.0	33.0	20.0	-	-	-	-	-	-	-	0.0	319.0	303.7	-	-	-	-	-	-	-
Essl (2020b)	0.0	22.0	30.0	-	-	-	-	-	-	-	0.0	131.0	281.0	-	-	-	-	-	-	-
Essl (2020b)	0.0	30.0	21.0	-	-	-	-	-	-	-	0.0	163.0	179.6	-	-	-	-	-	-	-
Essl (2020b)	0.0	30.0	20.0	-	-	-	-	-	-	-	0.0	275.9	288.9	-	-	-	-	-	-	-
Essl (2020b)	0.0	23.0	24.0	-	-	-	-	-	-	-	0.0	141.2	231.5	-	-	-	-	-	-	-
Golubkov (2014)	-	27.6	24.9	-	-	-	-	-	-	-	-	206.9	293.3	-	-	-	-	-	-	-
Golubkov (2014)	-	13.0	41.2	-	-	-	-	-	-	-	-	95.2	474.0	-	-	-	-	-	-	-
Huang (2020)	-	-	-	-	-	-	-	-	-	-	-	19.1	149.4	-	-	-	30.8	-	1.7	-
Sturk (2019)	-	-	-	-	-	-	-	-	-	-	14.3	-	-	-	-	-	-	-	-	-
Willstrand (2023)	0.0	-	-	-	0.0	0.0	0.0	0.0	-	-	-	-	-	-	-	-	-	-	-	-
Willstrand (2023)	0.0	44.0	22.0	-	0.0	0.0	0.0	0.0	-	-	-	-	-	-	-	-	-	-	-	-
Willstrand (2023)	0.0	36.0	28.0	-	0.0	0.0	0.0	0.0	-	-	-	-	-	-	-	-	-	-	-	-

Willstrand (2023)	0.0	26.0	48.0	-	0.0	0.0	0.0	0.0	-	-	-	-	-	-	-	-	-	-	-	-
Willstrand (2023)	0.0	13.0	58.0	-	0.0	0.0	0.0	0.0	-	-	-	-	-	-	-	-	-	-	-	-
Yang (2022)	0.0	32.4	35.3	-	-	-	-	-	-	-	0.0	149.8	204.7	-	-	-	-	-	-	-
Yang (2022)	0.0	29.6	28.1	-	-	-	-	-	-	-	0.0	201.7	296.5	-	-	-	-	-	-	-
Yang (2022)	0.0	60.3	13.0	-	-	-	-	-	-	-	0.0	410.1	143.2	-	-	-	-	-	-	-
Zhang (2019)	-	-	-	-	-	-	-	-	-	-	-	158.2	211.2	-	0.02	-	-	-	-	0.9

Table 75. LFP flaming yields

	Mass Produced [mg/g]										Mass Produced [mg/Wh]									
Source	**HF**	**CO**	**CO_2**	**Br**	**Cl**	**NO_2**	**SO_2**	**HCN**	**NH_3**	**Benzene**	**HF**	**CO**	**CO_2**	**Br**	**Cl**	**NO_2**	**SO_2**	**HCN**	**NH_3**	**Benzene**
Andersson (2013)	14.2	-	-	-	-	-	-	-	-	-	43.8	-	-	-	-	-	-	-	-	-
Andersson (2013)	18.4	-	-	-	-	-	-	-	-	-	56.3	-	-	-	-	-	-	-	-	-
Andersson (2013)	16.7	-	-	-	-	-	-	-	-	-	50.9	-	-	-	-	-	-	-	-	-
Andersson (2013)	32.0	-	-	-	-	-	-	-	-	-	100.9	-	-	-	-	-	-	-	-	-
Andersson (2013)	39.3	-	-	-	-	-	-	-	-	-	124.1	-	-	-	-	-	-	-	-	-
Andersson (2013)	15.2	-	-	-	-	-	-	-	-	-	23.9	-	-	-	-	-	-	-	-	-
DNV (2019)	-	-	-	-	-	-	-	-	-	-	9.4	499.1	3293	-	-	320.3	-	0.0	-	0.0
DNV (2019)	-	-	-	-	-	-	-	-	-	-	36.8	161.7	789.1	-	-	115.1	-	8.3	-	12.0

Larsson (2016)	15.2	-	-	-	-	-	-	-	-	-	23.9	-	-	-	-	-	-	-	-	-
Larsson (2016)	7.1	-	-	-	-	-	-	-	-	-	12.0	-	-	-	-	-	-	-	-	-
Larsson (2016)	18.7	-	-	-	-	-	-	-	-	-	57.6	-	-	-	-	-	-	-	-	-
Larsson (2017)	-	-	-	-	-	-	-	-	-	-	167.2	-	-	-	-	-	-	-	-	-
Larsson (2017)	-	-	-	-	-	-	-	-	-	-	53.6	-	-	-	-	-	-	-	-	-
Larsson (2017)	-	-	-	-	-	-	-	-	-	-	141.1	-	-	-	-	-	-	-	-	-
Larsson (2017)	-	-	-	-	-	-	-	-	-	-	23.9	-	-	-	-	-	-	-	-	-
Larsson (2017)	-	-	-	-	-	-	-	-	-	-	52.3	-	-	-	-	-	-	-	-	-
Lecocq (2016)	-	-	-	-	-	-	-	-	-	-	49.3	87.1	-	-	-	-	0.0	-	-	-
Lecocq (2016)	-	-	-	-	-	-	-	-	-	-	84.8	71.0	-	-	-	-	0.0	-	-	-
Lecocq (2016)	-	-	-	-	-	-	-	-	-	-	104.0	56.0	-	-	-	-	0.0	-	-	-
Lecocq (2016)	-	-	-	-	-	-	-	-	-	-	2.4	66.4	-	-	-	-	28.1	-	-	-
Lecocq (2016)	-	-	-	-	-	-	-	-	-	-	3.3	46.9	-	-	-	-	33.8	-	-	-
Lecocq (2016)	-	-	-	-	-	-	-	-	-	-	11.2	26.0	-	-	-	-	47.6	-	-	-
Liu (2020)	2.9	30.2	1518	-	-	-	-	-	-	-	4.1	42.3	2126	-	-	-	-	-	-	-
Liu (2020)	6.8	31.9	1170	-	-	-	-	-	-	-	10.8	50.7	1858	-	-	-	-	-	-	-
Liu (2020)	19.2	41.5	41.5	-	-	-	-	-	-	-	37.1	80.0	80.0	-	-	-	-	-	-	-
Liu (2021)	1.7	3.6	731.9	-	0.8	0.4	1.9	-	0.5	-	2.1	4.4	884.3	-	0.9	0.4	2.2	-	0.6	-

Liu (2021)	2.8	6.0	784.0	-	0.7	0.5	2.3	-	0.5	-	3.6	7.6	993.6	-	0.9	0.6	2.9	-	0.6	-
Liu (2021)	7.1	10.8	1482	-	0.7	2.3	3.8	-	0.5	-	10.4	15.8	2163	-	1.0	3.4	5.6	-	0.7	-
Meng (2020)	-	-	-	-	-	-	-	-	-	-	4.9	56.8	1931	-	-	-	-	-	-	-
Meng (2020)	-	-	-	-	-	-	-	-	-	-	17.3	104.9	1821	-	-	-	-	-	-	-
Meng (2020)	-	-	-	-	-	-	-	-	-	-	28.4	34.6	1559	-	-	-	-	-	-	-
Sturk (2015)	-	-	-	-	-	-	-	-	-	-	67.0	-	-	-	-	-	-	-	-	-
Sturk (2015)	-	-	-	-	-	-	-	-	-	-	40.2	-	-	-	-	-	-	-	-	-
Sturk (2015)	-	-	-	-	-	-	-	-	-	-	110.7	-	-	-	-	-	-	-	-	-
Sturk (2015)	-	-	-	-	-	-	-	-	-	-	50.0	-	-	-	-	-	-	-	-	-
Sturk (2015)	-	-	-	-	-	-	-	-	-	-	104.5	-	-	-	-	-	-	-	-	-
Sturk (2015)	-	-	-	-	-	-	-	-	-	-	107.1	-	-	-	-	-	-	-	-	-
Sturk (2015)	-	-	-	-	-	-	-	-	-	-	127.7	-	-	-	-	-	-	-	-	-
Sturk (2015)	-	-	-	-	-	-	-	-	-	-	167.9	-	-	-	-	-	-	-	-	-
Sturk (2015)	-	-	-	-	-	-	-	-	-	-	183.5	-	-	-	-	-	-	-	-	-

Table 76. NMC flaming yields

	Mass Produced [mg/g]										Mass Produced [mg/Wh]									
Source	**HF**	**CO**	**CO_2**	**HBr**	**HCl**	**NO_2**	**SO_2**	**HCN**	**NH_3**	**Benzene**	**HF**	**CO**	**CO_2**	**HBr**	**HCl**	**NO_2**	**SO_2**	**HCN**	**NH_3**	**Benzene**

Amano (2023)	-	-	-	-	-	-	-	-	-	-	0.01	45.7	365.0	-	-	-	-	0.1	-	-
Amano (2023)	-	-	-	-	-	-	-	-	-	-	0.01	59.5	663.5	-	-	-	-	0.1	-	-
Amano (2023)	-	-	-	-	-	-	-	-	-	-	-	17.3	-	-	-	-	-	0.1	-	-
Amano (2023)	-	-	-	-	-	-	-	-	-	-	-	16.3	-	-	-	-	-	0.1	-	-
Amano (2023)	-	-	-	-	-	-	-	-	-	-	-	59.2	22.3	-	-	-	-	0.3	-	-
Amano (2023)	-	-	-	-	-	-	-	-	-	-	-	49.0	-	-	-	-	-	0.1	-	-
Amano (2023)	-	-	-	-	-	-	-	-	-	-	-	49.8	-	-	-	-	-	0.1	-	-
Amano (2023)	-	-	-	-	-	-	-	-	-	-	-	205.0	-	-	-	-	-	0.1	-	-
Amano (2023)	-	-	-	-	-	-	-	-	-	-	-	147.8	-	-	-	-	-	0.3	-	-
Amano (2023)	-	-	-	-	-	-	-	-	-	-	-	134.7	-	-	-	-	-	0.2	-	-
Amano (2023)	-	-	-	-	-	-	-	-	-	-	-	160.7	-	-	-	-	-	0.4	-	-
Blum & Long (2016)	-	-	-	-	-	-	-	-	-	-	0.0	-	-	-	-	-	-	-	-	-
Bordes (2022)	-	-	-	-	-	-	-	-	-	-	6.7	109.5	2797	-	-	5.7	-	-	-	-
Bordes (2022)	-	-	-	-	-	-	-	-	-	-	16.2	67.6	-	-	-	2.4	-	-	-	-
DNV (2019)	-	-	-	-	-	-	-	-	-	-	2.1	111.0	616.8	-	-	-	-	0.0	-	29.9
DNV (2019)	-	-	-	-	-	-	-	-	-	-	0.7	345.5	612.3	-	-	-	-	0.0	-	120.4
DNV (2019)	-	-	-	-	-	-	-	-	-	-	2.1	371.1	393.3	-	-	-	-	0.0	-	141.3
Forestier (2020)	-	-	-	-	-	-	-	-	-	-	9.3	111.1	463.0	-	-	-	-	-	-	-

Huang (2020)	-	-	-	-	-	-	-	-	-	-	-	133.3	341.3	-	-	-	15.2	-	0.9	-
Huang (2021)	0.8	19.7	423.3	-	0.4	-	-	-	0.0	-	2.0	47.5	1023	-	0.9	-	-	-	0.0	-
Sturk (2015)	-	-	-	-	-	-	-	-	-	-	14.5	-	-	-	-	-	-	-	-	-
Sturk (2015)	-	-	-	-	-	-	-	-	-	-	6.2	-	-	-	-	-	-	-	-	-
Sturk (2015)	-	-	-	-	-	-	-	-	-	-	11.3	-	-	-	-	-	-	-	-	-
Sturk (2015)	-	-	-	-	-	-	-	-	-	-	8.7	-	-	-	-	-	-	-	-	-
Sturk (2015)	-	-	-	-	-	-	-	-	-	-	18.9	-	-	-	-	-	-	-	-	-
Wilstrand (2020)	-	-	-	-	-	-	-	-	-	-	29.0	29.8	-	0.6	1.3	-	-	-	-	-
Wilstrand (2020)	-	-	-	-	-	-	-	-	-	-	41.7	11.7	3917	0.1	1.6	1.8	15.0	-	-	-
Wilstrand (2020)	-	-	-	-	-	-	-	-	-	-	35.0	6.0	-	-	1.7	0.9	18.3	-	-	-
Wilstrand (2020)	-	-	-	-	-	-	-	-	-	-	36.7	1.0	3100	-	-	-	-	-	-	-
Wilstrand (2020)	-	-	-	-	-	-	-	-	-	-	30.3	1.3	-	-	-	-	-	-	-	-
Wilstrand (2020)	-	-	-	-	-	-	-	-	-	-	23.3	0.7	-	-	-	-	-	-	-	-
Wilstrand (2020)	-	-	-	-	-	-	-	-	-	-	26.7	1.3	-	-	-	-	-	-	-	-
Wilstrand (2020)	-	-	-	-	-	-	-	-	-	-	32.0	2.0	-	-	-	-	-	-	-	-
Wilstrand (2020)	-	-	-	-	-	-	-	-	-	-	34.0	1.3	-	-	-	-	-	-	-	-
Willstrand (2023)	-	-	-	-	-	-	-	-	-	-	4.2	-	-	-	-	-	-	-	-	-
Yuan (2020)	-	-	-	-	-	-	-	-	-	-	-	316.4	216.9	-	-	-	-	-	-	-
Yuan (2020)	-	-	-	-	-	-	-	-	-	-	-	358.8	370.4	-	-	-	-	-	-	-

Zhang (2022)	7.5	30.1	315.8	-	-	-	-	-	-	-	6.8	27.0	283.8	-	-	-	-	-	-	-
Zhang (2022)	7.0	45.8	45.8	-	-	-	-	-	-	-	13.5	87.8	87.8	-	-	-	-	-	-	-

7.2. AEGL-1 Justifications

The following justification for the benzene AEGL-1 values is an excerpt from the Committee on Acute Exposure Guideline Levels (2009).

"Although CNS effects of benzene are already known for over 100 years, very little is known about the time-concentration-effect relationship of slight CNS effects due to benzene exposure in humans, and no quantitative point of departure is available for a solid PBPK modeling. Although the study by Srbova et al. (1950) has some weaknesses (no details on all individual exposures and time durations, the lack of symptoms was reported by a single remark, no active investigation of health effects), the 110 ppm level for 2h is taken as a NOEL for CNS effects. This is the starting point for AEGL-1 development. This NOEL appears to be supported by the fact that a substantial number of volunteers was exposed in a controlled or occupational setting to levels of 1 – 76 ppm for 7h TWA (Inoue et al., 1986; 64 men, 88 women, occupational), 32 ppm ± 25 ppm for 8h TWA (Inoue et al., 1988; 65 workers, occupational) or 19-125 ppm for 6-8h (Hunter and Blair, 1972; male laboratory staff, controlled exp.) although none of these studies actually included statements on health effects. Because CNS effects are the consequence of systemic benzene exposure, time extrapolation should be applied. Based on the experiments described by Von Oettingen (1940) with cats, a n-value of 1 was identified for light and deep narcosis in cats (see section 6.2). Although these data from cats are from an old experiment and details about the experiment are lacking, the extensive number of concentrations and time points reported provides sufficient confidence in the results indicating that using N=3 for extrapolation to short time periods is too conservative. Therefore, time extrapolation is performed using N=1 and N=2 for longer and shorter time periods respectively. Because human data are used, the interspecies uncertainty factor is 1.

The intraspecies uncertainty factor is 3 because it has been found from experience with anesthetic gases that CNS depression does no vary by more than a factor 2-3 between groups in the population."

The following justification for the HBr AEGL-1 values is an excerpt from the Committee on Acute Exposure Guideline Levels (2014).

"The threshold for nasal irritation of 3ppm in human subjects exposed to HBr for several minutes (CT Department of Health, unpublished data, 1955, as cited in ACGIH 2002) was selected as the basis for the AEGL-1 values. That concentration was considered to be a threshold for notable discomfort, as only one individual was affected at that concentration. The 3 ppm point-of-departure was divided by an intraspecies uncertainty factor of 3, because response to sensory irritation is not expected to vary greatly among individuals (NRC 2001). A factor of 3 was considered sufficient because the effect of slight irritation is below the definition of AEGL-1. In addition, an intraspecies uncertainty factor of 3 was used to derive AEGL values for the related compounds HCl and HF, which have the same mode of action as HBr (NRC 2004). It is reasonable to use the same uncertainty factors for a class of chemicals whose mode of action is the same. Finally, the uncertainty factor used to derive the AEGL-1 values for HBr is believed to be protective of asthmatic individuals on the basis of comparison of the AEGL-1 value for HBr (1.0 ppm) with the AEGL-1 value for HCl (1.8 Acute Exposure Guideline Levels ppm); the latter is based on a no-effect level for irritation in exercising asthmatics. There is evidence that HBr is of similar toxicity to HCl; thus, the lower AEGL-1 values for HBr are considered to be protective of asthmatics on the basis of data on HCl. Because irritation depends on concentration rather than time, and adaptation to slight irritation occurs (Dalton 2001), 1.0 ppm was used for all of the AEGL-1

exposure durations (see Table 8-8). Derivation of the AEGL-1 values for HBr are presented in Appendixes A and D, and a category plot of the toxicity data for HBr in relation to AEGL values is presented in Appendix B. Although the AEGL-1 values for HBr are based on data presented in a secondary source, the values obtained from the data are supported by comparison with the related compounds HF and HCl. The AEGL-1 values for HF (1.0 ppm) and HCl (1.8 ppm) are equal to or higher than the values obtained for HBr using data from Connecticut State Department of Health (unpublished data, 1955, as cited in ACGIH 2002). Thus, if AEGL-1 values for HBr were obtained by analogy to these related compounds, the same or higher AEGL-1 values would be derived."

The following justification for the HCl AEGL-1 values is an excerpt from the Subcommittee on Acute Exposure Guideline Levels (2004).

"Because appropriate human data exist for exposure to HCl, they were used to identify AEGL-1 values. Exposure to HCl at 1.8 ppm for 45 min resulted in a no-observed-adverse-effect level (NOAEL) in 10 exercising young adult asthmatic subjects (Stevens et al. 1992). Because exercise will increase HCl uptake and exacerbate irritation, those asthmatic subjects are considered a sensitive subpopulation. Therefore, because the test subjects were a sensitive subpopulation and the end point was essentially a no-effect level, no uncertainty factory (UF) was applied to account for sensitive human subpopulations. Adequate human data were available, so no UF was applied for animal to human extrapolation. The no-effect level was held constant across the 10- and 30-min and 1-, 4-, and 8-h exposure time points. That approach was considered appropriate because mild irritant effects generally do not vary greatly over time, and the end point of a no-effect level in a sensitive population is inherently conservative."

The following justification for the HCN AEGL-1 values is an excerpt from the Subcommittee on Acute Exposure Guideline Levels (2002).

"The AEGL-1 is based on monitoring studies in which the preponderance of data as a weight-of-evidence consideration indicates that an 8-h exposure to 1 ppm would be without adverse effects for the general population…The AEGL-1 was derived from a consideration of the dose-response data, which were obtained from all of the monitoring studies and subsequently time scaled to the shorter exposure durations. Although the exposures were of chronic duration in the monitoring studies, they represent the best available human data. Symptoms observed during chronic exposures should represent the greatest potential response. An 8-h exposure duration was selected as the basis for AEGL development. Mild headache is a symptom of exposure that meets the definition of an AEGL-1. Dividing the 8-h concentration of 5 ppm of the Grabois (1954), Hardy et al. (1950), or Maehly and Swensson (1970) study by an intraspecies uncertainty factor (UF) of 3 or dividing the 1-h concentration of 8 ppm of the El Ghawabi et al. (1975) study by an intraspecies UF of 3 results in very similar AEGL-1 values. The resulting 8-h value of 1.7 ppm is also similar to the 8-h no-effect concentration of 1 ppm in the Leeser et al. (1990) study, where no UF was applied. UFs are generally applied to the highest NOAELs or lowest LOAELs. A UF was not applied to the Leeser et al. (1990) study because it was the lowest NOAEL. No specific susceptible populations were identified during numerous occupational monitoring studies or during the clinical use of nitroprusside solutions to control hypertension. Thus, potential differences in susceptibility among humans are not expected to exceed 3-fold. All individuals, including infants, possess large amounts of the cyanide detoxifying enzyme rhodanese (as well as other detoxifying enzymes) and normally have adequate amounts of sulfur-containing compounds.

The 8-h no-effect mean geometric concentration of 1 ppm (with excursions up to 6 ppm) from the Leeser et al. (1990) study was used as the basis for time scaling the AEGL-1 values. This study was chosen because it was well conducted: all workers had full medical examinations and routine blood tests, including measurements of blood cyanide and carboxyhemoglobin. Atmospheric HCN concentrations were monitored in the plant several times during the year. Because of the extrapolation from a long-term exposure, the 8-h value of 1 ppm was time scaled to the other exposure durations using the relationship C3 × t = k where k = 480 ppm 3 @min. In order to stay below the highest measured concentration from personal samplers, at 3.3 ppm in the Leeser et al. (1990) study, the 10-min value was set equal to the 30-min value."

The following justification for the HF AEGL-1 values is an excerpt from the Subcommittee on Acute Exposure Guideline Levels (2004).

"The AEGL-1 was based on an exposure at 3 parts per million (ppm) (range, 0.85-2.93 ppm) for 1 hour (h), which was the threshold for pulmonary inflammation, as evidenced by an increase in the percentage of several inflammatory parameters such as CD3 cells and myeloperoxidase in the bronchoalveolar lavage fluid of 20 healthy exercising adult subjects (Lund et al. 1999). There were no increases in neutrophils, eosinophils, protein, or methyl histamine at this or the next higher average exposure concentration of 4.7 ppm (range, 3.05-6.34 ppm). There were no changes in lung function and only minor symptoms of irritation at that concentration (Lund et al. 1997). Although healthy adults were tested, several individuals had increased immune factors, indicating atopy. The 3-ppm concentration was divided by an intraspecies uncertainty factor (UF) of 3 to protect susceptible individuals. Because there were no effects on respiratory parameters of healthy adults at concentrations up to 6.34 ppm in the Lund et al. (1997) study and at

concentrations up to 8.1 ppm for 6 h/day (d) with repeated exposures in a supporting study (Largent 1960, 1961), the calculated AEGL-1 values will be protective of asthmatic individuals. Although the Lund et al. (1999) study duration was only 1 h, the longer exposures at higher concentrations in the supporting study (Largent 1960, 1961), and the fact that adaptation to mild sensory irritation occurs, support application of the 1-ppm concentration for up to 8 h."

The following justification for the NH_3 AEGL-1 values is an excerpt from the Committee on Acute Exposure Guideline Levels (2008).

"Humans experience either faint or no irritation after exposure to ammonia at 30 ppm for 10 min (MacEwen et al. 1970); therefore, 30 ppm was used to derive AEGL-1 values. An interspecies uncertainty factor is not applied to these data because the AEGL value is based on human data. An intraspecies uncertainty factor of 1 was selected because ammonia is efficiently scrubbed in the upper respiratory tract, and if irritation occurs, it would be confined to the nasal cavity (and possibly the eyes). Nonatopic and atopic subjects, including asthmatics, responded similarly in a nasal airway resistance test when 100 ppm of ammonia was introduced into each nostril for up to 30 s (McLean et al. 1979); therefore, asthmatic individuals are not expected to respond differently than nonasthmatic individuals. Exercising subjects showed only a clinically nonsig nificant decrease in pulmonary function after exposure to higher concentrations of ammonia (Cole et al. 1977); therefore, exercise is not expected to cause an appreciable difference in effects experienced during exposure to AEGL-1 concentrations. The same value is proposed for 5, 30, 60, 240, and 480 min, because any effects that occur are not expected to become more severe with duration of exposure because adaptation occurs during prolonged exposure. AEGL-1 values are summarized in Table 2-9. The AEGL-1 value of 30 ppm for all time points is supported by observations that

humans reported similar intensities of response after exposure to 50 ppm for 10 min to 2 h (MacEwen et al. 1970; Verberk 1977)."

The following justification for the NO_2 AEGL-1 values is an excerpt from the Committee on Acute Exposure Guideline Levels (2012).

"AEGL values were based on studies of NO_2, the predominant form of the nitrogen oxides, and values are considered applicable to all nitrogen oxides. Values for N_2O_4 in units of ppm have been calculated on a molar basis. Because conversion to NO_2 is expected to occur in the atmosphere, and because NO_2 is more toxic than NO, the AEGL values for NO_2 are recommended for use with emergency planning for NO. The National Advisory Committee recognizes, however, that short-term exposures to NO below 80 ppm should not constitute a health hazard.... For AEGL-1, a concentration of 0.5 ppm was adopted for all time points. Although the response of asthmatics to NO2 is variable, asthmatics were identified as a potentially susceptible population. The evidence indicates that some asthmatics exposed to NO_2 at 0.3-0.5 ppm might respond with either subjective symptoms or slight changes in pulmonary function that are not clinically significant. In contrast, some asthmatics did not respond to NO_2 at concentrations of 0.5-4 ppm. Because of the weight of evidence, the study by Kerr et al. (1978, 1979) was considered the most appropriate for derivation of AEGL-1 values. They reported that 7/13 asthmatics experienced slight burning of the eyes, slight headache, and chest tightness or labored breathing with exercise when exposed at 0.5 ppm for 2 h; at this concentration, the odor of NO_2 was perceptible but the subjects became unaware of it after about 15 min. No changes in any pulmonary function tests were found immediately following the chamber exposure (Kerr et al. 1978, 1979). Therefore, 0.50 ppm was considered a no-adverse-effect level for the asthmatic population. Since asthmatics are potentially the most

susceptible population, no uncertainty factor was applied. Time scaling was not performed because adaptation to mild sensory irritation occurs. In addition, animal responses to NO_2 exposure have demonstrated a much greater dependence on concentration than on time; therefore, extending the 2-h concentration to 8 h should not exacerbate the human response."

The following justification for the SO_2 AEGL-1 values is an excerpt from the Committee on Acute Exposure Guideline Levels (2010).

"AEGL-1 values were based on the weight-of-evidence from human asthmatic data suggesting that 0.20 ppm may be a NOEL for bronchoconstriction in exercising asthmatics. No treatment-related effects were noted in asthmatics exposed to 0.2 ppm for 5 min (Linn et al. 1983b), 0.25 ppm for 10-40 min (Schacter et al. 1984), 0.25 ppm for 75 min (Roger et al. 1985), 0.5 ppm for 10-40 min (Schacter et al. 1984), or 0.5 ppm for 30 min (Jorres and Magnussen 1990). However, an increase in airway resistance (S_{Raw}) of 134-139% was observed in exercising asthmatics exposed to 0.25 ppm for 5 min (Bethel et al. 1985); the increase in S_{Raw} in this study, but not in the other studies, may be attributed to the lower relative humidity (36%) in the Bethel et al. (1985) study compared to the other studies (70-85%). No uncertainty factors were applied because the weight of evidence approach utilized studies from a sensitive human population, exercising asthmatics. The role of exposure duration to the magnitude of SO_2-induced bronchoconstriction in asthmatics appears to decrease with extended exposure. For example, asthmatics exposed to 0.75 ppm SO_2 for 3-h exhibited increases in S_{Raw} of 322% 10-min into exposure, 233% 20-min into the exposure, 26% 1-hr into the exposure, 5% 2-h into the exposure, and a decrease of 12% at the end of the 3-h exposure period. These data suggest that a major portion of the SO_2-induced bronchoconstriction occurs within 10-min and increases minimally or resolves beyond 10-min of

exposure. Therefore, AEGL-1 values for SO_2 were held constant across all time points. Exposure to concentrations at the level of derived AEGL-1 values is expected to have no effect in healthy individuals, but the concentrations are consistent with the definition of AEGL-1 for asthmatic individuals."

7.3. IDLH Justifications

The following justification for the benzene IDLH value is an excerpt from the NIOSH IDLH.

"The chosen IDLH is based on the report in Patty [1963] that for man, a single exposure to 3,000 ppm is endurable for 0.5 to 1 hour [Flury 1928]."

The following justification for the CO IDLH value is an excerpt from the NIOSH IDLH.

"The chosen IDLH is based on the statement by Patty [1963] that a 1-hour exposure to 1,000 to 1,200 ppm would cause unpleasant, but no dangerous symptoms [Henderson et al. 1921]. Patty [1963] also reported that 1,500 to 2,000 ppm might be a dangerous concentration for an exposure of 1 hour [Henderson et al. 1921]."

The following justification for the CO_2 IDLH value is an excerpt from the NIOSH IDLH.

"The chosen IDLH is based on the statements by ACGIH [1971] that a 30-minute exposure at 50,000 ppm produces signs of intoxication, and a few minutes of exposure at 70,000 ppm and 100,000 ppm produces unconsciousness [Flury and Zernik 1931]. AIHA [1971] reported that 100,000 ppm is the atmospheric concentration immediately dangerous to life. In addition, Hunter [1975] noted that exposure to 100,000 ppm for only a few minutes can cause loss of consciousness."

The following justification for the HBr IDLH value is an excerpt from the NIOSH IDLH.

"Hydrogen bromide is an extremely irritating and corrosive gas. The chosen IDLH is based on an analogy with bromine. According to ILO [1971], however, bromine produces a more marked toxic action. AIHA [1958] reported that for humans, 40 to 60 ppm bromine is dangerous for short exposure [Henderson and Haggard 1943]. Because hydrogen bromide is considered less irritating than bromine, an IDLH of 50 ppm is chosen."

The following justification for the HCl IDLH value is an excerpt from the NIOSH IDLH.

"The chosen IDLH is based on the statements by Patty [1963] that according to Matt [1889] as cited in Flury and Zernik [1931], work is impossible when one inhales air containing hydrogen chloride in concentrations of 75 to 150 mg/m^3 (50 to 100 ppm); work is difficult but possible when the air contains concentrations of 15 to 75 mg/m^3 (10 to 50 ppm); and work is undisturbed at the concentration of 15 mg/m^3 (10 ppm)."

The following justification for the HCN IDLH value is an excerpt from the NIOSH IDLH.

"The chosen IDLH is based on the statements by Patty [1963] that 45 to 54 ppm is 'tolerated by man for 0.5 to 1 hour without immediate or late effects; 110 to 135 ppm, however, may be fatal after 0.5 to 1 hour or later, or dangerous to life [Flury and Zernik 1931; Dudley et al. 1942].'"

The following justification for the HF IDLH value is an excerpt from the NIOSH IDLH.

"The chosen IDLH is based on the statement by Patty [1963] that 24 mg/m^3 (30 ppm) was tolerated by animals for a total of 41 hours without a fatality [Machle et al. 1934]. A concentration of 50 ppm is obviously too high to be selected as the IDLH, because Deichmann and Gerarde [1969] stated that 50 ppm may be fatal when inhaled for 30 to 60 minutes."

The following justification for the NH_3 IDLH value is an excerpt from the NIOSH IDLH.

"The chosen IDLH is based on the statement by AIHA [1971] that 300 to 500 ppm for 30 to 60 minutes have been reported as a maximum short exposure tolerance [Henderson and Haggard 1943]. AIHA [1971] also reported that 5,000 to 10,000 ppm are reported to be fatal [Mulder and Van der Zahm 1967] and exposures for 30 minutes to 2,500 to 6,000 ppm are considered dangerous to life [Smyth 1956]."

The following justification for the NO_2 IDLH value is an excerpt from NIOSH (2017).

"Nitrogen dioxide is an irritant to the mucous membranes and has been shown to cause coughing and dyspnea during exposure. Severe exposure pulmonary edema with symptoms of chest pain, cough, dyspnea, and cyanosis have been reported [NIOSH 1976; Douglas et al. 1989]. Human data indicate that acute inhalation exposures may induce potential escape-impairing effects of dyspnea, cyanosis, and pulmonary edema [Henschler et al. 1960; Norwood et al. 1969; Morley and Silk 1970]. Exposure to nitrogen dioxide at 30 ppm for 70 minutes resulted in a severe cough and an increased burning sensation of the upper respiratory tract that progressed with continued exposures to include the lower section of the airways and in the chest [Henschler et al. 1960]. These effects can be considered a LOAEL and serve as the basis of the IDLH value for nitrogen dioxide. Duration adjustment (see Table 5) resulted in the calculation of a 30-minute equivalent concentration of 38 ppm. Application of a composite uncertainty factor of 3 to account for human variability yielding an IDLH value 13 ppm for nitrogen dioxide."

The following justification for the SO_2 IDLH value is an excerpt from the NIOSH IDLH.

"The chosen IDLH is based on the statement by AIHA [1955] that 50 to 100 ppm is considered the maximum concentration for exposures of 0.5 to 1 hour [Henderson and Haggard 1943]. With regard to the atmospheric concentration immediately hazardous to life, AIHA [1955] reported that 400 to 500 ppm is considered dangerous for even short periods of exposure [Henderson and Haggard 1943] and that exposure to unendurable concentrations is not necessarily hazardous if escape is made within a few minutes."

7.4. Exposure Limit Distances

Table 77 through Table 80 present the distances at which exposure limits are exceeded for the non-flaming scenarios. Table 81 through Table 84 present the distances at which exposure limits are exceeded for the flaming scenarios. The furthest distance produced for each scenario is highlighted in yellow.

Table 77. LFP non-flaming thermal runaway simulation results for IDLH limits

Non-Flaming LFP			IDLH Distances [m]						
Temperature [C]	Wind Speed [m/s]	Duration [hr]	HF	CO	CO_2	NO_2	HCl	HCN	Benzene
7	2	6	0.5[a]	0	0	41.75	0	0	0
7	5	6	5	0	0	62.25	0	0	0
7	10	6	0	0	0	28.75	0	0	0
7	2	12	0.5[a]	0	0	34.25	0	0	0
7	5	12	0	0	0	27.75	0	0	0
7	10	12	0	0	0	11.25	0	0	0
22	2	6	0.5[a]	0	0	50.75	0	0	0
22	5	6	5.5	0	0	63.75	0	0	0
22	10	6	0	0	0	28.75	0	0	0
22	2	12	0.375[a]	0	0	45.75	0	0	0
22	5	12	0	0	0	29.25	0	0	0
22	10	12	0	0	0	12.25	0	0	0
35	2	6	7.75	0	0	54.75	0	0	0
35	5	6	6.5	0	0	69.75	0	0	0
35	10	6	0	0	0	33.25	0	0	0

35	2	12	0.25[a]	0	0	39.75	0	0	0
35	5	12	0	0	0	27.75	0	0	0
35	10	12	0	0	0	12.50	0	0	0

a) Distance was evaluated at the sides of the BESS unit, not downwind

Table 78. LFP non-flaming thermal runaway simulation results for AEGL-1, ERPG-1, & TEEL-1 limits

Non-Flaming LFP			AEGL-1, ERPG-1, & TEEL-1 Distances [m]						
Temperature [C]	Wind Speed [m/s]	Duration [hr]	HF	CO	CO_2	NO_2	HCl	HCN	Benzene
7	2	6	117.25	0	0	200+	62.25	18.75	9.25
7	5	6	165.75	2.625	0	200+	100.25	19.75	10
7	10	6	119.25	0	0	200+	57.25	9	3.75
7	2	12	103.25	0	0	200+	56.75	12.5	6
7	5	12	113.75	0	0	200+	54.25	8.25	3.25
7	10	12	71.75	0	0	200+	48.75	2.625	0
22	2	6	114.25	0	0	200+	71.75	23.25	11.75
22	5	6	168.25	3.75	0	200+	103.75	20.25	10.75
22	10	6	121.75	0	0	200+	56.75	9.5	4
22	2	12	115.75	0	0	200+	65.25	15.25	8
22	5	12	119.75	0	0	200+	58.75	9.25	4.25
22	10	12	74.75	0	0	200+	24.25	2.75	0
35	2	6	139.75	0	0	200+	75.75	27.25	15.25
35	5	6	168.25	4.5	0	200+	107.75	22.75	11.5
35	10	6	125.25	0	0	200+	63.75	10.25	4.5
35	2	12	103.25	0	0	200+	64.25	15.75	7
35	5	12	124.25	0	0	200+	57.75	9	11.5
35	10	12	77.25	0	0	200+	25.75	3.5	0

Table 79. NMC non-flaming thermal runaway simulation results for IDLH limits

Non-Flaming NMC			IDLH Distances [m]					
Temperature [C]	Wind Speed [m/s]	Duration [hr]	HF	CO	CO_2	HCl	HCN	Benzene
7	2	0.5	0	0	0	0	0	0
7	5	0.5	0.25[a]	15.25	0	0	0	0.25[a]
7	10	0.5	0	20.25	0	0	0	0.25[a]
7	2	2	0	0	0	0	0	0
7	5	2	0	8.25	0	0	0	0
7	10	2	0	2.625	0	0	0	0

22	2	0.5	0	0	0	0	0	0
22	5	0.5	0.25[a]	17.75	0	0	0	0.25[a]
22	10	0.5	0	21.25	0	0	0	0.25[a]
22	2	2	0	0	0	0	0	0
22	5	2	0	9	0	0	0	0
22	10	2	0	3.5	0	0	0	0
35	2	0.5	0	0.25[a]	0	0	0	0
35	5	0.5	0.25[a]	21.75	0	0	0	0.25[a]
35	10	0.5	0	22.25	0	0	0	0.25[a]
35	2	2	0	0	0	0	0	0
35	5	2	0	9.75	0	0	0	0
35	10	2	0	3.5	0	0	0	0

a) Distance was evaluated at the sides of the BESS unit, not downwind

Table 80. NMC non-flaming thermal runaway simulation results for AEGL-1, ERPG-1, & TEEL-1 limits

Non-Flaming NMC			AEGL-1, ERPG-1, & TEEL-1 Distances [m]					
Temperature [C]	**Wind Speed [m/s]**	**Duration [hr]**	**HF**	**CO**	**CO_2**	**HCl**	**HCN**	**Benzene**
7	2	0.5	0	0	0	0	0	0
7	5	0.5	73.75	72.75	0	48.25	0	35.75
7	10	0.5	132.75	130.25	0	85.25	0	62.25
7	2	2	17.75	17.25	0	7.5	0	3.75
7	5	2	69.25	65.75	0	36.75	0	22.75
7	10	2	43.25	40.75	0	18.25	0	12
22	2	0.5	0	0	0	0	0	0
22	5	0.5	85.25	83.75	0	53.25	0	41.25
22	10	0.5	133.75	131.75	0	90.25	0	65.75
22	2	2	22.75	21.75	0	13.75	0	9.25
22	5	2	76.25	72.75	0	39.75	0	24.75
22	10	2	45.25	42.75	0	19.25	0	12.5
35	2	0.5	0	0	0	0	0	0
35	5	0.5	95.25	93.75	0	61.75	0	46.75
35	10	0.5	140.25	138.25	0	95.75	0	69.75
35	2	2	30.25	29.25	0	19.25	0	13.75
35	5	2	81.25	78.25	0	43.75	0	28.75
35	10	2	48.75	45.75	0	20.25	0	12.5

Table 81. LFP flaming thermal runaway simulation results for IDLH limits

Flaming LFP	IDLH Distances [m]

Temperature [C]	Wind Speed [m/s]	Duration [hr]	HF	CO	CO_2	NO_2	HCl	SO_2	NH_3
7	2	2	0	0	0	0	0	0	0
7	5	2	0.125[a]	0	0	0	0	0	0
7	10	2	1[a]	0	0	0.75[a]	0	0	0
7	2	4	0	0	0	0	0	0	0
7	5	4	0.125[a]	0	0	0	0	0	0
7	10	4	0.75[a]	0	0	0.5[a]	0	0	0
7	2	6	0	0	0	0	0	0	0
7	5	6	0	0	0	0	0	0	0
7	10	6	0.75[a]	0	0	0.5[a]	0	0	0
22	2	2	0	0	0	0	0	0	0
22	5	2	0.125[a]	0	0	0	0	0	0
22	10	2	1.125[a]	0	0	0.75[a]	0	0	0
22	2	4	0	0	0	0	0	0	0
22	5	4	0.125[a]	0	0	0	0	0	0
22	10	4	0.875[a]	0	0	0.5[a]	0	0	0
22	2	6	0	0	0	0	0	0	0
22	5	6	0.125[a]	0	0	0	0	0	0
22	10	6	0.75[a]	0	0	0	0	0	0
35	2	2	0	0	0	0	0	0	0
35	5	2	0.125[a]	0	0	0	0	0	0
35	10	2	1.125[a]	0	0	0.75[a]	0	0	0
35	2	4	0	0	0	0	0	0	0
35	5	4	0.125[a]	0	0	0	0	0	0
35	10	4	0.875[a]	0	0	0.5[a]	0	0	0
35	2	6	0	0	0	0	0	0	0
35	5	6	0.125[a]	0	0	0	0	0	0
35	10	6	0.75[a]	0	0	0.5[a]	0	0	0

a) Distance was evaluated at the sides of the BESS unit, not downwind

Table 82. LFP flaming thermal runaway simulation results for AEGL-1, ERPG-1, & TEEL-1 limits

Flaming LFP			AEGL-1, ERPG-1, & TEEL-1 Distances [m]					
Temperature [C]	Wind Speed [m/s]	Duration [hr]	HF	CO	CO_2	NO_2	HCl	NH_3
7	2	2	0	0	0	0	0	0
7	5	2	1.875	0	0	0	0	0
7	10	2	12.75	0	0	0	0	0
7	2	4	0	0	0	0	0	0
7	5	4	0.625	0	0	0	0	0

7	10	4	13.25	0	0	0	0	0
7	2	6	0	0	0	0	0	0
7	5	6	0.375	0	0	0	0	0
7	10	6	12.75	0	0	0	0	0
22	2	2	0	0	0	0	0	0
22	5	2	2	0	0	0	0	0
22	10	2	12.75	0	0	0	0	0
22	2	4	0	0	0	0	0	0
22	5	4	0.75	0	0	0	0	0
22	10	4	16.25	0	0	0	0	0
22	2	6	0	0	0	0	0	0
22	5	6	2.25	0	0	0	0	0
22	10	6	15.75	0	0	0	0	0
35	2	2	0	0	0	0	0	0
35	5	2	2	0	0	0	0	0
35	10	2	12.75	0	0	0.25	0	0
35	2	4	0	0	0	0	0	0
35	5	4	2	0	0	0	0	0
35	10	4	14.75	0	0	0	0	0
35	2	6	0	0	0	0	0	0
35	5	6	0.75	0	0	0	0	0
35	10	6	12.75	0	0	0	0	0

Table 83. NMC flaming thermal runaway simulation results for IDLH limits

Flaming NMC			IDLH Distances [m]								
Temp. [C]	Wind Speed [m/s]	Duration [hr]	HF	CO	CO_2	NO_2	HCl	HCN	HBr	SO_2	Benzene
7	2	2	0	0	0	0	0	0	0	0	0
7	5	2	0	0	0	0	0	0	0	0	0
7	10	2	1[a]	0	0	0.75[a]	0	0	0	0	0.5[a]
7	2	4	0	0	0	0	0	0	0	0	0
7	5	4	0	0	0	0	0	0	0	0	0
7	10	4	0.75[a]	0	0	0.5[a]	0	0	0	0	0.375[a]
7	2	6	0	0	0	0	0	0	0	0	0
7	5	6	0	0	0	0	0	0	0	0	0
7	10	6	0.625[a]	0	0	0.5[a]	0	0	0	0	0
22	2	2	0	0	0	0	0	0	0	0	0
22	5	2	0	0	0	0	0	0	0	0	0

22	10	2	1[a]	0	0	0.5[a]	0	0	0	0	0.375[a]
22	2	4	0	0	0	0	0	0	0	0	0
22	5	4	0	0	0	0	0	0	0	0	0
22	10	4	0.625[a]	0	0	0.5[a]	0	0	0	0	0.375[a]
22	2	6	0	0	0	0	0	0	0	0	0
22	5	6	0	0	0	0	0	0	0	0	0
22	10	6	0.625[a]	0	0	0.5[a]	0	0	0	0	0.375[a]
35	2	2	0	0	0	0	0	0	0	0	0
35	5	2	0	0	0	0	0	0	0	0	0
35	10	2	1[a]	0	0	0.75[a]	0	0	0	0.375[a]	0.375[a]
35	2	4	0	0	0	0	0	0	0	0	0
35	5	4	0	0	0	0	0	0	0	0	0
35	10	4	0.625[a]	0	0	0.5[a]	0	0	0	0	0
35	2	6	0	0	0	0	0	0	0	0	0
35	5	6	0	0	0	0	0	0	0	0	0
35	10	6	0.625[a]	0	0	0.5[a]	0	0	0	0	0

a) Distance was evaluated at the sides of the BESS unit, not downwind

Table 84. LFP flaming thermal runaway simulation results for AEGL-1, ERPG-1, & TEEL-1 limits

Flaming NMC			AEGL-1, ERPG-1, & TEEL-1 Distances [m]								
Temp. [C]	**Wind Speed [m/s]**	**Duration [hr]**	**HF**	**CO**	**CO_2**	**NO_2**	**HCl**	**HCN**	**HBr**	**SO_2**	**Benzene**
7	2	2	0	0	0	0	0	0	0	0	0
7	5	2	0	0	0	0	0	0	0	0	0
7	10	2	12	0	0	0.35	0	0	0	13.75	0
7	2	4	0	0	0	0	0	0	0	0	0
7	5	4	0	0	0	0	0	0	0	0	0
7	10	4	3.25	0	0	0	0	0	0	12.75	0
7	2	6	0	0	0	0	0	0	0	0	0
7	5	6	0	0	0	0	0	0	0	0	0
7	10	6	5	0	0	0	0	0	0	11.25	0
22	2	2	0	0	0	0	0	0	0	0	0
22	5	2	0	0	0	0	0	0	0	0	0
22	10	2	12.5	0	0	0.25	0	0	0	14.25	0
22	2	4	0	0	0	0	0	0	0	0	0
22	5	4	0	0	0	0	0	0	0	0	0
22	10	4	3.25	0	0	0	0	0	0	12.5	0
22	2	6	0	0	0	0	0	0	0	0	0
22	5	6	0	0	0	0	0	0	0	0	0

22	10	6	4.5	0	0	0	0	0	0	11.75	0
35	2	2	0	0	0	0	0	0	0	0	0
35	5	2	0	0	0	0	0	0	0	0.375	0
35	10	2	12.5	0	0	0.375	0	0	0	14.25	0
35	2	4	0	0	0	0	0	0	0	0	0
35	5	4	0	0	0	0	0	0	0	0	0
35	10	4	3.5	0	0	0	0	0	0	12.75	0
35	2	6	0	0	0	0	0	0	0	0	0
35	5	6	0	0	0	0	0	0	0	0	0
35	10	6	10.75	0	0	0	0	0	0	14.75	0

8. Bibliography

Aiuppa, A., Franco, A., von Glasow, R., Allen, A.G., D'Alessandro, W., Mather, T.A., Pyle, D.M., & Valenza, M. (2007). The tropospheric processing of acidic gases and hydrogen sulphide in volcanic gas plumes as inferred from field and model investigations. *Atmospheric Chemistry and Physics*, 7, 1441-1450.

Amano, K.O.A., Hahn, S.K., Tschirschwitz, R., Rappsilder, T., & Krause, U. (2022). An Experimental Investigation of Thermal Runaway and Gas Release of NMC Lithium-Ion Pouch Batteries Depending on the State of Charge Level. *Batteries*, 8, 41.

Amano, K.O.A., Hahn, S.K., Butt, N., Vorwerk, P., Gimadieva, E., Tschirschwitz, R., Rappsilder, T., & Krause, U. (2023). Composition and explosibility of gas emissions from lithium-ion batteries undergoing thermal runaway. *Batteries*, 9, 300.

Andersson, P., Blomqvist, P., Lorén, A., & Larsson, F. (2016). Using Fourier transform infrared spectroscopy to determine toxic gases in fires with lithium-ion batteries. *Fire and Materials*, 40(8), 999–1015.

Andersson, P., Brandt, J., & Willstrand, O. (2016). Full scale fire-test of an electric hybrid bus. SP Technical Research Institute of Sweden, Borås, Sweden, 2017.

Andrea, FDS Mesh size calculator, FDS Tutorial, March 17, 2021, retrieved from https://fdstutorial.com/fds-mesh-size-calculator/

Archibald, E.J. (2021). Fire & Explosion Hazards due to Thermal Runaway Propagation in Lithium-Ion Battery Systems. Doctoral dissertation, University of Texas at Austin.

Barowy, A., Klieger, A., Regan, J., & McKinnon, M. (2021). UL 9540A Installation Level Tests with Outdoor Lithium-ion Energy Storage System Mockups. Underwriter's Laboratory.

Bergstrom, U., Gustafsson, A., Hagglund, L., Lejon, C., Sturk, D., & Tengel, T. (2021). Vented gases and aerosol of automotive Li-ion LFP and NMC batteries in humidified nitrogen under thermal load.

Biteau, H., Fuentes, A., Marlair, G., Brohez, S., & Torero, J.L. (2009). Ability of the Fire Propagation Apparatus to characterise the heat release rate of energetic materials. *Journal of Hazardous Materials*, 166(2-3), 916-924.

Biteau, H., Steinhaus, T., Bal, N., Torero, J.L., Marlair, G., Schemel, C., & Simeoni, A. (2008). Calculation methods for the heat release rate of materials of unknown composition. *Fire Safety Science*,9, 1165-1176.

Blomqvist, P., Persson, B., & Simonson, M. (2007). Fire Emissions of Organics into the Atmosphere. *Fire Technology*, 43, 213-231.

Blum, A., Bensen, T., Rogers, P., Grant, C., & Hough, G. (2022). Victorian Big Battery Fire: July 20, 2021. Fisher Engineering. Energy Safety Response Group (ESRG).

Blum, A. F., & Long, R. T. (2016). *Fire hazard assessment of lithium ion battery energy storage systems*. SpringerBriefs in Fire.

Bordes, A., Marlair, G., Zantman, A., Herreyre, S., Papin, A., Desprez, P., & Lecocq, A. (2022). New Insight on the Risk Profile Pertaining to Lithium-Ion Batteries Under Thermal Runaway as Affected by System Modularity and Subsequent Oxidation Regime. *Journal of Energy Storage*, 52, Part B, 104790.

Bowes, M., & Rogers, P. (2022). Cranberry Point Energy Storage Project Hazard Mitigation Analysis [Draft]. ESRG: Energy Safety Response Group.

Bruckner, M.Z, Ion Chromatography, Microbial Life Educational Resources, Science Education Resource Center at Carleton College, October 17, 2006, retrieved from https://serc.carleton.edu/microbelife/research_methods/biogeochemical/ic.html

Chen, J., Gao, F., Li, X., Yang, K., Wang, S., & Yang, R. (2017). The study of the toxicity of the gas released on lithium ion battery during combustion. *Proceedings of the 2017 2nd International Conference on Automation, Mechanical and Electrical Engineering (AMEE 2017)*.

Cheng, M. (2017). Atmospheric chemistry of hydrogen fluoride. *Journal of Atmospheric Chemistry*, 75, 1-16.

Committee on Acute Exposure Guideline Levels. (2008). Chapter 9: Sulfur Dioxide, *Acute Exposure Guideline Levels for Selected Airborne Chemicals: Volume 6*. Committee on Toxicology, Board on Environmental Studies and Toxicology, National Research Council.

Committee on Acute Exposure Guideline Levels. (2009). Benzene (CAS Reg. No. 71-43-2): Interim Acute Exposure Guideline Levels (AEGLs). Committee on Toxicology, Board on Environmental Studies and Toxicology, National Research Council.

Committee on Acute Exposure Guideline Levels. (2010). Chapter 9: Sulfur Dioxide, *Acute Exposure Guideline Levels for Selected Airborne Chemicals: Volume 8*. Committee on Toxicology, Board on Environmental Studies and Toxicology, National Research Council.

Committee on Acute Exposure Guideline Levels. (2012). Chapter 4: Nitrogen Oxides, *Acute Exposure Guideline Levels for Selected Airborne Chemicals: Volume 11*. Committee on Toxicology, Board on Environmental Studies and Toxicology, National Research Council.

Committee on Acute Exposure Guideline Levels. (2014). Chapter 8: Hydrogen Bromide, *Acute Exposure Guideline Levels for Selected Airborne Chemicals: Volume 17*. Committee on Toxicology, Board on Environmental Studies and Toxicology, National Research Council.

Department of Energy (DOE) National Nuclear Security Administration (NNSA), Protective Action Criteria (PAC): Chemicals with AEGLs, ERPGs, & TEELs, retrieved 10/22/2024 from https://edms3.energy.gov/pac#/

Ditch, B., & Zeng, D. (2020). Fire hazard of lithium-ion battery energy storage systems: 1. module to rack-scale fire tests. *Fire Technology*.

Electric Power Research Institute (EPRI), August 2024. BESS Failure Incident Database, retrieved from https://storagewiki.epri.com/index.php/BESS_Failure_Incident_Database

Enphase, IQ Battery 5P Datasheet, September 9, 2024, retrieved from https://enphase.com/store/storage/gen3/iq-battery-5p

Enphase. (2023). UL 9540A report summary of IQ Battery 5: Model Number: IQBATTERY-5P-1P-NA, SKU: B05-T02-US00-1-3.

Environmental Protection Agency (EPA), Ecological Structure Activity Relationships (ECOSAR) Predictive Model, August 20, 2024, retrieved from https://www.epa.gov/tsca-screening-tools/ecological-structure-activity-relationships-ecosar-predictive-model

Essl, Golubkov, A.W., Gasser, E., Nachtnebel, M., Zankel, A., Ewert, E., & Fuch, A. (2020a). Comprehensive Hazard Analysis of Failing Automotive Lithium-Ion Batteries in Overtemperature Experiments. *Batteries*, 6, 30.

Essl, C., Golubkov, A.W., & Fuchs, A. (2020b). Comparing Different Thermal Runaway Triggers for Two Automotive Lithium-Ion Battery Cell Types. *Journal of The Electrochemical Society*, 167, 130542.

Environmental Safety and Health Group (ESHG), August 2020. Carbon Dioxide: Health Hazard Information Sheet. Food Safety and Inspection Service (FSIS), U.S. Department of Agriculture (USDA).

Fisher Engineering. (2022). Tesla Megapack 2: UL 9540A Fire Protection Engineering Analysis, UL 9549A Fire Test Analysis (MP2 FPE report 22035-02R).

Forestier, C., Lecocq, A., Zantman, A., Grugeon, S., Sannier, L., Marlair, G., & Laruelle, S. (2020). Study of the Role of LiNi1/3Mn1/3Co1/3O2/Graphite Li-Ion Pouch Cells Confinement, Electrolyte Composition and Separator Coating on Thermal Runaway and Off-Gas Toxicity. *Journal of The Electrochemical Society*, 167, 090513.

Fortress Power, eVault Max 18.5: Lithium Battery Storage, retrieved 3/20/2024 from https://www.fortresspower.com/wp-content/uploads/2022/05/eVault-MAX-18.5-technical-datasheet.pdf

Franqueville, J.I., Archibald, E.J., & Ezekoye. (2023). Data-driven modeling of downwind toxic gas dispersion in lithium-ion battery failures using computational fluid dynamics. *Journal of Loss Prevention in the Process Industries*, 86, 105201.

Galbraith, D., Gross, S.A., & Paustenbach, D. (2010). Benzene and human health: A historical review and appraisal of associations with various diseases. *Critical Reviews in Toxicology*, 40, 1-46.

Golubkov, A.W., Fuchs, D., Wagner, J., Wiltsche, H., Stangl, C., Fauler, G., Voitic, G., Thaler, A., & Hacker, V. (2014). Thermal-runaway experiments on consumer Li-ion batteries with metal-oxide and olivin-type cathodes. *RSC Advances*, 4, 3633.

Golubkov, A.W., Scheikl, S., Planteu, R., Voitic, G., Wiltsche, H., Stangl, C., Fauler, G., & Hacker, V. (2015). Thermal runaway of commercial 18650 Li-ion batteries with LFP and NCA cathodes – impact of state of charge and overcharge. *RSC Advances*, 5, 57171.

Grant, C., Hough, G., & Petrakis, N. (2023). Elkhorn Battery Energy Storage System Fire: Public Report of Technical Findings. Energy Safety Response Group (ESRG).

Hinshaw, J.V. (2005). The Flame Ionization Detector. *LCGC North America*, 23(12), 1262-1272.

Hill, D. (2020). McMicken Battery Energy Storage System Event Technical Analysis and Recommendations. Arizona Public Service.

Hines, J. & McGhee, R. "Tesla battery on fire at Bouldercombe energy storage site, Genex confirms." ABC Capricornia, September 27, 2023, retrieved from https://www.abc.net.au/news/2023-09-27/tesla-battery-fire-at-queensland-renewable-energy-project/102905302

Hodges, J.L. (2020). pyFDStools: A Python Package to Assist in Developing and Post-Processing Data Produced Through the Computational Fluid Dynamics Software Fire Dynamics Simulator, GitHub repository, https://github.com/johodges/pyfdstools.

Huang, P., Ping, P., Li, K., Chen, H., Wang, Q., Wen, J., & Sun, J. (2016). Experimental and modeling analysis of thermal runaway propagation over the large format energy storage battery module with Li4Ti5O12 anode. *Applied Energy*, 183, 659-673.

Huang, Z., Zhao, C., Huang, L., Peng, W., & Zhang, Z. (2020). Experimental study on thermal runaway and its propagation in the large format lithium ion battery module with two electrical connection modes. *Energy*, 205, 117906.

Huang, Z., Li, X., Wang, Q., Duan, Q., Li, Y., & Li, L. (2021). Experimental investigation on thermal runaway propagation of large format lithium ion battery modules with two cathodes. *International Journal of Heat and Mass Transfer*, 172, 121077.

Huertas, J.I., Martinez, D.S., & Prato, D.F. (2021). Numerical approximation to the effects of the atmospheric stability conditions on the dispersion of pollutants over flat areas. *Scientific Reports*, 11, 11566.

International Code Council (ICC). (2024). Section 1207 Electrical Energy Storage Systems (ESS), International Fire Code (IFC), 2024 ed.

Jha, R.K. (2022). Non-Dispersive Infrared Gas Sensing Technology: A Review. *IEEE Sensors Journal*, 22(1), 6-15.

Kawamura, K., Miyazawa, K., & Kent, L. (2021). The Past, Present and Future in Tube- and Paper-Based Colorimetric Gas Detectors. *AppliedChem*, 1(1), 14-40.

Kendall, R., Anderson, T., Baker, R., Bens, C., Carr, J., Chiodo, L. et al. (2001). "Ecotoxicity" in Klassen, C.D. (Ed.), *Casarett & Doull's Toxicology: The Basic Science of Poisons*, 1013-1045, New York, NY: McGraw-Hill.

Larsson, F., Andersson, P., Blomqvist, P., & Mellander, B.-E. (2016). Gas Emissions from Lithium-Ion Battery Cells Undergoing Abuse from External Fire.

Larsson, F., Andersson, P., Blomqvist, P., & Mellander, B.-E. (2017). Toxic fluoride gas emissions from lithium-ion battery fires. *Scientific Reports*, 7(1).

Lecocq, A., Eshetu, G.G., Grugeon, S., Martin, N., Laruelle, S., & Marlair, G. (2016). Scenario-based prediction of Li-ion batteries fire-induced toxicity. *Journal of Power Sources*, 316, 197-206.

Lee, C. P., & Stoliarov, D. S. I. (2018). Analysis and Qualification of Hazards Associated with Cascading Thermal Runway Propagation in Lithium Ion Battery Cell Arrays (thesis).

Lemieux, P.M., Lutes, C.C., & Santoianni, D.A. (2004). Emissions of organic air toxics from open burning: a comprehensive review. *Progress in Energy and Combustion Science*, 30(1), 1-32.

LibreTexts Chemistry. Gas Chromatography, LibreTexts, retrieved on 11/12/2024 from https://chem.libretexts.org/Bookshelves/Analytical_Chemistry/Supplemental_Modules_(Analytical_Chemistry)/Instrumentation_and_Analysis/Chromatography/Gas_Chromatography

Liu, P., Liu, C., Yang, K., Zhang, M., Gao, F., Mao, B., Li, H., Duan, Q., & Wang, Q. (2020). Thermal runaway and fire behaviors of lithium iron phosphate battery induced by over heating. *Journal of Energy Storage*, 31, 101714.

Liu, P., Li, Y., Mao, B., Chen, M., Huang, Z., & Wang, Q. (2021). Experimental study on thermal runaway and fire behaviors of large format lithium iron phosphate battery. *Applied Thermal Engineering*, 192, 116949.

Long, R.T., Blum, A.F., Bress, T.J., & Cotts, B.R.T. (2013). Best Practices for Emergency Response Incidents Involving Electric Vehicles Battery Hazards: A Report on Full Scale Testing Results (thesis). The Fire Protection Research Foundation.

Lopez, C.F., Jeevarajan, J.A., & Mukherjee, P.P. (2015). Experimental Analysis of Thermal Runaway and Propagation in Lithium-Ion Battery Modules. *Journal of The Electrochemical Society*, 162(9).

Mayanado, J.G., El Ouaragli, J., Flibbert, S., Kraft, S., Lebowitz, J., Hodges, J., & Conzen, J. (2024). Advancing Li-ion BESS Safety: Comprehensive Testing and Meta-Analysis for Optimized Hazard Mitigation. Jensen Hughes.

McGratten, K., McDermott, R., Vanella, M., Mueller, E., Hostikka, S., & Floyd, J. (2024a). NIST Special Publication 1018-2 - Fire Dynamics Simulator Technical Reference Guide Volume 2: Verification (Rev Ed.). National Institute of Standards and Technology.

McGratten, K., McDermott, R., Vanella, M., Mueller, E., Hostikka, S., & Floyd, J. (2024b). NIST Special Publication 1018-3 - Fire Dynamics Simulator Technical Reference Guide Volume 3: Validation (Rev Ed.). National Institute of Standards and Technology.

Meng, X., Yang, K., Zhang, M., Gao, F., Liu, Y., Duan, Q., & Wang, Q. (2020). Experimental study on combustion behavior and fire extinguishing of lithium iron phosphate battery. *Journal of Energy Storage*, 30, 101532.

Murray, C. "Terra-Gen to investigate cause of Valley Center California BESS fire with 'incident over'." Energy Storage News, September 19, 2023, retrieved from https://www.energy-storage.news/terra-gen-to-investigate-cause-of-valley-center-battery-storage-fire-with-incident-over/

National Institute for the Industrial Environment and Risks (INERIS). (2022) List of toxic substances (having a potential short, medium and long-term impact) likely to be emitted by a fire, Verneuil-en-Halatte: Ineris -203887 - v3.0.

National Fire Research Laboratory (NFRL) National Institute of Standards and Technology (NIST). (2020). Test_1, Room Flashover Experiments to Demonstrate Effectiveness of Barrier Fabrics, Fire Calorimetry Database (FCD).

National Fire Protection Association (NFPA). (2023). Chapter 9- Electrochemical Energy Storage Systems, NFPA 855: Standard for the Installation of Stationary Energy Storage Systems, 2023 ed.

National Institute of Standards and Technology (NIST), Cone Calorimeter, June 24, 2024, retrieved from https://www.nist.gov/laboratories/tools-instruments/cone-calorimeter

National Institute for Occupational Safety and Health (NIOSH). (2004). NIOSH respirator selection logic. Cincinnati, OH: U.S. Department of Health and Human Services, Centers for Disease Control and Prevention, National Institute for Occupational Safety and Health, DHHS (NIOSH) Publication No. 2005-100, retrieved from http://www.cdc.gov/niosh/docs/2005-100/pdfs/2005-100.pdf

National Institute for Occupational Safety and Health (NIOSH). (2017). Immediately Dangerous to Life or Health (IDLH) Value Profile: Nitrogen Dioxide. Centers for Disease Control and Prevention

National Institute for Occupational Safety and Health (NIOSH), February 2021, Immediately Dangerous To Life or Health (IDLH) Values - Table of IDLH Values. Centers for Disease Control and Prevention, retrieved from https://www.cdc.gov/niosh/idlh/intridl4.html

National Oceanic and Atmospheric Administration (NOAA) Office of Response and Restoration, Emergency Response Planning Guidelines (ERPGs), retrieved 10/22/2024 from https://response.restoration.noaa.gov/oil-and-chemical-spills/chemical-spills/resources/emergency-response-planning-guidelines-erpgs.html

National Oceanic and Atmospheric Administration (NOAA) Office of Response and Restoration, Temporary Emergency Exposure Guidelines (TEELs), retrieved 10/22/2024 from https://response.restoration.noaa.gov/oil-and-chemical-spills/chemical-spills/resources/temporary-emergency-exposure-limits-teels.html

National Oceanic and Atmospheric Administration (NOAA), Cameo Chemicals, retrieved 10/22/2024 from https://cameochemicals.noaa.gov/

Nedjalkov, A., Meyer, J., Köhring, M., Doering, A., Angelmahr, M., Dahle, S., Sander, A., Fischer, A., & Schade, W. (2016). Toxic gas emissions from damaged lithium ion batteries—analysis and Safety Enhancement Solution. *Batteries*, 2(1), 5.

Netzsch, Accelerating Rate Calorimetry: Advanced Solution for Chemical Process Safety, Energetic Material, and Battery Development, 2019, retrieved from https://paralab.pt/wp-content/uploads/2019/11/ARC_en_web.pdf

New York State, Inter-Agency Fire Safety Working Group. (2023). New York Inter-Agency Fire Safety Working Group Air, Soil, and Water Data Findings. New York State Energy Research and Development Authority (NYSERDA).

Nikolic, M.V., Milovanovic, V., Vasiljevic, Z.Z., & Stamenkovic, Z. (2020). Semiconductor Gas Sensors: Materials, Technology, Design, and Application. *Sensors*, 20(22), 6694.

Nugent, A. & DeCou, D. (2019). "Chapter 5- Atmospheric Stability" in Nugent, A., DeCou, D., Russell, S., & Karamperidou, C. (Ed.), *Atmospheric Processes and Phenomena*, University of Hawai'i at Manoa.

O'Connor, B. (2021). NFPA 855: Standard for Installation of Stationary Energy Storage Systems. National Fire Protection Association (NFPA).

Peacock, B. "Queensland Bouldercombe battery fire ignited on grid side, not within Megapack, analysis finds." PV Magazine, November 7, 2023, retrieved from https://www.pv-magazine-australia.com/2023/11/07/queensland-bouldercombe-battery-fire-ignited-on-grid-side-not-within-megapack-analysis-finds/

Peng, Y., Yang, L., Ju, X., Liao, B., Ye, K., Li, L., Cao, B., & Ni, Y. (2020). A comprehensive investigation on the thermal and toxic hazards of large format lithium-ion batteries with Lifepo4 Cathode. *Journal of Hazardous Materials*, 381, 120916.

Premnath, V., Wang, Y., Wright, N., Khalek, I., & Uribe, S. (2022). Detailed characterization of particle emissions from battery fires. *Aerosol Science and Technology*, 556(4), 337-354.

Quant, M., Willstrand, O., Mallin, T., & Hynynen, J. (2023). Ecotoxicity Evaluation of Fire-Extinguishing Water from Large-Scale Battery and Battery Electric Vehicle Fire Tests. *Environmental Science & Technology*, 57(12), 4821-4830.

Said, A.O. & Stoliarov, S.I. (2021) Analysis of effectiveness of suppression of lithium ion battery fires with a clean agent. *Fire Safety Journal*, 121.

Simpliphi Power, Phi 3.8TM Battery- REV202106281043, retrieved 3/21/2024 from https://simpliphipower.com/wp-content/uploads/documentation/phi-3-8/simpliphi-power-phi-3-8-kwh-60-amp-specification-sheet.pdf

Simpliphi Power, The Boss .6 and .12: Battery Only Storage Systems- REV202102081346, retrieved 3/21/2024 from https://simpliphipower.com/wp-content/uploads/documentation/boss-12/simpliphi-power-boss-6-12-specification-sheet.pdf

Sturk, D., Hoffman, L., & Ahlberg-Tidblad, A. (2015). Fire Tests on E-vehicle Battery Cells and Packs. *Traffic Injury Prevention*, 16, S159-S164.

Sturk, D., Rosell, L., Blomqvist, P., & Ahlberg-Tidblad, A. (2019). Analysis of li-ion battery gases vented in an inert atmosphere thermal test chamber. *Batteries*, 5(3), 61.

Subcommittee on Acute Exposure Guideline Levels. (2002). Chapter 5: Hydrogen Cyanide. *Acute Exposure Guideline Levels for Selected Airborne Chemicals: Volume 4*. Committee on Toxicology, Board on Environmental Studies and Toxicology, National Research Council.

Subcommittee on Acute Exposure Guideline Levels. (2004). *Acute Exposure Guideline Levels for Selected Airborne Chemicals: Volume 4*. Committee on Toxicology, Board on Environmental Studies and Toxicology, National Research Council.

Swenson, D, Updated FDS Combustion and Fuel Composition Calculators, Thunderhead Engineering, retrieved on 11/06/2024 from https://www.thunderheadeng.com/news/updated-fds-combustion-and-fuel-composition-calculators/

ThermoFisher Scientific, Inductively Coupled Plasma Optical Emission Spectroscopy (ICP-OES) Information, retrieved on 11/12/2024 from https://www.thermofisher.com/us/en/home/industrial/spectroscopy-elemental-isotope-analysis/spectroscopy-elemental-isotope-analysis-learning-center/trace-elemental-analysis-tea-information/icp-oes-information.html

Trouvé, A. (2023). *CFD Approaches*. PowerPoint Slides for ENFP626, University of Maryland, College Park.

TÜV Rheinland of North America, Inc. (2022). TEST REPORT ANSI/CAN/UL 9540A:2019 Test Method for Evaluating Thermal Runaway Fire Propagation in Battery Energy Storage Systems (Report No. NN22GLCI.003).

Underwriter's Laboratory (UL). (2019). ANSI/CAN/UL 9540A:2019: Standard For Safety: Test Method for Evaluating Thermal Runaway Fire Propagation in Battery Energy Storage Systems. Standards Council of Canada (SCC). American National Standards Institute (ANSI).

Underwriter's Laboratory (UL). (2020). UL 9540A Test Method for Evaluating Thermal Runaway Fire Propagation in Battery Energy Storage Systems: Unit Level Test Report, Model PHR0000-004AE3D- Project Number 4789231760.

Underwriter's Laboratory (UL). (2021). AACD.E527394B: UL 9540A Module Level Test Details – Summary.

Underwriter's Laboratory (UL). (2021). CELL TEST REPORT UL 9540A Test Method for Evaluating Thermal Runaway Fire Propagation in Battery Energy Storage Systems (AACD) (Project Number 4789956341).

Underwriter's Laboratory (UL). (2021). AACD.E527394C: UL 9540A Unit Level Test Details – Summary.

U.S. Environmental Protection Agency (EPA), About Acute Exposure Guideline Levels (AEGLs), retrieved 05/30/2024 from https://www.epa.gov/aegl/about-acute-exposure-guideline-levels-aegls

U.S. Environmental Protection Agency (EPA), Access Acute Exposure Guideline Levels (AEGLs) Values, retrieved 10/22/2024 from https://www.epa.gov/aegl/access-acute-exposure-guideline-levels-aegls-values

van Mierlo, R. (2005). The Single Burning Item (SBI) test method – a decade of development and plans for the near future. *HERON*, 50(4).

Von Burg, C. & Cross, S. (2022). NFPA- 9540A Test Method Analysis: REV202010051018. Simpliphi Power.

Wang, N., Chen, A., & Zhou, J. (2022). Project 80128223: Laboratory Test Data – UL 9540A Checklist and Test Result. CCIC-CSA International Certification Co., Canadian Standards Association (CSA) Group. Shanghai Huahui Testing Co.

Weather Spark, Climate and Average Weather Year Round in California, retrieved 03/01/2024 from https://weatherspark.com/countries/US/CA#google_vignette

Willstrand, O., Bisschop, R., Blomqvist, P., Temple, A., & Anderson, J. (2020). (rep.). Toxic Gases from Fire in Electric Vehicles (RISE Report 2020:90). RISE Research Institutes of Sweden AB.

Willstrand, O., Pushp, M., Andersson, P., & Brandell, D. (2023). Impact of different Li-ion cell test conditions on thermal runaway characteristics and gas release measurements. *Journal of Energy Storage*, 68, 107785.

Wilschefski, S.C. & Baxter, M.R. (2019). Inductively Coupled Plasma Mass Spectrometry: Introduction to Analytical Aspects. *The Clinical Biochemist Reviews*, 40(3), 115-133.

Yang, X., Wang, H., Li, M., Li, Y., Li, C., Zhang, Y., Chen, S., Shen, H., Qian, F., Feng, X., & Ouyang, M. (2022). Experimental Study on Thermal Runaway Behavior of Lithium-Ion Battery and Analysis of Combustible Limit of Gas Production. *Batteries*, 8, 250.

Yuan, L., Dubaniewicz, T., Zlochower, I., Thomas, R., & Rayyan, N. (2020). Experimental study on thermal runaway and vented gases of lithium-ion cells. *Process Safety and Environmental Protection*, 144, 186-192.

Zhang, Y., Wang, H., Li, W., & Li, C. (2019). Quantitative identification of emissions from abused prismatic Ni-rich lithium-ion batteries. eTransportation, 2, 100031.

Zhang, L., Duan, Q., Meng, X., Jin, K., Xu, J., Sun, J., & Wang, Q. (2022). Experimental investigation on intermittent spray cooling and toxic hazards of lithium-ion battery thermal runaway. *Energy Conversion and Management*, 252, 115091.